DEVELOPMENT OF DYNAMIC PHOSPHORUS-31 AND OXYGEN-17 MAGNETIC RESONANCE SPECTROSCOPY AND IMAGING TECNIQUES FOR PRECLINICAL ASSESSMENT OF ENERGY METABOLISM IN VIVO

by

YUCHI LIU

Submitted in partial fulfillment of the requirements for the degree of

Doctor of Philosophy

Department of Biomedical Engineering

CASE WESTERN RESERVE UNIVERSITY

January, 2018

CASE WESTERN RESERVE UNIVERSITY

SCHOOL OF GRADUATE STUDIES

We hereby approve the dissertation of

Yuchi Liu

candidate for the degree of Doctor of Philosophy*.

Committee Chair

Dr. Nicole Seiberlich

Committee Member

Dr. Xin Yu

Committee Member

Dr. Mark Griswold

Committee Member

Dr. Nicola Lai

Committee Member

Dr. John Kirwan

Date of Defense

July 19th, 2017

*We also certify that written approval has been
obtained for any proprietary material contained therein.

Table of Contents

List of Tables

List of Figures

Acknowledgements

I would like to thank my family, friends, teachers, and all the other people without whom I would not be where I am today. They are like the gradients and RF pulses that help the magnetization of me to form echoes after five years' dephasing and refocusing.

First of all, I would like to thank my mentor, Dr. Xin Yu for her excellent guidance and support during the last five years. I feel so fortunate to have such a meticulous and responsible advisor to guide me through the most important years in my career. I would also like to thank my wonderful committee, Dr. Mark Griswold, Dr. Nicole Seiberlich, Dr. John Kirwan, and Dr. Nicola Lai, for their direct and indirect help on all the projects from the perspective of both technology and physiology.

I also want to thank my lab mates, Charlie Wang, Yifan Zhang, Xunbai Mei, Yuning Gu, Kai Jiang, Didi Goodnough, and Ya Chen for their support and inspirational discussions on the projects. I would like to thank Dr. Yanming Wang's group, Dr. Robert Salomon's group, and Dr. Yu Luo's group at CASE for providing animal models for my experiments. I am grateful to Dr. Zhi-Pei Liang's group at UIUC for their help with the development of ^{31}P SPICE. The enthusiasm and motivation towards science of Dr. Liang's group deeply impressed me.

Finally, I want to thank my parents for their love, support, and understanding. I specifically want to thank my husband Yun for being a good friend and a good teacher to me. He is my shimming coils. I am grateful to have him in my life sharing the sunny and rainy days of PhD with each other. I would also like to dedicate this thesis to my dearest grandmother in Heaven, who has always been supporting me and encouraging me to explore the world. I hope she is happy with what I have achieved today.

List of Abbreviations

Abbreviation	Definition
^{1}H	Proton
^{13}C	Carbon-13
^{15}O	Oxygen-15
^{17}O	Oxygen-17
^{23}Na	Sodium-23
^{31}P	Phosphorus-31
1D	One Dimensional
2D	Two Dimensional
3D	Three Dimensional
ADP	Adenosine Diphosphate
ASL	Arterial Spin Labeling
ATP	Adenosine Triphosphate
BBB	Blood-Brain Barrier
BOLD	Blood Oxygen Level Dependent
bSSFP	balanced Steady-State Free Precession
CBF	Cerebral Blood Flow
CK	Creatine Kinase
cm	centimeters
$CMRO_2$	Cerebral Metabolic Rate of Oxygen
CSI	Chemical Shift Imaging
EPSI	Echo Planar Spectroscopic Imaging
FID	Free Induction Decay
FLASH	Fast Low Angle Shot
flexTPI	flexible Twisted Projection Imaging
FOV	Field of View
FWHM	Full Width of Half Maximum
G	Gastrocnemius
GBM	Glioblastoma
GK	Goto-Kakizaki

ISIS	Image-Selected In vivo Spectroscopy
KWIC	k-space Weighted Image Contrast
MCAO	Middle Cerebral Artery Occlusion
min	minutes
MRI	Magnetic Resonance Imaging
MRS	Magnetic Resonance Spectroscopy
MRSI	Magnetic Resonance Spectroscopic Imaging
ms	milliseconds
MT	Magnetization Transfer
NMR	Nuclear Magnetic Resonance
NRMSE	Normalized Root Mean Square Error
NUFFT	Non-Uniform Fast Fourier Transform
OEF	Oxygen Extraction Fraction
PCr	Phosphocreatine
PDE	Phosphodiesters
PET	Positron Emission Tomography
P_i	Inorganic Phosphate
PME	Phosphomonoesters
PRESS	Point RESolved Spectroscopy
PS	Partial Separable
PSF	Point Spread Function
RARE	Rapid Acquisition with Relaxation Enhancement
RF	Radiofrequency
ROI	Region of Interest
s	seconds
SAR	Specific Absorption Rate
SNR	Signal-to-Noise Ratio
SPICE	SPectroscopic Imaging by exploiting spatiospectral CorrElation
STEAM	STimulated Echo Acquisition Mode
SVD	Singular Value Decomposition
SVS	Single Voxel Spectroscopy
T	Tesla

T2D	Type 2 Diabetes
TA	Tibialis Anterior
TE	Echo Time
TM	Mixing Time
TR	Repetition Time
TSE	Turbo Spin-Echo

Development of Dynamic Phosphorus-31 and Oxygen-17 Magnetic Resonance Spectroscopy and Imaging Techniques for Preclinical Assessment of Energy Metabolism in vivo

Abstract

by

YUCHI LIU

Adenosine triphosphate (ATP) is the energy currency that maintains physiological activities of the cell. The major source of ATP in aerobic organisms is oxidative phosphorylation occurred in mitochondria. Disruptions of oxidative phosphorylation are associated with various metabolic diseases. Hetero-nuclei MRI plays an important role in assessing functional cell processes such as oxidative metabolism. Specifically, phosphorous-31 (^{31}P) and oxygen-17 (^{17}O) MRS/MRI provide a non-invasive tool to probe mitochondrial oxidative capacity and oxygen consumption, respectively. However, hetero-nuclei MRI in general is challenging due to the low in vivo concentrations and low MR sensitivity. Long acquisition time is usually required even with low spatial resolution. In this thesis, novel approaches for imaging ^{31}P and ^{17}O with high spatial resolution and temporal resolution were developed and demonstrated in small animals at high fields. In particular, this thesis focused on fast ^{31}P MR Spectroscopic Imaging (MRSI) and ^{17}O MRI approaches with non-Cartesian encoding schemes that assess mitochondrial function in skeletal muscle and cerebral oxygen metabolism/water movement across the blood-brain barrier (BBB), respectively.

Four projects are described in this thesis. First, an ischemia-reperfusion protocol was established to evaluate mitochondrial oxidative capacity in type 2 diabetic rats using ^{31}P MRS. Second, a fast dynamic ^{31}P MRSI method using a low-rank model was developed and demonstrated in rat skeletal muscle during ischemia-reperfusion. Third, a dynamic ^{17}O MRI method using golden-angle radial acquisition combined with k-space weighted image contrast (KWIC) reconstruction was developed and validated in simulation studies and phantom experiments. Finally, the ^{17}O MRI method was demonstrated in a mouse model with glioblastoma (GBM) to assess the water movement across BBB after a bolus in injection of ^{17}O-labeled water. The ^{17}O MRI approach was also applied to a mouse model of middle cerebral artery occlusion (MCAO) in ^{17}O-labeled gas inhalation experiments to assess cerebral oxygen metabolism in vivo. The success of these studies will pave the way for fast metabolic imaging using ^{31}P and ^{17}O MRI techniques and allow for the assessment of metabolic alterations in various disease models, such as diabetes, ischemic stroke, etc.

Chapter 1. Introduction

1.1. Metabolism and Oxidative Phosphorylation

Metabolism is a set of chemical transformations in the cell to maintain normal functions in all levels of biological systems and thereby to sustain life. The purposes of metabolism include converting food to energy and to building blocks for proteins, lipids, etc. Specifically, the process of converting food/fuel to energy is referred to as energy metabolism. While the energy currency, adenosine triphosphate (ATP), can be produced in both aerobic metabolism and anaerobic metabolism in the presence or absence of oxygen, the major source of ATP is oxidative phosphorylation occurred in mitochondria in the cell.

Figure 1.1 illustrates the process of ATP production via oxidative phosphorylation in mitochondria. Three major processes are shown, including oxidation of the acetyl groups through citric acid cycle (also known as tricarboxylic acid cycle or Krebs cycle), proton gradient across the inner membrane of mitochondria generated by electron transport chain, and generation of ATP from adenosine diphosphate (ADP) via the ATP synthase driven by the proton gradient. The fuel molecules, such as pyruvate and fatty acids derived from sugars and fats, are transported across the membranes of mitochondria and converted to the crucial metabolic intermediate acetyl-CoA. The acetyl groups in acetyl-CoA are then oxidized through the citric acid cycle. During this oxidation process, the carbon atoms carried by acetyl-CoA are converted to CO_2 that is released as a waste product by the cell. On the other hand, this oxidation process also produces high-

energy electrons that are carried by NADH and $FADH_2$. Then these high-energy electrons enter electron transport chain at the inner membrane of mitochondria. Meanwhile NADH and $FADH_2$ are restored to NAD^+ and FAD due to the loss of electrons. The electrons are then transferred through three large respiratory enzyme complexes sequentially and finally reach oxygen, resulting in water converted from oxygen. As electrons pass along the electron transport chain, energy is stored as an electrochemical proton gradient across the inner mitochondrial membrane. This proton gradient drives proton back to the matrix of mitochondria through the ATP synthase, which is a membrane-bound enzyme. The ATP synthase creates a pathway across the inner membrane of mitochondria to allow protons to flow down

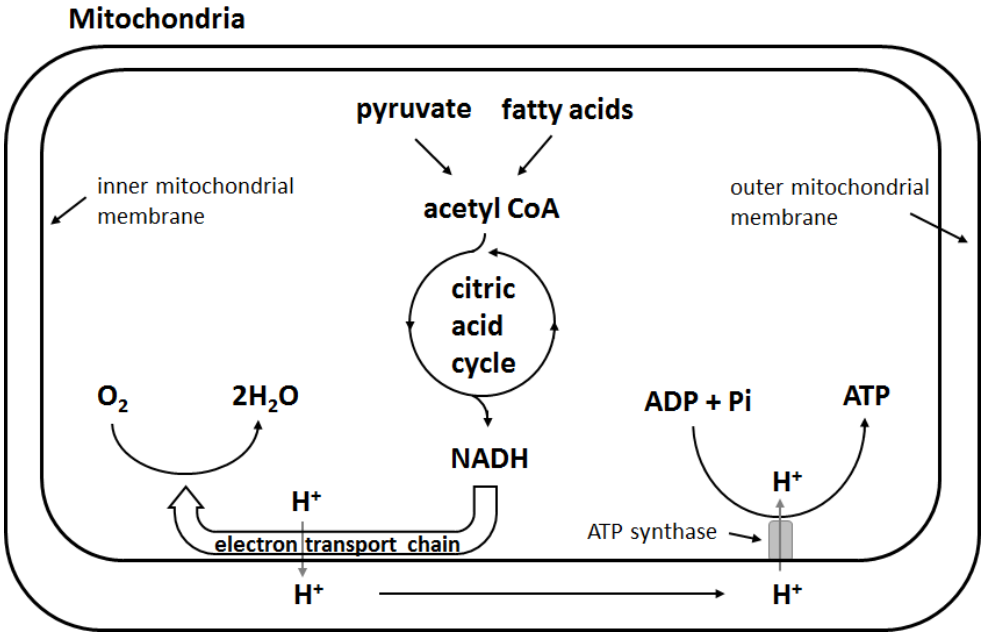

Figure 1.1. Illustration of oxidative phosphorylation in mitochondria. The acetyl groups in acetyl-CoA are oxidized through citric acid cycle, generating high-energy electrons carried by NADH and $FADH_2$. Electrons pass along electron transport chain and are transferred to oxygen, resulting in proton gradient across the inner membrane of mitochondria that drives the generation of ATP from ADP by the ATP synthase.

the electrochemical gradient, and uses the energy of the proton flow to synthesize ATP from ADP and inorganic phosphate (Pi) in the matrix of mitochondria.

Although the citric acid cycle is part of aerobic metabolism, oxygen is not directly consumed until it is combined with electrons on the inner mitochondrial membrane. For this reason, the series of reactions regarding electron transport at the inner membrane of mitochondria and following ATP synthesis via the ATP synthase are described by the term oxidative phosphorylation.

On the one hand, oxidative phosphorylation in mitochondria yields the majority of ATP to meet the energy demands; on the other hand, there exists a mechanism to buffer ATP concentrations in the cell via the creatine kinase (CK) reaction. CK is an enzyme that catalyzes the conversion of creatine and consumes ATP to generate phosphocreatine (PCr) and ADP. As shown in Eq. [1.1], this conversion is reversible, thereby ATP can also be created from PCr and ADP.

$$\mathrm{ATP} + \mathrm{Cr} \rightleftharpoons \mathrm{ADP} + \mathrm{PCr} + \mathrm{H}^{+} \qquad [1.1]$$

Therefore, CK is a key enzyme for maintaining the steady-state ATP concentrations in the cell, and PCr serves as an energy reservoir for rapid buffering of ATP. CK is expressed in various tissues and cell types. Cells with high energy demand (e.g., skeletal muscle cells) usually exhibit high CK concentrations. More importantly, CK exists in various isoforms. For example, mitochondrial CK presents in the intermembrane space of mitochondria, while cytosolic CK isoforms exist in the cytosol. As energy production and consumption take place at different locations in the cell with different CK isoforms, CK enzymes and PCr also function as a “shuttle”

to facilitate the transport of high-energy phosphates between different compartments of the cell (1).

As described above, under normal conditions, the majority of ATP is supplied by oxidative phosphorylation catalyzed by the ATP synthase enzyme, and ATP is rapidly cycled in the body to meet energy demands. These processes are accompanied by the important CK reaction, which facilitates to maintain a stable cellular ATP level and transport of high-energy phosphates between the mitochondria and cytosol.

However, ATP energy pathways could be disrupted under pathological conditions. Disruptions of oxidative phosphorylation and the CK reaction are associated with various metabolic diseases (2–7). For example, when cells are derived of oxygen during ischemic stroke in the brain, ATP generation through the ATP synthase cannot be completed during oxidative phosphorylation. As a result of diminished energy supply, brain function in the affected area is temporarily and even permanently damaged. On the other hand, intentional control of the oxygen demand or supply also provides a tool to investigate the oxidative capacity of mitochondria. For example, hypoxia during ischemia and high demand of energy during exercise in skeletal muscle leads to perturbations to steady-state ATP levels. Under these circumstances, ATP generation through oxidative phosphorylation is not sufficient to maintain stable ATP levels in the cell, hence PCr acts as an energy reservoir to fill the ATP pool and this reaction is catalyzed by the CK enzyme. Upon the end of the perturbation (i.e., exercise or ischemia), the PCr pool is replenished by ATP in return because ATP generation through oxidative

phosphorylation is restored in mitochondria. Therefore, the kinetics of PCr changes during and after exercise/ischemia acts as an index of the oxidative capacity of mitochondria, and provides a potential way to evaluate mitochondrial function in vivo (8–12).

1.2. Assessing Mitochondrial Function Using ^{31}P MRS/MRI

Since the early development of magnetic resonance imaging (MRI) as an imaging modality in the 1970s (13), the technique has branched into various fields with the primary focus on imaging protons (^{1}H). Meanwhile, hetero-nuclei are of great value in probing unique aspects of metabolism in both preclinical and clinical research. MR spectroscopy (MRS), also referred to as nuclear magnetic resonance (NMR), provides a non-invasive approach to investigate metabolism in vivo. Particularly, phosphorous-31 (^{31}P) plays an important role in energy metabolism and ^{31}P MRS provides a unique tool to probe bioenergetics in vivo by measuring energy metabolites such as PCr, ATP, and Pi. Since the 1970s, ^{31}P MRS has been used extensively to study metabolism in heart (14–16), muscle (17), kidney (18), and brain (19,20). Albeit proton MRS became more prevalent in the 1990s due to its higher MR sensitivity and the development of water suppression techniques, hetero-nuclei such as ^{31}P remain of interest, particularly at high magnetic fields.

Compared to imaging protons in water, ^{31}P MRS/I is challenging because of the low MR sensitivity and low concentrations of phosphate metabolites. The concentrations of PCr, ATP, and P_i in human skeletal muscle are approximately 30, 10, and 5 mM (21), which are four orders of magnitude lower than water protons in tissue. However, ^{31}P MRS/I has some advantages comparing to proton and other

hetero-nuclei MRS. First, ^{31}P has a natural abundance of 100%, hence, it is relatively easy to acquire ^{31}P spectra with good quality even at low field strength. Second, there are only a few resonance peaks (five major peaks) dispersed in a relatively wide range of about 30 ppm in a ^{31}P spectrum, resulting in more straightforward peak quantification. Third, no suppression techniques are needed in ^{31}P MRS/I due to the absence of dominant water or fat signal. Finally, the SNR gain provided by high magnetic fields is not compromised by longer longitudinal relaxation time (T_1) as in ^{1}H imaging. On the contrary, T_1 of ^{31}P nuclei is reduced at high fields, making fast acquisition with a relatively short repetition time (TR) possible (22–25). A significant decrease in T_1 of PCr has been reported with an increase in field strength in the resting human calf muscle (6.7 s ± 0.4 s at 3T versus 4 s ± 0.2 s at 7T) (25) and in human brain (4.27 s ± 0.27 s at 4T versus 3.37 s ± 0.29 s at 7T) (24).

1.2.1. Steady-state ^{31}P MRS

^{31}P MRS is a powerful tool to quantify PCr, ATP, and Pi, the three major phosphate metabolites involved in high-energy metabolism. PCr is usually assigned a chemical shift of 0 ppm due to its relative stability and prominence in most organs. P_i and the phospholipids, including phosphomonoesters (PME) and phosphodiesters (PDE), are located to the left of PCr. Resonant peaks from the three phosphate groups of ATP (γ-, α-, and β-ATP from left to right) are located to the right of PCr. Nicotinamide adenine dinucleotide (NAD) in its oxidized and reduced form, i.e., NAD^+ and NADH, can also be detected in ^{31}P spectra. The concentration of ADP under physiological conditions is too low to be detectable by

in vivo ^{31}P MRS. However, as will be shown later, ADP can be calculated indirectly from the concentrations of PCr, ATP, and Cr.

To quantify the ^{31}P metabolites from a steady-state ^{31}P spectrum, acquisition parameters need to be carefully chosen to achieve best SNR efficiency. A fully relaxed spectrum with complete T_1 recovery after each signal acquisition is frequently used for accurate quantification of all peaks. In this case, TR is usually chosen as ~15 s with 90° flip angle, and minimum acquisition delay is preferable to avoid signal loss due to transverse magnetization decay. For accurate quantification, some post-processing strategies are also necessary to remove distortions and to improve spectral quality, including phase correction (26–28), line broadening (29), and baseline correction (30–33).

Direct quantification of the metabolite concentrations from measured signal intensity is complicated by many factors such as coil sensitivity, field inhomogeneity, and relaxation time. In order to convert relative signal intensity into absolute concentrations in mM, either an internal or an external concentration reference can be used. For the internal reference approach, ATP is typically usually used as an internal reference because the concentration of ATP is relatively stable stable (~8.2 mM cell water) (21). For the external reference approach, a phantom with known concentration of P_i solution is often placed beside the image object and within the coil sensitivity range (34). The concentrations of the metabolites are then derived based on the following equation:

$$C = C_{ref} \times \frac{SI}{SI_{ref}} \times f \qquad [1.2]$$

where C and SI are concentration and signal intensity of the metabolite of interest, C_{ref} and SI_{ref} are the concentration and signal intensity of the reference, and f is a correction factor that takes into account the differences in coil sensitivity and T_1 saturation between the external reference and in vivo metabolites. Accurate estimation of the correction factor f requires measurements of B_1 field map of the ^{31}P transceiver coil and relaxation times of both the external reference and the metabolites. However, these measurements in ^{31}P are much more challenging and time consuming than those in proton due to low sensitivity and low in vivo concentrations. B_1 field mapping for a ^{31}P volume coil has been reported to take over one hour in human calf muscle (35). Therefore, accurate calculation of the metabolite concentrations using this approach is not always practical especially in small animals limited by SNR. Alternatively, the metabolite ratio that can be directly obtained from the acquired spectra, such as PCr-to-Pi and PCr-to-ATP ratio, is considered an indicator of metabolic changes and is frequently used in a variety of pathology studies (36–44).

ADP concentration can be calculated from the concentrations of PCr, ATP, and Cr due to the chemical equilibrium of the CK reaction (45,46),

$$C_{ADP} = \frac{C_{Cr} \times C_{ATP}}{C_{PCr} \times C_{H^+} \times K_{CK}} \quad [1.3]$$

The equilibrium constant of CK (K_{CK}) is approximately 1.66×10^9 M^{-1} (47). The concentration of Cr can be calculated based on the assumption that PCr represents ~85% of total creatine (i.e. the sum of PCr and free Cr) at rest (48), or the assumption based on muscle biopsies that the concentration of total creatine is 42 mM in muscles (21).

Besides the quantification of metabolite concentrations, ^{31}P MRS also provides a non-invasive tool to measure tissue pH in vivo. The chemical shifts of many phosphorus compounds are pH dependent, because protonation of a compound changes the electron distribution surrounding the nuclei and thus changes their resonance frequencies. In a ^{31}P spectrum, the chemical shift of P_i is most sensitive to changes in pH near neutrality because the dissociation constant of P_i, i.e., the pK of $H_2PO_4^- \rightleftharpoons H^+ + HPO_4^{-2}$, is approximately 7. Hence, from the observed chemical shift of P_i (δ), which is a concentration-weighted sum of the chemical shifts of $H_2PO_4^-$ ($\delta_{H_2PO_4^-}$) and HPO_4^{-2} ($\delta_{HPO_4^{-2}}$), tissue pH can be calculated as

$$pH = pK + \log\left(\frac{\delta - \delta_{H_2PO_4^-}}{\delta_{HPO_4^{-2}} - \delta}\right) \quad [1.4]$$

For cardiac and skeletal muscle, pK, $\delta_{H_2PO_4^-}$, and $\delta_{HPO_4^{-2}}$ are 6.75, 3.27, and 5.69, respectively (49). In the brain, these values differ slightly at 6.77, 3.29, and 5.68, respectively (50,51). The accuracy of pH quantification using P_i-PCr system may be affected by low Pi concentration at normal physiology conditions, or depleted PCr under hypoxia and in tumors. Alternative approaches such as the P_i-αATP method can be used for the spectra without well-defined PCr, such as in the liver (52).

1.2.2. Dynamic ^{31}P MRS

As described in Chapter 1.1, PCr recovery rate upon the end of a metabolic perturbation can be used as an index of mitochondrial oxidative capacity (53). In skeletal muscle, the perturbation is usually induced by muscle exercise/stimulation

or ischemia. Continuous acquisition of ^{31}P spectra during exercise-recovery or ischemia-reperfusion provides the potential to assess mitochondrial oxidative capacity by quantifying the kinetics of PCr depletion and replenishment. Indeed, dynamic ^{31}P MRS has been applied to assess skeletal muscle bioenergetics under physiological conditions (44,49,54–58), as well as to evaluate mitochondrial function in skeletal muscle in both diabetic patients and animal models of type 2 diabetes (7,59–61).

During muscle contraction or ischemia, PCr is depleted by the CK reaction to maintain a constant ATP level and P_i is accumulated. Intracellular pH increases initially due to PCr hydrolysis and decreases during longer contraction protocols due to accumulation of lactate resulting from glycolysis under anaerobic conditions (53). PCr, P_i, and pH recover to baseline level upon cessation of the contraction or ischemia, and PCr recovery rate derived from the dynamic spectra reflects mitochondrial oxidative capacity.

PCr recovery time constant in calf muscle is typically on the order of 25 ~ 35 s in humans (58,62) and 50 ~ 90 s in small animals (55,58,61,63). Prolonged PCr recovery is usually accompanied by deficits in mitochondrial function (64,65). Hence, a temporal resolution of <10 s in humans and <20 s in small animals is desired to capture the kinetics of ^{31}P metabolites changes. In dynamic studies, a short TR of typical 1~2 s is commonly used with Ernst angle for SNR benefit (66). However, absolute quantification of the metabolites is impossible using this approach due to T_1 saturation effects caused by short TR. To achieve accurate quantification while maintain high temporal resolution, a fully relaxed spectrum

using long TR is usually acquired at steady-state to correct for T_1 saturation effects, while dynamic spectra are acquired using short TR during the dynamic process.

1.2.3. Single Voxel Spectroscopy (SVS)

SVS techniques were developed in the 1980s to acquire spectra from a 3D cuboid volume. The selection of the 3D cuboid voxel can be achieved using either single- or multi-acquisition approaches. The single-acquisition techniques include the Point RESolved Spectroscopy (PRESS) and the STimulated Echo Acquisition Mode (STEAM) approaches (67–69). In PRESS, sequential 90°-180°-180° RF pulses with three slice selective gradients in orthogonal planes are used to achieve 3D volume selection, resulting in spin echo and thereby relatively preferable SNR. However, the long TE resulting from multiple sequential RF pulses is not suitable for imaging short T_2 species, such as ^{31}P metabolites. Therefore, PRESS is a popular SVS method and commonly used in ^{1}H MRS (70–73) but not widely applied in ^{31}P MRS. In contrast, STEAM employs 90°-90°-90° RF pulses for 3D localization, resulting in a shorter TE and lower RF power deposition compared to PRESS. Furthermore, the second 90° pulse stores magnetization in z-direction and thus avoid signal loss due to T_2 decay. However, the stimulated echo formed by STEAM sequence has only about half of the SNR compared to the spin echo in PRESS at the same TE and TR (74).

The Image-Selected In vivo Spectroscopy (ISIS) technique is a multi-acquisition approach. Compared to PRESS and STEAM, ISIS requires multiple acquisitions and depends on post-acquisition signal combination to derive the spectrum from a localized voxel (75). In brief, 3D localization is achieved by

addition and subtraction of eight acquisitions with slice selective gradient and the concurrent 180° inversion pulse on or off prior to the nonselective excitation pulse. ISIS is a preferred method for short T_2 metabolites since FID is acquired with minimum acquisition delay. Therefore, this approach is a primary method for ^{31}P MRS (76–81). However, the multiple acquisitions with following additions and subtractions make ISIS sensitive to motion artifacts. More detailed comparison of the three SVS methods can be found in the review by Keevil (82).

1.2.4. Chemical Selective Imaging Methods

SVS techniques successfully provide a reasonable selectivity of the volume of interest. However, the limited spatial information acquired by SVS cannot meet the demand of capturing heterogeneous alterations in tissue metabolism when high spatial resolution is desired. Direct imaging of a single ^{31}P metabolite provides spatial mapping of the metabolic state or alterations in vivo with relatively high spatial resolution, and avoids extremely long acquisition time as in MR spectroscopic imaging (MRSI) by reducing the chemical shift dimension. Since PCr and Pi are of the most interest in assessing mitochondrial function and intracellular pH, they are the focus of most ^{31}P imaging studies.

There are mainly two approaches to achieve chemical selection of a single ^{31}P metabolite. Greenman and colleagues achieved chemical selection of PCr by careful design of the time delay between the RF pulses in a Rapid Acquisition with Relaxation Enhancement (RARE) sequence, allowing for other resonances but PCr signals substantially suppressed (83). This approach was applied in both 2D and 3D PCr imaging studies in human forearm (83), normal human myocardium (84),

and human calf muscle (85–87). However, the implementation of this approach is limited in spin-echo sequences because suppression of ATP and Pi peaks rely on the spacing between the excitation and refocusing RF pulses. In addition, the timing of RF pulses must be carefully designed and evaluated at different field strengths due to the field-dependent chemical shift between ^{31}P metabolites. The other approach developed by Parasoglou et al employed a spectral selective RF pulse without the use of a slice selective gradient to achieve 3D PCr imaging in human skeletal muscle (35,62,88–90). Spatial encoding within the coil sensitive volume is performed by phase encoding gradients. The absence of the slice selective gradient avoids the complications of spectral-spatial selective RF pulses, but renders this approach not applicable to 2D imaging sequences.

The signal readout approaches for ^{31}P MRI fall into two categories: turbo spin-echo (TSE) methods, and gradient-echo methods. The two groups mentioned above (Greenman et al and Parasoglou et al) both use TSE (also known as RARE) sequences to acquire PCr signals. On the other hand, gradient-echo approaches have also been used to image PCr of human myocardium tissue and skeletal muscle (91), as well as PCr/ATP ratio of human head (92). TSE sequences are preferable for PCr imaging due to the relatively long T_2 of PCr in vivo compared with other ^{31}P metabolites (22,25). However, TSE methods have a demand on high RF amplitude and B_1 homogeneity to achieve satisfactory refocusing. In contrast, gradient-echo methods are preferable to ATP imaging than TSE methods due to the relatively short T_2 values of ATP (22,25). Moreover, low RF power is needed in gradient-

echo methods without the use of refocusing pulses, resulting in low specific absorption rate (SAR).

Table 1.1. A summary of typical static and dynamic PCr imaging studies in humans.

Reference	Study	Field Strength	Organ	Voxel Size (mm^3)	Experiment Time
Greenman et al (84)	3D PCr imaging	4T	heart	12.5×12.5×25	9 min 40 s
Greenman et al (85)	2D PCr imaging	3T	skeletal muscle	4.68×4.68×25	4 min
Greenman et al (86)	2D dynamic PCr imaging	3T	skeletal muscle	15×15×25	6 s (temporal resolution)
Parasoglou et al (35)	3D PCr imaging	3T	skeletal muscle	4.6×4.6×25	10 min
Parasoglou et al (62)	3D dynamic PCr imaging	3T	skeletal muscle	9.2×9.2×50	24 s (temporal resolution)
		7T	skeletal muscle	8×8×25	24 s (temporal resolution)

A summary of some typical static and dynamic PCr imaging studies in humans is listed in Table 1.1. In addition to PCr imaging, P_i (87) and PCr/ATP ratio (92) can also be quantified by ^{31}P MRI. An interleaved excitation scheme further enables simultaneous quantification of PCr and Pi. pH can be also derived from the phase difference between PCr and Pi (93). Moreover, magnetization transfer (MT) can also be incorporated into this chemical selective imaging approach for the mapping of the CK enzyme reaction rate (89,90). However, these approaches have not been widely applied to preclinical studies yet due to the much higher demand of spatial resolution in small animals.

1.2.5. MRSI Methods

MRSI, also known as chemical shift imaging (CSI), is the combination of MRS and MRI. Compared with non-localized MRS and SVS techniques, MRSI enables acquisitions of spectra from multiple voxels simultaneously. However, MRSI is much more time consuming than MRI or MRS due to the encoding of the entire k-t space, rather than only k-space in MRI and only t-space in MRS. In addition, species with low MR sensitivity and in vivo concentrations, such as ^{31}P metabolites, require a large number of signal averages to achieve satisfactory SNR.

Conventional MRSI employs phase-encoding gradients to encode the spatial distribution of the spins and leaves the readout direction for spectral encoding (82,94–97). Therefore, data points in k-t space are acquired line by line and the total acquisition time equals to the multiplication of TR, number of phase encoding steps, and number of signal average. This approach has been widely used in ^{31}P studies in brain (98–101), heart (102,103), liver (104–106), kidney (107), and skeletal muscle (108–111), and proved to be feasible to investigate metabolic heterogeneity in these organs. A limitation of this approach is cross-voxel contamination due to the Fourier transform point spread function (PSF), resulting in the loss of localization precision. A k-space weighted acquisition approach combined with post-acquisition filtering can be used to improve the PSF shape. A typical example of weighted k-space sampling is to only acquire a circular region in k-space and zero fill the outer regions, resulting in both improved PSF profile and reduced acquisition time (112). However, the phase encoding MRSI method is

not feasible if relatively high spatial resolution or temporal resolution is desired especially in dynamic studies.

There have emerged a variety of fast MRSI methods in the past decade. EPSI was proposed in the late 1990s to accelerate MRSI acquisition (113) and has been widely used in ^{1}H MRSI (114–118). The feasibility of EPSI in mapping ^{31}P metabolites was also demonstrated in human calf muscle and brain at 7T recently and reduced experiment time from ~55 min to 10 min compared with conventional ^{31}P MRSI (119). EPSI employs an oscillating gradient to collect a planar of data in one TR instead of one line of data points as in conventional MRSI, leading to significantly reduced number of phase encoding steps and thereby reduced acquisition time. A limitation of EPSI is the high demand on the performance of gradients. Ghosting artifacts due to imperfect bipolar gradients also cause problem in image quality. For ^{31}P MRSI, the lower gyromagnetic ratio compared to proton requires even higher gradient amplitude and slew rate to achieve the same resolution with the same sampling bandwidth.

In addition to EPSI, non-Cartesian encoding is another approach to accelerate acquisition by reducing number of phase encoding steps. Compared to conventional Cartesian MRSI, non-Cartesian trajectories, such as spiral (120), radial (121), and rosette (122), are able to cover more k-space in one acquisition, and then spectral domain is encoded with a shifted echo time, which corresponds to the acquired spectral bandwidth. Reconstruction of the data requires a process called regridding to interpolate data onto Cartesian space such that fast Fourier transform can be applied (123). Non-Cartesian MRSI has been successfully applied

to ^{1}H MRSI (122,124–126) and hyperpolarized ^{13}C MRSI studies (121,127–131). Some pioneer studies using spiral (132,133) and rosette (134) trajectories have shown the feasibility of this approach in ^{31}P MRSI for quantification of ^{31}P metabolites and mapping mitochondrial oxidative capacity in human skeletal muscle. An acceleration factor of 16~25 was achieved compared with conventional phase encoding MRSI in mapping ^{31}P metabolites at 7T (135).

Alternatively, there are also some approaches achieving acceleration by reducing TR, such as the ^{31}P MRSI method based on bSSFP framework (136). In conventional MRSI, either FID or spin-echo signals are acquired with the absence or presence of the refocusing RF pulse. The signal properties of these two acquisition modes are essentially equivalent to those in gradient-spoiled fast low angle shot (FLASH) and spin-echo MRI, respectively. Alternatively, bSSFP sequences serve as a candidate for ^{31}P MRSI due to its excellent SNR efficiency (137). Speck and colleagues first developed the ^{31}P MRSI technique based on bSSFP framework and demonstrated it in human skeletal muscles at 2T (136). In vivo results show 4~5 folds acceleration with the same SNR compared to FLASH-based MRSI methods (136). Later, a multi-echo bSSFP MRSI method was applied to ^{1}H and ^{31}P to further reduce the acquisition time (138). However, bSSFP requires short TR to minimize the banding artifact, and thus limits the achievable spectral resolution. The severe frequency-dependent spectral modulation also constrains the flexibility of acquisition parameters in order to avoid the resonances of interest falling in the null band, limiting the applications of this approach in both preclinical and clinical research (136).

In addition to reducing number of phase encoding steps and TR, prior knowledge of the image function can also be exploited to further enable data undersampling and hence acceleration in acquisition. Recently, a subspace approach called SPectroscopic Imaging by exploiting spatiospectral CorrElation (SPICE) based on partial separable (PS) model was proposed and applied to ^{1}H MRSI (139). Excellent SNR and spatial resolution was achieved with an acceleration factor of 10 compared with the conventional MRSI method (139). Because there are limited tissue types in the image object, SPICE takes advantage of the low-rank nature of the signal model and thereby allows for data undersampling. In brief, two datasets were acquired to significantly reduce the acquisition time: one with undersampled k-space and fully sampled t-space that can be acquired using phase-encoding MRSI method; the other with undersampled t-space and fully sampled k-space that can be acquired using EPSI method. Spatial and spectral information was then recovered by exploiting the spatial-spectral correlation of the acquired data in PS model (139). Without water or fat suppression as required in ^{1}H MRSI, ^{31}P MRSI can adopt the SPICE approach easily.

Despite the fast MRSI methods described above, other fast imaging strategies commonly used in proton MRI such as parallel imaging (140–142) and compressed sensing (143) are also promising to be combined with MRSI techniques to further accelerate the acquisition. For example, compressed sensing has been successfully applied to ^{1}H MRSI of the human brain (124) and ^{23}Na MRSI of the mouse heart (144).

In conclusion, ^{31}P MRS/MRI/MRSI provides a powerful and versatile tool to probe energy metabolism in vivo. The development of advanced hardware systems and novel reconstruction strategies in recent years brings enormous opportunities to ^{31}P MR techniques to extend its application in both clinical and preclinical studies with improved robustness and efficiency. Improved ^{31}P MR techniques will further enhance the understanding of underlying mechanisms of bioenergetics and physiological and pathological influences on energy metabolism in various organs.

1.3. Assessing Oxygen Metabolism Using ^{17}O MRS/MRI

1.3.1. Concept of ^{17}O MRI for Investigating Cerebral Oxygen Metabolism and Water Movement across the Blood-Brain Barrier (BBB)

As described in Chapter 1.1, oxygen gas is reduced to water to provide energy for ATP generation during oxidative phosphorylation in mitochondria. The use of ^{17}O-isotope labeled oxygen gas ($^{17}O_2$) enables in vivo ^{17}O MRS/MRI as a non-invasive tool to measure the metabolically generated $H_2{}^{17}O$ via the following reaction in mitochondria:

$$4H^+ + 4e^- + {}^{17}O_2 \leftrightarrow 2H_2{}^{17}O \qquad [1.3]$$

Similar to ^{15}O Positron Emission Tomography (PET) methods, when the ^{17}O-labeled oxygen gas is inhaled by the animal or human, it binds to hemoglobin in the blood and enters the brain through the arteries and blood circulation. Then, $^{17}O_2$ is metabolized in mitochondria of brain cells to produce $H_2{}^{17}O$. The production rate of $H_2{}^{17}O$ reflects the consumption rate of oxygen in brain tissue. Therefore, in

vivo assessment of cerebral metabolic rate of oxygen ($CMRO_2$) is enabled by monitoring the accumulation of metabolized $H_2{}^{17}O$ molecules directly using dynamic ^{17}O MRS/MRI.

In addition to oxygen utilization, water movement across the BBB and cerebral blood flow (CBF) can also be assessed using ^{17}O-labeled exogenous tracers (e.g., $H_2{}^{17}O$) (145–147). During a bolus injection of $H_2{}^{17}O$, $H_2{}^{17}O$ is brought to the brain by the CBF, resulting in an initial rapid increase in $H_2{}^{17}O$ concentration in brain tissues. Then the concentration of $H_2{}^{17}O$ in the brain starts to decrease driven by CBF; meanwhile some $H_2{}^{17}O$ molecules are brought back to the brain from the body by blood recirculation. These two processes give rise to a net effect of $H_2{}^{17}O$ washout and finally achieve a new steady-state of $H_2{}^{17}O$ concentration in the brain. Hence, assessment of CBF and water movement across BBB can be realized by monitoring the uptake and washout of $H_2{}^{17}O$ in the brain with a bolus injection of $H_2{}^{17}O$ using dynamic ^{17}O MRS/MRI.

1.3.2. ^{17}O MR Properties

Unlike the radioactive ^{15}O isotope used in PET, ^{17}O is a stable and non-radioactive isotope of oxygen with a magnetic moment that can be detected by MR. However, ^{17}O has a natural abundance of only ~0.037%. In addition to the extremely low natural abundance, the gyromagnetic ratio of ^{17}O is 7.4 times lower than that of protons, leading to the lowest MR sensitivity among all nuclei that are commonly used in research and clinical studies.

^{17}O has an electric quadrupolar moment and a spin quantum number of greater than 1/2 (I=5/2), which gives rise to extremely short relaxation times of

$H_2{}^{17}O$ (148–150). Studies in rat brain in vivo showed that the longitudinal and transverse relaxation times of natural abundance $H_2{}^{17}O$ are on the order of a few milliseconds and are field independent (T_2 = 3 ms, T_2* = 1.8 ms at both 4.7T and 9.4T; T_1 = 4.5 ms at 4.7T versus 4.8 ms at 9.4T) (149).

In order to improve SNR, increasing the field strength is one of the most efficient ways for the detection of ^{17}O signals. Unlike protons, the SNR gain at higher fields for ^{17}O is not compromised by longer relaxation times. In addition, the field independent short T_1 of $H_2{}^{17}O$ enables rapid acquisition with short TR and allows for rapid signal averages. The SNR gain for ^{17}O at 4.7T, 9.4T, and 16.4T has been investigated thoroughly (149,151). The SNR at 9.4T was found to be 4.4- and 4.1-fold higher than that at 4.7T in the NaCl solution and in the rat brain (149). 16.4T gives rise to a more than 2.7-fold higher SNR than 9.4T (151). These studies suggest the feasibility to map cerebral oxygen metabolism in vivo with high image quality at ultra-high fields.

An advantage of ^{17}O MRI for mapping $CMRO_2$ compared with ^{15}O PET is the invisibility of $^{17}O_2$ to MR. ^{15}O PET approaches require a complicated model and complex experimental procedures to derive $CMRO_2$ because ^{15}O signals from both $^{15}O_2$ and $H_2{}^{15}O$ are detected and cannot be distinguished (152,153). In contrast, the $^{17}O_2$ molecule is undetectable in MR because it is strongly paramagnetic due to the unpaired electrons (150). Therefore, MR only detects $H_2{}^{17}O$ without compounding signals from $^{17}O_2$, leading to a simplified model and straightforward experimental procedures to map $CMRO_2$ in vivo.

1.3.3. Quantification of $CMRO_2$ in Small Animals

As shown in Figure 1.2, the changes in $H_2{}^{17}O$ concentrations in the brain tissue during a brief period of $^{17}O_2$ inhalation are contributed by three components. The first is the metabolically generated $H_2{}^{17}O$ from $^{17}O_2$ through oxidative metabolism in mitochondria of the brain cells. The second is washout of the $H_2{}^{17}O$ from the brain driven by CBF. The third is the $H_2{}^{17}O$ brought back to brain from the body through blood recirculation. Thus, the mass balance of $H_2{}^{17}O$ in the brain tissue can be derived as follows (150),

$$\frac{dC_b(t)}{dt} = 2\alpha f_1 CMRO_2 + f_2 CBF\big(C_a(t) - C_v(t)\big) \qquad [1.4]$$

where $C_b(t)$, $C_a(t)$, and $C_v(t)$ are the $H_2{}^{17}O$ concentrations in brain tissue, arterial blood, and venous blood, respectively. α is the ^{17}O enrichment fraction that can be treated as a constant for small animals. f_1 and f_2 are unit conversion factors.

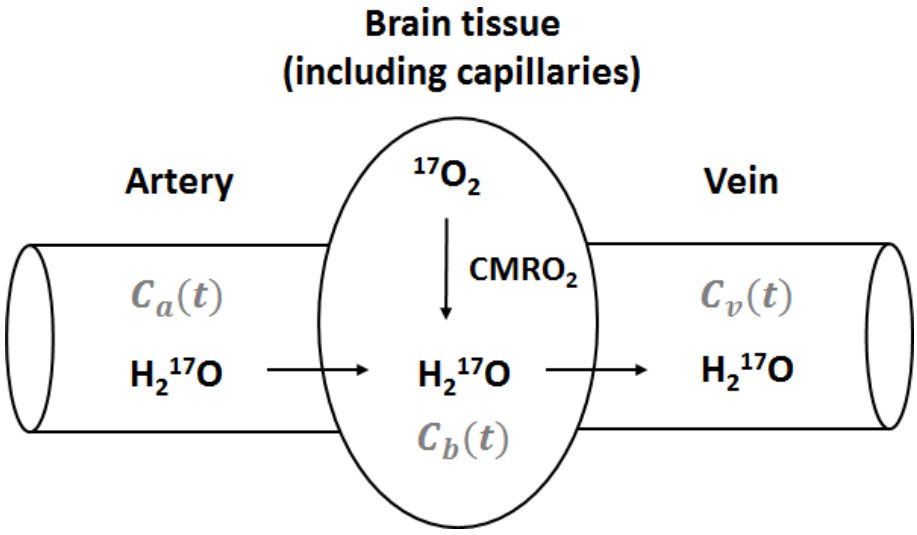

Figure 1.2. Schematic illustration of the model for quantification of $CMRO_2$.

It has been shown that during a short period of inhalation (2~4 min) for small animals, the model can be simplified as the following equation (154–156),

$$\frac{dC_b(t)}{dt} = 2\alpha CMRO_2 + CBF\left(C_a(t) - \frac{C_b(t)}{k_1}\right) \quad [1.5]$$

where k_1 is a constant, $C_a(t)$ and $C_b(t)/k_1$ are canceled out. Therefore, $CMRO_2$ is proportional to the linear production rate of metabolically generated $H_2{}^{17}O$ during inhalation, which is measured directly by ^{17}O MRI.

Note that the simplified model above is no longer appropriate for the quantification of $CMRO_2$ in humans because it takes much longer time for ^{17}O fractional enrichment of oxygen gas in the human artery blood to reach steady-state due to the relatively low respiration rate as compared to small animals. Therefore, α cannot be treated as a constant and an alternate model should be used (157).

1.3.4. ^{17}O MRS/MRI Methods

The available MR methods to detect ^{17}O signals in the brain of human and small animals are limited due to the unique MR properties of ^{17}O, i.e., the extremely short T_2, low MR sensitivity, etc. Currently there are mainly two approaches for imaging $H_2{}^{17}O$ directly using ultra-short echo time sequences. One is ^{17}O MRSI approach using the 3D Fourier Series Window MRS imaging technique (154,158); the other applies non-Cartesian encoding sequences, i.e., the flexible Twisted Projection Imaging (flexTPI) acquisition and density-adapted 3D radial sequence that are commonly used for ^{23}Na imaging (159,160).

The 3D ^{17}O MRSI approach has been widely applied in preclinical studies to quantify $CMRO_2$ and CBF. It has been used extensively to evaluate cerebral metabolic activity in rats (161), healthy cats (162), and mice (156,163). Water dynamics and CBF can also be assessed using this approach by observing the kinetics of $H_2{}^{17}O$ signal either from a bolus injection of $H_2{}^{17}O$ or from metabolically produced $H_2{}^{17}O$ from inhaled $^{17}O_2$ in small animals (154,156,164). Using this approach, Zhu et al. reported a temporal resolution of 11 s with a voxel size of 40 μL (15 μL nominal) at 11.7 T in an inhalation study on stroked mice (156). In another study, Cui and colleagues quantified $CMRO_2$ in mouse brain at 16.4 T with a temporal resolution of 15.4 s and a voxel size of 26 μL (9 μL nominal) (163).

Alternatively, non-Cartesian encoding methods are commonly used in clinical ^{17}O studies (157,165,166). This approach was initially applied to sodium imaging and then was adopted by ^{17}O studies. These methods have achieved a spatial resolution of 8 to 8.5 mm and a temporal resolution of 40 to 50 s in humans at high field.

The Cartesian encoding MRSI method is easy to implement on preclinical scanners and does not require high gradient amplitude. On the other hand, the implementation of the non-Cartesian gradient waveforms and the image reconstruction process are relatively complicated; however, the non-Cartesian encoding approach potentially provides more flexibility to combine with advanced sampling and image reconstruction schemes to allow for significant undersampling and thus improved spatial/temporal resolutions.

1.4. Motivations and Objectives

Hetero-nuclei MRI in general is challenging due to the low in vivo concentrations and low MR sensitivity. Long acquisition time is usually required even with low spatial resolution. ^{31}P MRS has been used extensively to investigate mitochondrial function in heart (38,43), brain (24,167), liver (168), and skeletal muscle (21) associated with various diseases. However, the non-localized spectroscopy approach cannot distinguish the heterogeneity in metabolic alterations among different muscle groups. ^{31}P MRSI is a promising method that can detect spatial and spectral variations, but it is still challenging especially for dynamic applications, such as ischemia-reperfusion or exercise-recovery studies in skeletal muscle due to the low temporal resolution. On the other hand, ^{17}O MRS/MRI plays an important role in assessing cerebral oxygen metabolism. However, the current techniques using Cartesian MRSI or non-Cartesian MRI approaches still suffer from partial volume effects due to the low spatial resolution.

The studies in this thesis aimed to develop fast hetero-nuclei MRI methods for metabolic imaging in small animal models at high fields. In particular, this thesis focused on fast ^{31}P MRSI and ^{17}O MRI approaches with non-Cartesian encoding schemes that assess mitochondrial function in skeletal muscle and cerebral oxygen metabolism/water movement across BBB, respectively. Chapter 2 describes the evaluation of mitochondrial oxidative capacity in type 2 diabetic rats using ^{31}P MRS with an ischemia-reperfusion protocol. Chapter 3 presents the development of a fast dynamic ^{31}P MRSI method using SPICE. Proof-of-concept demonstration was performed in rat skeletal muscle using an ischemia-reperfusion protocol. In

Chapter 4, a dynamic ^{17}O MRI method using golden-angle radial acquisition combined with k-space weighted image contrast (KWIC) reconstruction was developed and validated in simulation studies. The in vivo applications of the dynamic ^{17}O MRI method are presented in Chapter 5. First, this method was demonstrated in a mouse model with glioblastoma (GBM) to assess the water movement across BBB after a bolus in injection of ^{17}O-labeled water. Second, the ^{17}O MRI approach was applied to a mouse model of middle cerebral artery occlusion (MCAO) in ^{17}O-labeled gas inhalation experiments to assess cerebral oxygen metabolism in vivo. Chapter 6 summarizes the conclusions of this thesis and discusses optimizations in experimental design, signal acquisition, and future directions in dynamic imaging techniques for hetero-nuclei MRI. The success of this work will pave the way for fast metabolic imaging using ^{31}P and ^{17}O MRI techniques and allow for the assessment of metabolic alterations associated with various diseases, such as diabetes, ischemic stroke, etc.

Chapter 2. Mitochondrial Function Assessed by ^{31}P MRS and BOLD MRI in Non-obese Type 2 Diabetic Rats

This chapter describes a study that aimed to characterize age-associated changes in skeletal muscle bioenergetics by evaluating the response to ischemia-reperfusion in the skeletal muscle of the Goto-Kakizaki (GK) rats, a rat model of non-obese type 2 diabetes (T2D). ^{31}P MRS and blood oxygen level dependent (BOLD) MRI were performed on the hindlimb of young (12 weeks) and adult (20 weeks) GK and Wistar (control) rats. ^{31}P-MRS and BOLD-MRI data were acquired continuously during an ischemia and reperfusion protocol to quantify changes in phosphate metabolites and muscle oxygenation. The time constant of phosphocreatine recovery, an index of mitochondrial oxidative capacity, was not statistically different between GK rats (60.8±13.9 s in young group, 83.7±13.0 s in adult group) and their age-matched controls (62.4±11.6 s in young group, 77.5±7.1 s in adult group). During ischemia, baseline-normalized BOLD-MRI signal was significantly lower in GK rats than in their age-matched controls. These results suggest that insulin resistance leads to alterations in tissue metabolism without impaired mitochondrial oxidative capacity in GK rats.

2.1. Introduction

T2D is a common form of diabetes mellitus. It is characterized by hyperglycemia as a consequence of insulin resistance and relative insulin deficiency (169). Skeletal muscle is the major site of insulin-mediated glucose uptake in the postprandial state (170). Emerging evidence suggests that impaired

muscle metabolism plays a major role in the pathogenesis of T2D, and reducing mitochondrial oxidative damage may be a therapeutic target for preventing reduction in muscle mitochondrial function in T2D (171). Metabolic dysfunction in skeletal muscle had been documented in the development of T2D (7,59,172–174). Previous studies have reported reduced mitochondria electron transport chain activity (173), low mitochondrial content (174,175), and smaller skeletal muscle mitochondria (173) in T2D patients. A defect in mitochondrial oxidative phosphorylation in both diabetic patients and animal models of T2D has also been reported (7,59). However, conflicting results have also been reported that suggest normal mitochondrial function in T2D patients (175,176).

One key parameter used in evaluating mitochondrial function is the mitochondrial oxidative capacity. MRI/MRS can provide noninvasive and dynamic tools that are well suited to assessing mitochondrial function in vivo. ^{31}P MRS offers direct quantification of the high-energy phosphate metabolites such as ATP and PCr (59). In particular, monitoring the depletion and resynthesis of PCr during exercise-recovery or ischemia-reperfusion by dynamic ^{31}P MRS allows the assessment of mitochondrial oxidative capacity in the muscle (8,12). Furthermore, BOLD MRI allows the assessment of muscle oxygenation in vivo by detecting changes in the oxygenated versus deoxygenated hemoglobin ratio (177). The technique has been used to evaluate muscle oxygenation following arterial occlusion (178). Simultaneous assessment of mitochondrial function and tissue oxygenation may lead to a more comprehensive understanding of the energetics of skeletal muscle in T2D. In addition, these noninvasive approaches enable

longitudinal studies aimed at delineating the time course of metabolic changes in T2D.

To date, most studies using animal models of T2D have focused on obese T2D rodents (179). While insulin resistance is frequently associated with obesity, not all T2D patients are obese. Hence, a lean animal model of T2D is of value to studying mitochondrial function in non-obese T2D. The Goto-Kakizaki (GK) rats, which were created by repetitive breeding of Wistar rats with the poorest glucose tolerance, develop peripheral insulin resistance without elevated level of plasma fatty acids (180). They have thus been used in the investigation of various aspects of T2D not related to obesity. Impaired microvascular function has been reported in GK rats (181), however, in vivo data regarding mitochondrial function in this animal model are still scarce. In a recent study, Macia et al characterized PCr recovery following a 6-min electrical stimulation protocol in the gastrocnemius muscle of GK rats. While no change in mitochondrial oxidative capacity was observed in GK rats, it is not clear whether other aspects of muscle metabolism, e.g., tissue oxygenation, also remained the same. Further, energy metabolism during the progression of T2D has not been characterized.

The purpose of this study was to examine whether the T2D condition and its progression slows PCr recovery kinetics and alters tissue oxygenation. We sought to assess metabolic response of the skeletal muscle to ischemia-reperfusion in non-obese GK rats. Interleaved ^{31}P MRS and BOLD MRI acquisitions were performed continuously during an ischemia and reperfusion protocol to evaluate mitochondrial oxidative capacity and muscle oxygenation. Progression of the

disease was investigated by conducting experiments on both young and adult GK rats and their age-matched controls.

2.2. Materials and Methods

2.2.1. Animals

Non-obese male GK rats (Charles River Laboratories, the United States) were scanned at about 12 weeks as the young group (n=7). The same rats were scanned at about 18 weeks as the adult group (n=7). Wistar rats (Charles River Laboratories, the United States) were scanned at about 13 weeks as the young control group (n=6), with five of the same rats scanned at about 20 weeks as the adult group. Additional four adult Wistar rats were also scanned at about 20 weeks of age (n=9 in total). The animal protocol was approved by the Institutional Animal Care and Use Committee of the Case Western Reserve University.

2.2.2. Experimental Protocol

Animals were anesthetized with isoflurane (1.5–2.5%) and placed in a cradle in the lateral position. Respiration rate and body temperature were monitored during the experiments. The body temperature was maintained at 35.5±0.5°C by blowing hot air into the MRI scanner through a feedback control system. An inflatable cuff was placed at the thigh of the rat. Ischemia was induced by occluding the femoral artery with the inflated cuff. After the MRI scan, the blood glucose concentration was determined using a glucometer with blood samples obtained from tail vein.

2.2.3. MRI and MRS Studies

All experiments were conducted on a 9.4T Bruker Biospec horizontal scanner (Bruker Biospin Inc., Billerica, MA). A Bruker ^{1}H volume coil was used for ^{1}H image acquisition. An in-house built, 2-cm diameter ^{31}P saddle coil was placed around the calf muscles to acquire the ^{31}P spectra. The leg was secured to the ^{31}P coil that was attached to the cradle to avoid potential motion during the experiment. To minimize the coupling between the ^{1}H and the ^{31}P coils, the orientation of the two coils were adjusted such that their B_1 fields were perpendicular to each other.

Scout ^{1}H images were acquired to determine the position of the lower leg. Automatic, localized shimming was performed on an isotropic voxel of 20×20×20 mm^3 that covered the entire lower leg using a PRESS sequence. A proton linewidth of 120 to 140 Hz was achieved after the shimming. The experimental setup and shimming took about 15 to 20 min on average.

128 ^{31}P spectra were acquired, followed by the acquisition of three BOLD images, leading to a total acquisition time of ~7 min at baseline. Ischemia was then induced by inflating the cuff to 300 mmHg pressure within 1 to 2 s. After 26 min of ischemia, perfusion was resumed immediately by deflating the cuff. During ischemia and reperfusion, interleaved ^{31}P MRS and BOLD MRI acquisitions were performed continuously. ^{31}P MRS scan consisted of the acquisition of 160 single-average ^{31}P spectra. Each acquisition used a hard excitation pulse with a flip angle of 60°, followed by the acquisition of FID with 600 points and a spectral width of 6 kHz. A 2-s inter-scan delay (TR) was used, leading to a total acquisition time of

5 min 22 s. BOLD images of an axial slice were acquired using the FLASH sequence. Imaging parameters were: TR, 500 ms; TE, 7 ms; flip angle, 40°; FOV, 4×4 cm^2; matrix size, 128×128; number of averages, 1. Total acquisition time was 64 s for each BOLD scan. The interleaved ^{31}P and BOLD acquisitions were repeated four times each during ischemia and reperfusion, respectively. The experimental protocol and MR acquisition scheme are illustrated in Figure 2.1.

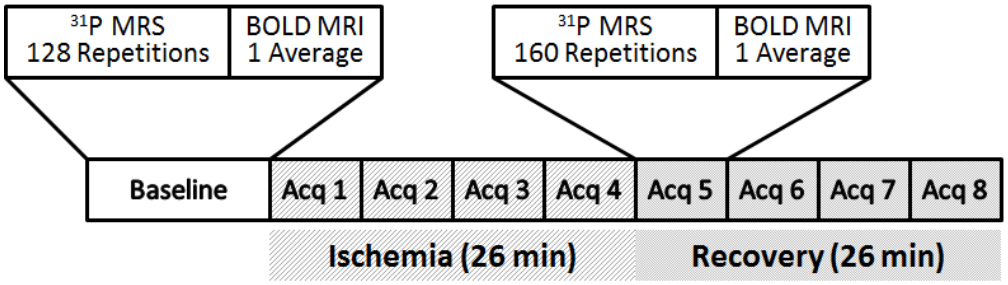

Figure 2.1. Data acquisition scheme. Interleaved ^{31}P MRS and BOLD MRI acquisitions were performed at baseline and during ischemia and reperfusion. The acquisition block was repeated four times each during ischemia and reperfusion, respectively.

2.2.4. Data Analysis

^{31}P MRS data were analyzed using in-house developed software written in MATLAB (Mathworks, Natick, MA). Four ^{31}P spectra were averaged to achieve an adequate SNR of ~7 for PCr peak at baseline. The averaged spectra were zero-padded to 2048 points and a 30 Hz line-broadening was applied before Fourier transform. The transformed spectra were phase-corrected manually using zero- and first-order correction. The area under PCr was calculated by integration.

Baseline PCr level was calculated as the peak area from the averaged spectra acquired at baseline. PCr level during the entire ischemia-reperfusion

period was normalized to the baseline value. Upon cuff inflation, the initial slope of %PCr depletion was quantified as an index of resting metabolic rate. During reperfusion, the time constant of PCr recovery was estimated by fitting a mono-exponential function to the PCr recovery curve (44). Although the use of a 2-s TR introduced signal saturation, the kinetics of the normalized PCr signal was not affected. In addition to the time constant, the initial rate of %PCr recovery was also quantified by calculating the initial slope of %PCr recovery.

P_i levels were quantified by averaging 128 spectra acquired at the baseline and at the end of reperfusion, respectively. pH values at baseline and at the end of ischemia and reperfusion were calculated from the chemical shift of P_i relative to PCr (δ_{P_i}) according to Eq [1.2] (49).

BOLD images were also processed using MATLAB-based software (Mathworks, Natick, MA). Regions of interest (ROI) that encompassed the tibialis anterior and the gastrocnemius muscles were segmented manually. Signal intensity in these two ROIs, as well as in the entire calf muscle, was calculated as the mean value of all pixels within the ROIs. The signal was then normalized to the corresponding baseline values.

2.2.5. Statistics

Results are reported as mean ± standard deviation. Two-way analysis of variance (ANOVA) was used for data comparison. If statistical differences were detected, multiple pairwise comparisons were performed using two-tailed student's t-test. Significant difference was accepted at $p<0.05$.

2.3. Results

2.3.1. Animal Characteristics

The age, body weight, and blood glucose level for young and adult groups are summarized in Table 1. The body weight for young and adult GK rats was significantly lower than their age-matched controls. Blood glucose level was significantly higher than that of the age-matched controls. Young and adult GK rats were scanned at 12.2 ± 0.3 weeks and 18.1 ± 0.2 weeks, respectively. The age at which the young and adult Wistar rats were scanned was 13.8±0.1 weeks and 20.4±1.4 weeks, respectively.

Table 2.1. Animal characteristics.

	Young		**Adult**	
	Control	**GK**	**Control**	**GK**
Age (weeks)	13.8±0.1	12.2±0.3	20.4±1.4	18.1±0.2
Body weight (g)	389.1±16.2	293.4±37.4*	507.5±32.7	356.5±19.9*
Blood glucose level (mg/ml)	123.8±6.1	227±7.5*	108±23.2	204±6*

*$p<0.05$, young versus adult

2.3.2. ^{31}P MRS

Representative ^{31}P spectra at baseline, end of ischemia, and end of reperfusion from an adult control rat are shown in Figure 2.2a. Each spectrum is an average of four acquisitions, giving rise to a temporal resolution of 8 s. PCr depletion and P_i accumulation were evident during ischemia. A representative time

course of PCr changes during the entire experimental protocol is shown in Figure 2.2b. PCr showed progressive decrease during the entire period of ischemia. There was no difference in the initial rate of %PCr depletion among the four experimental groups (2.9 ± 0.2 versus 2.7 ± 0.4 %/min for young and adult controls; 2.8 ± 0.2 versus 2.7 ± 0.2 %/min for young and adult GK rats). Upon reperfusion, PCr was rapidly resynthesized, accompanied by the decrease of P_i to near baseline level.

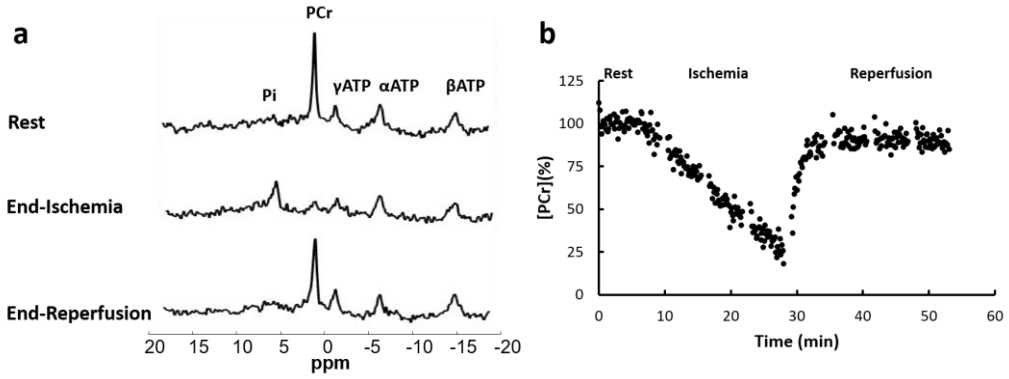

Figure 2.2. Representative ^{31}P spectra at baseline, end of ischemia, and end of reperfusion **(a)** and changes in PCr concentration **(b)** during ischemia-reperfusion with a temporal resolution of 8 s.

PCr levels at the end of ischemia and reperfusion are shown in Figures 2.3a and 3b, respectively. All four groups of rats showed significant but similar levels of PCr depletion at the end of ischemia (Figure 2.3a). PCr levels at the end of reperfusion ranged from 86% to 95%, while the adult GK rats showed significantly lower PCr recovery compared to their age-matched controls (Figure 2.3b). No statistically significant interaction between the age and animal strain was detected by ANOVA. Consistent with the incomplete PCr recovery, there was an increase in P_i at the end of reperfusion. Again, adult GK rats showed the highest increase in

P_i compared to their age-matched controls (8.5% versus 4.6%). P_i increase in young GK and control rats was 4.3% and 5.1%, respectively.

Figure 2.3c shows the time constant of PCr recovery at the onset of reperfusion. There was no difference between the GK rats and their age-matched controls. However, the adult rats showed prolonged PCr recovery kinetics for both GK and control rats ($p<0.05$). There was no statistically significant interaction between the age and animal strain. Consistent with increased time constant of PCr recovery, both adult and GK rats also showed a decrease in the initial rate of %PCr recovery: 1.2 ± 0.2 versus 0.9 ± 0.1 %/s for young and adult controls, and 1.3 ± 0.3 versus 0.9 ± 0.4 %/s for young and adult GK rats, respectively ($p<0.05$).

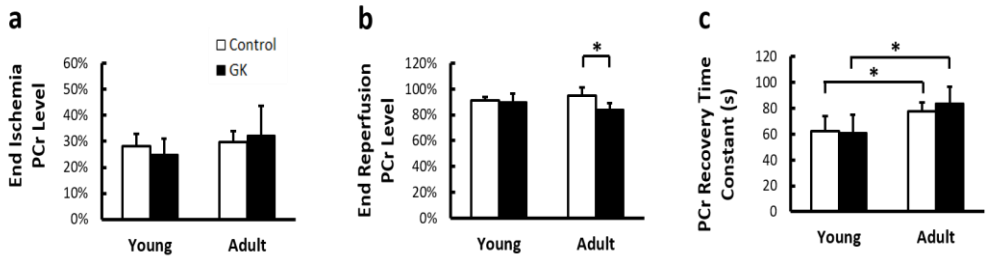

Figure 2.3. Metabolic response to ischemia and reperfusion measured by ^{31}P MRS. **a**. Normalized PCr level at the end of ischemia; **b.** Normalized PCr level at the end of reperfusion; **c**. Time constant of PCr recovery during reperfusion.

As expected, there was a significant reduction in pH during ischemia, and it returned to the baseline level after reperfusion (Figure 2.4). No significant difference in pH was found among all four groups.

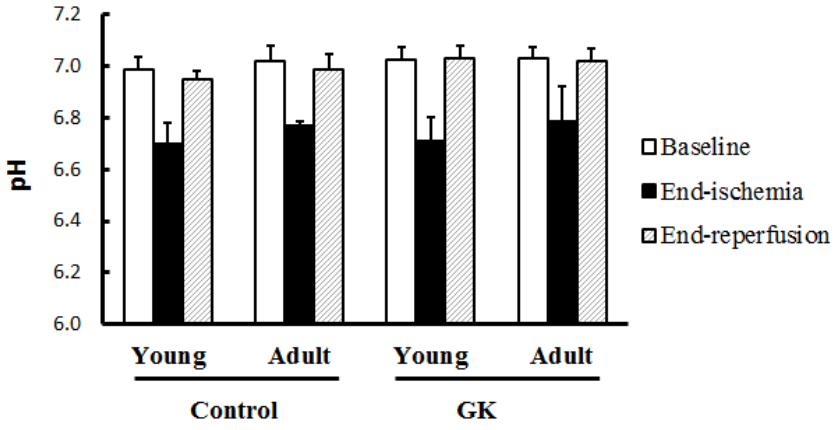

Figure 2.4. Intracellular pH at baseline, end of ischemia, and end of reperfusion.

2.3.3. BOLD MRI

Figure 2.5 shows baseline-normalized BOLD signal intensity during ischemia and reperfusion. Ischemia induced a significant decrease in BOLD signal intensity, suggesting decreased tissue oxygenation. Compared to their age-matched controls, adult GK rats showed significantly lower BOLD signal intensities during ischemia-reperfusion, suggesting a more pronounced reduction in tissue oxygen level in the entire calf muscle (Figure 2.5b). The difference in BOLD signal between the GK rats and the controls was predominantly caused by the difference in gastrocnemius muscle (Figure 2.5c). In contrast, BOLD signal in tibialis anterior muscle was similar among all groups during ischemia and reperfusion (Figure 2.5d).

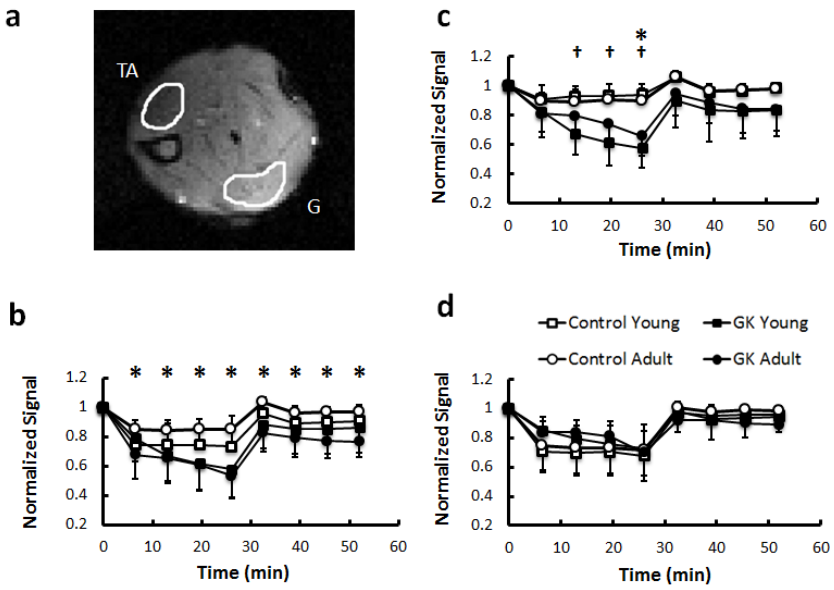

Figure 2.5. Tissue oxygen measured by BOLD MRI. **a.** A representative BOLD image acquired at baseline with ROIs of tibialis anterior (TA) and gastrocnemius (G) muscles; **b-d**. Normalized BOLD signal changes during ischemia and reperfusion in all muscles **(b)**, gastrocnemius **(c)**, and tibialis anterior **(d)**. *p<0.05, adult GK rats versus adult controls; †p<0.05, young GK rats versus young controls.

2.4. Discussion and Conclusions

In the current study, we characterized *in vivo* metabolic and physiological alterations in response to ischemia and reperfusion in the skeletal muscle of GK rats, a rat model of non-obese T2D. GK rats were shown as one of the best animal models of non-obese T2D (182). In the present study, both young and adult GK rats showed significantly higher blood glucose levels compared to their age-matched controls, suggesting that insulin-resistance was present at an early age. The time constant of PCr recovery, an index of mitochondrial oxidative capacity, was not significantly different between GK rats and their age-matched controls.

However, we observed a significant reduction in PCr recovery level after ischemia in adult GK rats. Interestingly, ischemia induced a more pronounced reduction in BOLD signal in GK rats, suggesting reduced muscle oxygenation in gastrocnemius muscle during ischemia and reperfusion.

It has been shown that skeletal muscle oxidative capacity can be quantified from the kinetics of PCr recovery following a period of PCr depletion (56). In a recent study using a 6-min stimulated maximal isometric contraction protocol (60), Macia and colleagues observed that the initial rate of PCr resynthesis after the stimulation was not different between the GK rats and the controls. In our current study, PCr depletion was induced by a 26-min ischemia protocol. The ischemia protocol induced a similar level of PCr depletion compared to the stimulation study by Macia et al. Further, the time constant of PCr recovery during reperfusion was also similar between the GK rats and the controls in both age groups, suggesting unaltered mitochondrial oxidative capacity. Given that GK rats in both age groups were insulin-resistant but showed similar mitochondrial oxidative capacity as the controls, it can be expected that pre-diabetic GK rats will also show normal oxidative capacity. These results confirm the previous observation that mitochondrial impairment is not the causative factor for the development of insulin resistance in GK rats.

Oxygen deficiency during ischemia also induced a significant decrease in intracellular pH. Previous studies have shown that the time constant of PCr recovery after its depletion is inversely related to intracellular pH (58,183,184). Possible mechanisms include direct impact of acidosis on mitochondrial respiration

(47), ATP consumption during pH restoration (185), and the modulation of CK equilibrium (186–188). In their recent study on GK rats (60), Macia and colleagues reported an intracellular pH of 6.3 to 6.4 at the end of 6-min maximal isometric contraction. The subsequent PCr recovery showed a rate constant of 0.38 to 0.39 min^{-1}, corresponding to a time constant of 154 to158 s. In our current study, the ischemia-induced pH decrease was much less, ranging from 6.7 to 6.8. As a result, the time constant of PCr recovery was much shorter, from 60 to 80 s. While these results support the negative correlation between the time constant of PCr recovery and intracellular acidosis, it is important to note that the measured PCr recovery kinetics still deviated from that measured under physiological pH, and thus was impacted by both mitochondrial oxidative capacity and proton clearance. Future studies can use a shorter duration of ischemic period to minimize the effect of acidosis.

Previous studies on lean diabetic patients using ^{31}P MRS have documented decreased ATP synthesis at resting state and during insulin-stimulation (7). Reduction in the number and size of muscle mitochondria has also been documented in obese T2D patients (173), as well as the lean insulin-resistant offspring of T2D patients (189). These observations have led to the hypothesis that mitochondrial deficiency may be responsible for insulin resistance (172,190). However, normal PCr recovery after exercise/stimulation was also observed in both T2D patients and animal models of obese T2D (176,191). Hence, the causal association between mitochondrial dysfunction and the development of insulin resistance remains to be elucidated. The normal mitochondrial oxidative capacity

in GK rats supports the notion that insulin resistance is not necessarily associated with impaired mitochondrial oxidative capacity in T2D. On the other hand, we observed a significant reduction in post-ischemia PCr level in adult GK rats. Consistent with PCr reduction, GK rats also showed a more pronounced increase in P_i at the end of reperfusion. Previously, incomplete PCr recovery has been observed in normal Wistar rats after a long period of ischemia (6 hours) (54,192). However, the duration of ischemia in the current study was much shorter. While one cannot rule out the possibility of metabolic dysfunction, the observed reduction in end-reperfusion PCr level in adult GK rats may also be caused by a deficit in oxygen delivery, as vascular impairment and lower microvascular oxygen pressure have been observed in adult GK rats (181,193).

Compared to the control rats, both young and adult GK rats also showed a more pronounced decrease in the normalized BOLD signal during ischemia. In general, BOLD signal depends on both blood oxygenation and blood volume (177). During ischemia induced by cuff-inflation, change in blood volume was minimal. Hence, the observed changes in BOLD signal are more likely associated with altered muscle oxygenation. The differences in baseline normalized BOLD signal could be caused by either a difference at the baseline (the denominator), or by a difference during ischemia (the numerator). A previous study has reported lower baseline microvascular oxygen pressure in GK rats (181), possibly caused by vascular impairment (193). This reduction in baseline muscle oxygenation in GK rats might have given rise to more pronounced reduction in normalized BOLD signal during ischemia observed in the current study. Alternatively, this reduction

may also reflect increased oxygen extraction by GK rats during ischemia. Impaired glucose uptake in T2D can lead to increased fatty acid utilization for ATP generation, which consumes more oxygen to fuel the oxidation. Indeed, increased fat oxidation has been reported in T2D patients and obese individuals with insulin-resistant (194). Hence, the more pronounced BOLD signal reduction in GK rats during ischemia can also be associated with increased fat oxidation. Which is the dominant mechanism that leads to the observed reduction in normalized BOLD signal in GK rats needs further investigation. Furthermore, the time course of BOLD signal recovery immediately after the onset of reperfusion can also provide important insight into the relationship between tissue oxygenation and muscle energetics.

With measurements of metabolic response from different muscles, BOLD MRI also provided assessment of heterogeneous alterations in muscle metabolism. Interestingly, gastrocnemius muscle in GK rats showed more pronounced BOLD signal reduction during ischemia-reperfusion compared to the controls. In contrast, oxygen level in tibialis anterior muscle was similar between GK rats and the controls. Comparing to the tibialis anterior muscle, gastrocnemius muscle is predominantly glycolytic type IIb fibers in rats (195–197). It was reported that glycolytic fibers are more insulin resistant in both rats (198) and humans (199). It is possible that gastrocnemius muscle with a larger fraction of glycolytic type IIb fibers is more likely to manifest metabolic alterations than the tibialis anterior muscle in T2D GK rats.

A limitation of the current study is that the ^{31}P MRS signals were acquired in a non-localized fashion and absolute concentrations of phosphate metabolites were not quantified. Hence, they represented the weighted averages from different muscle fiber types and cannot capture the heterogeneous alterations in mitochondrial function. Distinct differences in fiber-type composition exist among limb muscles, which give rise to metabolic diversity in response to stress and pathophysiological changes, as well as marked disparities in the recovery rate of PCr following its depletion (200). Recently, spectrally selective PCr imaging has been proved feasible in measuring post-exercise PCr resynthesis rate in the calf muscles of human subjects with adequate spatial and temporal resolution at 7T (88). While ^{31}P imaging of rodents is still challenged by the requirement of much higher spatial resolution, combining a spectrally selective PCr imaging method with other fast imaging approaches may enable the monitoring of the kinetics of PCr recovery in different muscle types *in vivo*.

In conclusion, we have observed unaltered mitochondrial oxidative capacity and decreased muscle oxygenation during ischemia-reperfusion in non-obese T2D GK rats. These findings provide evidence that insulin resistance is not accompanied by impaired mitochondrial oxidative capacity in this animal model. The lower BOLD signal during ischemia-reperfusion may be a consequence of impaired microvascular function and/or substrate alteration resulting in higher oxygen extraction. These findings provide the evidence that insulin resistance leads to altered oxygen utilization without impaired mitochondrial oxidative capacity in GK rats.

Chapter 3. High Resolution Dynamic ^{31}P MRSI of Ischemia-Reperfusion in Rat Hindlimb Using a Low-rank Tensor Model

Dynamic ^{31}P MRSI serves as a non-invasive tool to assess mitochondrial oxidative capacity in skeletal muscle during ischemia-reperfusion or exercise-recovery. However, ^{31}P MRSI with high spatial resolution requires long acquisition time which renders dynamic measurements impractical. This chapter describes a study that adapted a recently proposed low-rank tensor-based method for high resolution dynamic ^{31}P MRSI in preclinical studies. We present results from an in vivo ischemia-reperfusion experiment on a rat hindlimb with 15 s nominal temporal resolution and 0.75×0.75×1.6 mm^3 nominal spatial resolution, demonstrating the potential of the method for assessing mitochondrial function in different muscle types in small animal models.

3.1. Introduction

^{31}P MRS/MRI is a well-established tool to quantify the high-energy phosphate metabolites non-invasively, and is widely used to assess mitochondrial energy metabolism in vivo (201). In particular, monitoring the depletion and resynthesis of phosphocreatine (PCr) during exercise-recovery or ischemia-reperfusion by dynamic ^{31}P-MRS/MRI allows for the assessment of mitochondrial oxidative capacity in skeletal muscle (8,12). Most ^{31}P MRS studies have employed non-localized or single voxel techniques, rendering the assessment of heterogeneity in mitochondrial function impossible. ^{31}P MRSI provides a tool to evaluate spatial

variations in energy metabolism in vivo. However, current ^{31}P MRSI methods yield limited spatial resolution and require long acquisition time to achieve adequate SNR due to low metabolite concentrations.

In clinical studies, current ^{31}P MRSI methods yield a spatial resolution typically on the order of a cubic centimeter. In small animal models, it is desirable to achieve a resolution of a cubic millimeter to observe the variation between muscle groups. Several methods have been developed to provide increased spatial resolution, but at the cost of reduced temporal resolution, or spectral resolution and bandwidth (87,93,109,135). To retain the ability to measure mitochondrial oxidative capacity, the temporal resolution must be high enough to measure the PCr recovery rate during reperfusion, and estimation of metabolite concentrations and intracellular pH requires a spectral bandwidth/resolution of ~30 ppm/0.1 ppm.

Recently, a subspace based approach, called SPICE (SPectroscopic Imaging by exploiting spatiospectral CorrElation), has been proposed for fast ^{1}H-MRSI (139). SPICE employed a PS model to capture the spatiospectral correlation of the MRSI data (202–205). By exploiting the inherent correlations of high-dimensional data in multiple dimensions, recovery of spatiospectral information from undersampled data is enabled by special data acquisition scheme and reconstruction methods because high-dimensional MRSI data reside in a low dimensional subspace. This method was successfully applied to ^{1}H MRSI in human brain and achieved 3 mm isotropic resolution within 10 min acquisition (206–208). This approach was then applied to static and dynamic ^{31}P

MRSI in human calf muscles and achieved sub-centimeter spatial resolution with good SNR (209,210).

In this work, we adapted the low-rank tensor-based SPICE method for high resolution dynamic ^{31}P MRSI to small animal models. A hybrid data acquisition scheme was used for sparse sampling, including a set of "training" data with limited k-space coverage for the estimation of subspace structure and a set of "imaging" data with extended k-space coverage for image reconstruction. The potential of the method for observing spatiospectral variation during ischemia-reperfusion was demonstrated on rat hindlimb. 15 s nominal temporal resolution, 0.75×0.75×1.6 mm^3 nominal spatial resolution, 37 ppm/0.14 ppm spectral bandwidth/resolution were achieved at 9.4T.

3.2. Methods

3.2.1. Signal Model

The image function of dynamic MRSI is denoted as $\rho(x, f, t)$, where x, f, and t denotes spatial, spectral, and temporal axis, respectively. The variations of $\rho(x, f, t)$ in each dimension during a dynamic experiment can be represented by a linear combination of a finite number of basis functions because the tissue type in vivo is limited. For example, the spectral distribution of $\rho(x, f, t)$ can be approximated by a few number of resonances, such as PCr, ATP, and Pi. The temporal variations of $\rho(x, f, t)$ can be represented by a set of exponential functions with various time constants. Therefore, a PS model is used to represent the image function (202):

$$\rho(x,f,t) = \sum_{l=1}^{L}\sum_{m=1}^{M}\sum_{n=1}^{N} c_{l,m,n}\,\theta_l(x)\phi_m(f)\varphi_n(t) \qquad [3.1]$$

where $\{\theta_l(x)\}_{l=1}^{L}$, $\{\phi_m(f)\}_{m=1}^{M}$, $\{\varphi_n(t)\}_{n=1}^{N}$ denotes spatial, spectral, and temporal basis functions, respectively, and $\{c_{l,m,n}\}_{l,m,n=1}^{L,M,N}$ the corresponding model coefficients.

The PS model described in Eq [3.1] implies a low-rank tensor structure. After discretization, $\rho(x, f, t)$ can be expressed in the Tucker form (211):

$$\rho = \sum_{l=1}^{L}\sum_{m=1}^{M}\sum_{n=1}^{N} c_{l,m,n}\,\theta_l \cdot \phi_m \cdot \varphi_n \qquad [3.2]$$

where θ_l, ϕ_m, φ_n are vectors representing discretized $\theta_l(x)$, $\phi_m(f)$, $\varphi_n(t)$, and '$\cdot$' denotes the vector outer product. (L, M, N) is the rank of the tensor in Eq. [3.2]. In practice, L, M, and N are small numbers. This low-rank tensor model takes advantage of data redundancy in ρ, and exploits data correlation in multiple dimensions simultaneously.

3.2.2. Data Acquisition

A hybrid data acquisition scheme was used to exploit the PS property of the dynamic MRSI data. Similar to the original SPICE acquisition on ^{1}H MRSI, two sets of data, $\mathcal{D}_1$ and $\mathcal{D}_2$, were acquired shown in Figure 3.1.

$\mathcal{D}_1$ can be acquired either before or after the dynamic process. The acquisition parameters of $\mathcal{D}_1$ were designed to ensure that it captured the spectral variation at the needed bandwidth and spectral resolution. $\mathcal{D}_2$ can be acquired during the dynamic process, and was designed to provide only limited spectral information while capturing the spatial and temporal variation during the dynamic process. Taken separately, neither data set contained adequate information, however by fitting the data to the PS model as described by Ma et al. (209), an image with high spatial, spectral and temporal resolution can be reconstructed.

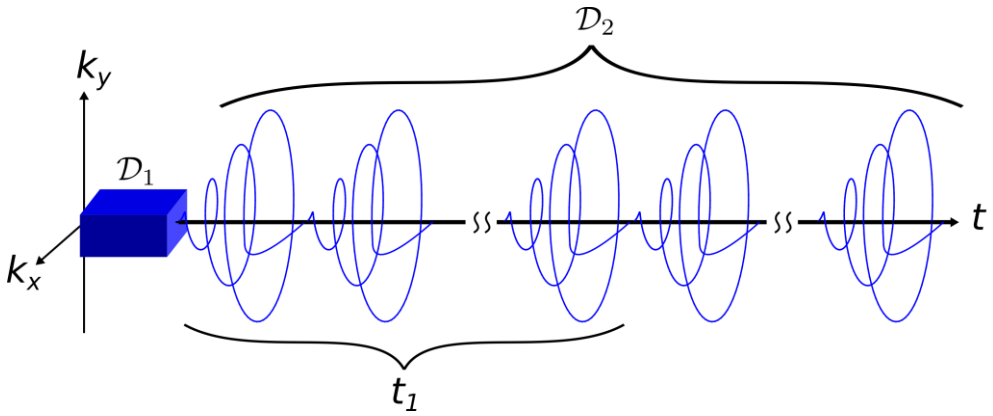

Figure 3.1. Acquisition scheme. We acquired two sets of data: $\mathcal{D}_1$ at baseline and $\mathcal{D}_2$ during ischemia-reperfusion. $\mathcal{D}_1$ had limited k-space coverage but dense temporal sampling and was used for estimating the spectral bases. $\mathcal{D}_2$ had extended k-space coverage but sparser temporal coverage and used for estimating the time-varying spatial distributions. Data from adjacent spiral shots were grouped into single time frames with limited spectral encoding. The first frame, t_1 is shown in the figure.

3.2.3. Data Processing

In this study we performed image reconstruction by solving the following optimization problem:

$$\{\hat{\upsilon}_m(\mathbf{x},t)\}_{m=1}^{M} = \arg\min_{\{\upsilon_m\}_{m=1}^{M}} \left\| \mathbf{d} - \mathcal{F}\left\{ \sum_{m=1}^{M} \upsilon_m(\mathrm{x},t)\,\hat{\phi}_m(f) \right\} \right\|_2^2 + \mathrm{R}(\{\upsilon_m(\mathbf{x},t)\}_{m=1}^{M})$$

$$\text{s.t.} \quad \upsilon_m(\mathrm{x},t) = \sum_{p=1}^{P_m} \theta_p(x)\varphi_p(t) \qquad [3.3]$$

where $\mathbf{x}$, t, f, are the spatial, temporal, and spectral coordinates, $\{\hat{\phi}_m(f)\}_{m=1}^{M}$ is the estimate of spectral subspace obtained from $\mathcal{D}_1$, $\mathcal{F}$ is the encoding operator, $\mathrm{R}(\cdot)$ is a regularization function which included a smoothness penalty in both space and time, and the model orders M and $\{P_m\}_{m=1}^{M}$ were determined from a singular value decomposition (SVD) based analysis of the data. The final reconstructed image was then computed as $\rho(\mathbf{x},t,f) = \sum_{m=1}^{M} \hat{\upsilon}_m(\mathrm{x},t)\,\hat{\phi}_m(f)$.

3.2.4. In vivo MRI Experiments

The animal protocol was approved by the Institutional Animal Care and Use Committee of the Case Western Reserve University. A Fischer rat was anesthetized with isoflurane (1.5–2.5%) and placed in a cradle in the lateral position. Respiration rate and body temperature were monitored during the experiments. The body temperature was maintained at 35.5 ± 0.5°C by blowing hot air into the MRI scanner through a feedback control system. An inflatable cuff was placed around the thigh of the rat. Ischemia was induced by occluding the femoral artery with the inflated cuff. The experiment was conducted on a 9.4T Bruker Biospec horizontal scanner (Bruker Biospin Inc., Billerica, MA). A Bruker ^{1}H volume coil was used for ^{1}H image acquisition. A custom-built ^{31}P saddle coil was placed around the calf muscles to acquire MRSI data. The leg was secured to the ^{31}P coil that was attached to the cradle to avoid potential motion during the experiment. To minimize the

coupling between the ^{1}H and the ^{31}P coils, the orientation of the two coils were adjusted such that their B_1 fields were perpendicular to each other.

Scout ^{1}H images were acquired to determine the position of the lower leg. Automatic, localized shimming was performed on an isotropic voxel of 15×15×15 mm^3 that covered the entire lower leg using a PRESS sequence. Anatomical ^{1}H images were acquired using FLASH sequence with the following parameters: TR/TE, 500/10 ms; flip angle, 30°; FOV, 2.4×2.4 cm^2; matrix size, 128×128; number of averages, 2; slice thickness, 1.67 mm; number of slices, 12; inter-slice gap, 0.

$\mathcal{D}_1$ dataset was acquired at baseline for 8.5 min using an FID-CSI sequence with 160 ms TR, 0.69 ms TE, 17° flip angle, 2.4×2.4×2 cm^3 FOV, 8×8×6 matrix size, 256 readout points, 6000 Hz bandwidth, and 8 signal averages. During 10 min ischemia and 5 min reperfusion, $\mathcal{D}_2$ dataset was acquired using an FID-EPSI sequence with single-shot uniform density stack of spirals readout. TR, TE and FOV were the same as $\mathcal{D}_1$ acquisition. 20 echoes were acquired with 16×16×12 matrix size, 3.96 ms echo-spacing, 111.1 kHz bandwidth, and 16 signal averages. The frame rate of the EPSI acquisition was 30 s/frame. Both temporal and spatial basis were estimated from $\mathcal{D}_2$ dataset. The total experiment time was approximately 23 min.

3.3. Results

Figure 3.2a shows the center five slices of the anatomical reference images of the rat leg. The corresponding PCr maps during ischemia (Figure 3.2b-d) and

reperfusion (Figure 3.2e) shows that PCr pool was significantly reduced during ischemia and rapidly replenished upon reperfusion. Dynamic spectra from two pixels in different muscle groups showed varied kinetics during ischemia-reperfusion (Figure 3.3). These results demonstrate that our method was able to capture both the temporal dynamics and spatial variation of the image while maintaining good spectral quality. The dynamic behavior of the PCr spatiospectral distribution agrees well with previous experiments reported in the literature (54,61,192). Note that the presented animal experiment was designed for proof-of-concept validation of the ^{31}P SPICE method. The SNR can be further improved by using a surface or quadrature ^{31}P coil. The spatial resolution of the experiment can be improved by using a multi-shot variable density spiral trajectory to acquire $\mathcal{D}_2$ dataset.

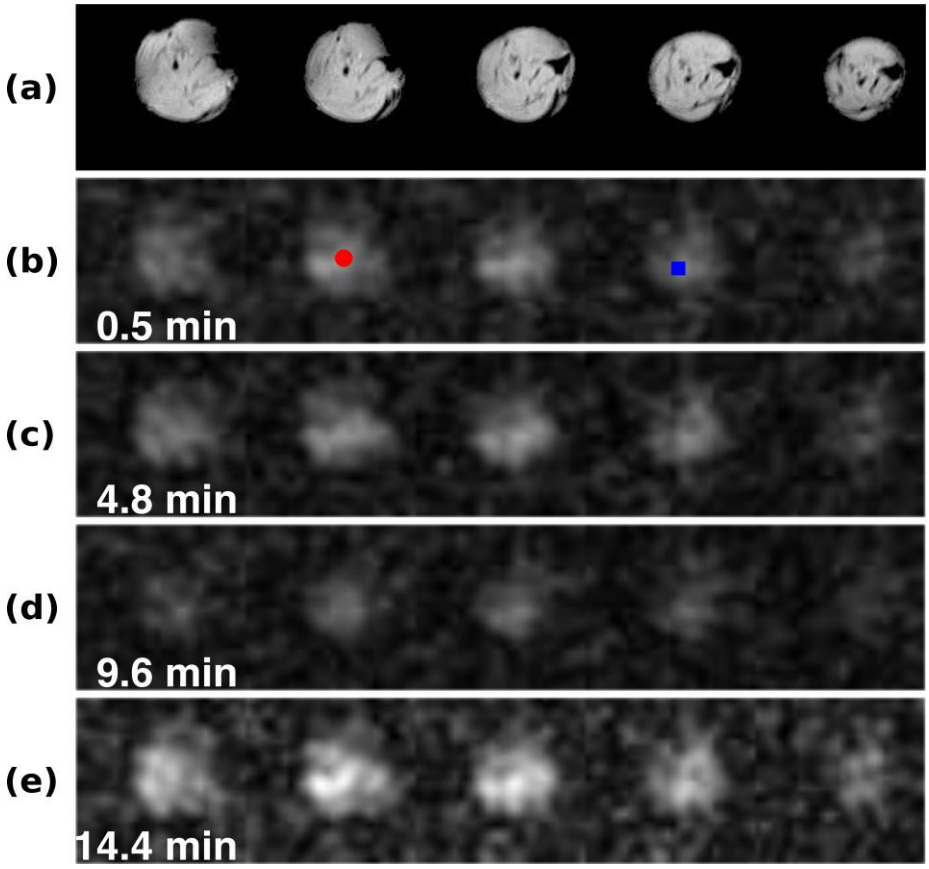

Figure 3.2. Slices of the anatomical reference image **(a)** and PCr peak integral **(b - e)** of the reconstruction at various time points. The pressure cuff was inflated and deflated at approximately 0 and 10 minutes respectively.

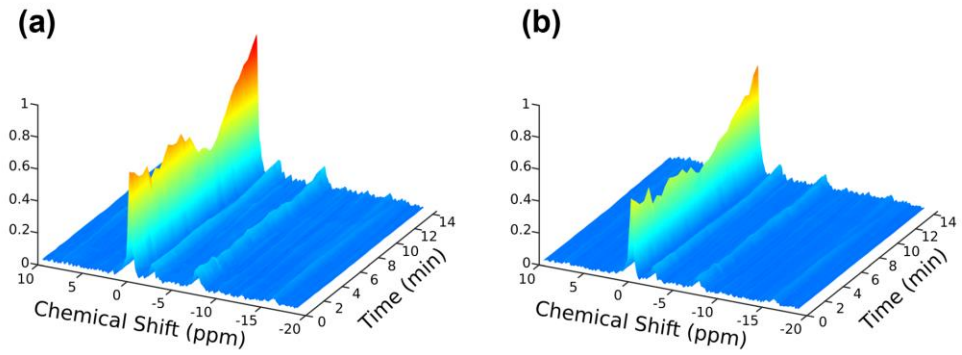

Figure 3.3. Spectra from two different spatial points in the reconstruction shown over time. The locations of the spectra in **(a)** and **(b)** correspond to the locations of the red circle and blue square in Figure 3.2b respectively.

3.4. Discussion and Conclusions

In this study, a recently proposed fast MRSI method (i.e., SPICE) has been adapted and applied to 3D dynamic ^{31}P MRSI for observing the changes in phosphate metabolites in a rat hindlimb with high spatial and temporal resolutions. 15 s nominal temporal resolution and 0.75×0.75×1.6 mm^3 nominal spatial resolution was achieved using the proposed approach. These preliminary results demonstrate the potential of this method to provide an unprecedented combination of SNR, spatial, and temporal resolution for in vivo quantification of PCr depletion and recovery during ischemia-reperfusion. Quantification in a series of phantoms with known concentrations of Pi solutions can be used to further validate the accuracy of the proposed method compared with non-localized MRS or SVS methods in future studies.

Compared with conventional MRSI methods, the proposed method significantly improves SNR efficiency by exploiting the correlations between multiple dimensions in MRSI data (139,209). The SNR benefit of this method comes from 1): the spectral and temporal basis functions are estimated from the "training" data set, which sample central k-space and the acquired data has good SNR; 2): after the estimations of spectral and temporal basis functions, the spatial function and coefficients are determined by solving an optimization problem from the "imaging" data. The reduced number of degrees of freedom of the imaging function makes it possible to recover spatial information from noisy "imaging" data and obtain good SNR. In the current study, SNR can be further improved by

employing more flexible data acquisition schemes, such as variable density spirals, and using more sensitive surface coil or quadrature volume coil.

During image reconstruction, it is critical to select the rank of the model. In principle, the rank depends on the number of metabolites (i.e., PCr, λ-, α-, β-ATP, Pi), tissue types, and dynamic process. In practice, the rank was determined adaptively by performing SVD on the Casorati matrix formed by the "training" data and thresholding the singular values (139).

The current data acquisition approach requires high performance of the gradient system. Given a much lower gyromagnetic ratio of ^{31}P compared with proton, a much higher gradient strength is required in order to achieve high spatial resolution with the same acquisition bandwidth. In the current study, since no echo shifting was employed, the duration of the uniform density spiral readout was designed to be minimum for the benefit of spectral encoding. However, this design demands high gradient amplitude and slew rate, and continuous acquisition with relatively high duty cycle leads to a gradient heating problem during the dynamic experiment. In order to solve this heating problem, more flexible trajectory design for spatiospectral encoding, such as variable density spiral, can be employed. On the other hand, an electrical stimulation protocol can be used to reduce the duration of the PCr depletion period, which achieves the same level of PCr depletion as in ischemia (55,61,63).

In conclusion, the current study demonstrated a fast dynamic ^{31}P MRSI approach. By exploiting the multi-dimensional correlations of the MRSI data, this method proposed a hybrid data acquisition scheme and image reconstruction which

leads to high spatial/temporal resolution and SNR. The feasibility of the proposed method was demonstrated on rat skeletal muscle undergoing an ischemia-reperfusion procedure. Combined with appropriate quantification techniques, this method may allow the assessment of the heterogeneity in mitochondrial oxidative capacity in rodent models of various metabolic diseases.

Chapter 4. Development of Dynamic ^{17}O MRI Using Golden-ratio–based Radial Sampling and k-space–weighted Image Reconstruction

This chapter describes a study that aimed to develop a 3D dynamic ^{17}O MRI method with high temporal and spatial resolution for preclinical applications. A 3D imaging method with a stack-of-stars golden-ratio-based radial sampling scheme was employed to acquire ^{17}O signals. A k-space-weighted image contrast (KWIC) reconstruction method was used to improve the temporal resolution while preserving spatial resolution. Simulation studies were performed to validate the method. Evaluation of PSF was performed in phantom experiments. This method has mainly two preclinical applications. The first is to delineate the kinetics of ^{17}O-water uptake and washout in the brain of small animals after a bolus injection of ^{17}O-labeled water. The second is to measure cerebral metabolic rate of oxygen in small animals with a brief inhalation of ^{17}O-labeled gas. In vivo experiments of these two applications will be described in Chapter 5.

4.1. Introduction

Oxygen is one of the most crucial elements that maintain normal physiological activities in aerobic living organisms. Moreover, various oxygen containing molecules, such as water, play an important role in supporting numerous forms of life on earth. In vivo ^{17}O MRI has been reported to measure the uptake and washout of ^{17}O-labled exogenous agent, such as ^{17}O-labeled water, for evaluating tissue perfusion since 1990s (145–147). More importantly, metabolic

rate of oxygen can be quantified using in vivo ^{17}O MRI non-invasively (154,155,161,162,164,212,213). The most valuable and unique capability of ^{17}O MRI is its potential role in detecting abnormal oxidative metabolism in brain function associated with neurological diseases and thereby assisting diagnosis and treatment evaluation.

There are two available MR methods for detecting $H_2{}^{17}O$ in vivo: direct method (^{17}O MRI) and indirect method (^{1}H MRI). Direct approaches refer to ^{17}O MRI methods that measure ^{17}O signals directly in the brain tissue. These approaches are able to quantify the concentration of $H_2{}^{17}O$ accurately, but usually yield low spatial/temporal resolution due to low signal sensitivity (136–138,141–144,148–153,199–200). Alternatively, the proton signal can be detected to reflect the concentration of $H_2{}^{17}O$ because ^{17}O affects the relaxation times of protons (150). The indirect methods has the advantage of relatively high sensitivity and SNR by measuring the proton signal. However, the changes in the relaxation times of the proton signal induced by ^{17}O are subtle and the quantification is not very reliable or robust in different physiological environments and at different pH levels (216,217).

In addition to MRI, the other available imaging modality capable of detecting water labeled with oxygen isotopes is ^{15}O PET. ^{15}O PET has been established to assess cerebral blood flow and $CMRO_2$ since 1980s (218–221). However, ^{15}O PET requires an on-site cyclotron to generate the short-lived ^{15}O isotope (~2 min half-life), limiting its clinical use. In contrast, ^{17}O is a non-radioactive and MR-detectable isotope and serves as a tracer for assessment of

water movement and oxygen metabolism. Compared with ^{15}O PET, the model used in ^{17}O MRI to calculate $CMRO_2$ is significantly simplified without the compounding signals from $^{17}O_2$ because $^{17}O_2$ is invisible to MR (150). However, SNR of ^{17}O MRI is extremely limited due to its low natural abundance (0.037%) and low MR sensitivity. In addition, assessing water movement and imaging $CMRO_2$ are more challenging in small animals due to the demand of high spatial resolution and temporal resolution compared with humans. High field strength is often used to improve SNR (150,151,156,163). However, even on high-field scanners, images are typically acquired with a large voxel size to achieve adequate SNR.

Current ^{17}O MRI methods for imaging $H_2{}^{17}O$ directly in clinical and preclinical studies include mainly two approaches. Both approaches use ultra-short echo time sequences because minimizing signal loss in ^{17}O MRI is critical due to the extremely short transverse relaxation time of ^{17}O (215). One approach is a ^{17}O 3D MRSI approach using the 3D Fourier Series Window MRS imaging technique (154,158); the other is non-Cartesian encoding 3D imaging sequences, such as the flexTPI acquisition and density-adapted 3D radial sequence (159,160).

The aim of this study was to develop a 3D dynamic ^{17}O MRI method with high temporal and spatial resolutions that allows for characterizing the kinetics of $H_2{}^{17}O$ uptake and washout in the brain of small animals, as well as quantifying $CMRO_2$ in small animal models. A stack-of-stars radial sampling method was implemented based on the golden-angle acquisition scheme (222). KWIC reconstruction was applied to the acquired data to improve the temporal rate with

preserved spatial resolution (223). Simulation studies were performed to validate the method. Feasibility of implementing 3D stack-of-stars radial acquisition based on golden-ratio profile order on the preclinical scanner was demonstrated on phantoms. Evaluation of the PSF was also performed in phantom experiments.

4.2. Methods

4.2.1. Golden-Ratio-Based Radial Sampling and k-Space-Weighted Image Reconstruction

Since changes in image intensity are determined primarily by the low-frequency data in dynamic imaging, undersampled radial images still retain abundant dynamic information due to the intrinsic oversampling of the center k-space by the radial trajectory. The golden-ratio-based radial profile order was proposed and adopted by various dynamic MRI studies that demanded high temporal and spatial resolutions (222,224,225). Instead of sampling the k-space with evenly spaced radial lines in the order of increasing azimuthal angles from 0 to π (or 2π), a golden-ratio-based profile uses an azimuthal angle spacing of π (or 2π) divided by the golden ratio. This sampling scheme achieves a nearly uniform coverage of k-space with an arbitrary number of spokes, and k-space coverage becomes most uniform when the number of spokes reaches a Fibonacci number (222). Therefore, the golden-ratio-based profile order is extremely flexible, enabling various undersampling schemes and retrospective selection of an image update rate/temporal resolution for dynamic imaging.

In the current study, a dynamic golden-angle acquisition was combined with KWIC reconstruction to achieve high temporal resolution with preserved spatial resolution (223). To reconstruct a specific time frame, the k-space was segmented into a set of rings (Figure 4.1). The central ring consisted of radial spokes acquired at the time frame of interest, with the number of spokes being a Fibonacci number. Moving out in k-space to the next ring, the number of spokes increased to the next Fibonacci number. The radius of each ring was chosen such that the number of spokes in each ring fulfilled the Nyquist sampling criterion (223). For example, the k-space filter used in the simulations for injection studies consisted of five rings

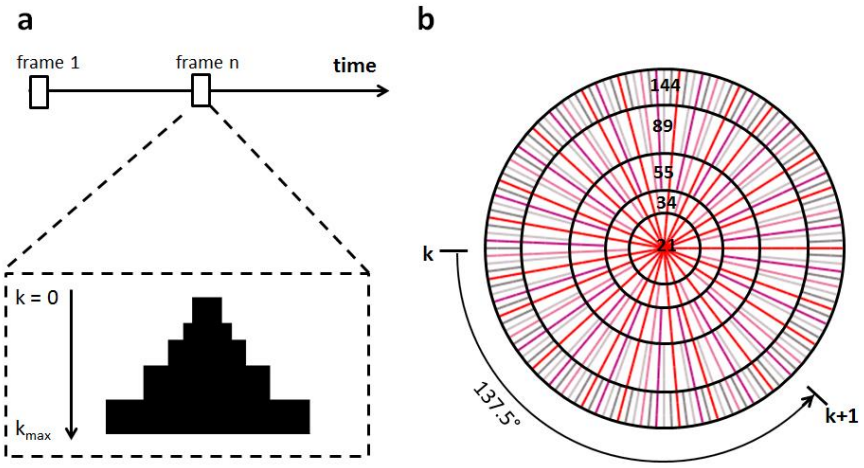

Figure 4.1. Image reconstruction by k-space filtering. **a**: Data selection for a specific time frame. Half of the k-space from center to k_{max} is shown. The k-space filter was shifted by 21 spokes from one time frame to the next. **b**: k-space filtering with golden-ratio-based profile order. The k-space was segmented into 5 rings with 21 spokes in the central ring. The following rings consisted of 34, 55, 89, and 144 spokes, respectively.

with 21, 34, 55, 89, and 144 spokes in each ring respectively, and the outer radius of each ring was 3, 5, 8, 12, and 16 respectively (Figure 4.1b). Hence, the filtered

data comprised of a total of 1228 data points in k-space. After the k-space filtering, all images were reconstructed using the non-uniform fast Fourier transform (NUFFT) toolbox (123). The density compensation function was calculated and applied to the data using the method developed by Pipe et al. (226) prior to regridding.

4.2.2. Simulations

To evaluate the impact of k-space filtering on the dynamics of the ^{17}O signal in both $H_2{}^{17}O$ injection and $^{17}O_2$ inhalation experiments, simulation studies were performed on a modified Shepp-Logan phantom with three compartments, and a brain phantom with two compartments, respectively.

On the one hand, in the modified Shepp-Logan phantom, the time course of ^{17}O signal changes in each compartment comprised of three segments representing the three phases of an $H_2{}^{17}O$ injection experiment: the baseline with a constant ^{17}O signal, the injection phase with a rapid linear increase, and the washout phase with a mono-exponential decay. The duration of baseline, injection, and washout phases was 3, 0.5, and 18 min, respectively. The baseline-normalized peak and steady-state ^{17}O signal and the washout rate used in simulation are listed in Table 1. These values were representative of those observed in the mouse brain in vivo. Using these values, a set of dynamic images was generated with a matrix size of 256×256 and a temporal resolution of 0.36 s. Temporal resolution here is defined as the time lapse between the acquisitions of two consecutive spokes in a slice. A total of 3583 images were generated to simulate the entire course of signal changes at baseline, during $H_2{}^{17}O$ injection, and during the washout phase.

On the other hand, in the two-compartment brain phantom, the two compartments were designed to present normal and compromised $CMRO_2$ during $^{17}O_2$ inhalation studies, corresponding to normal brain tissue and stroke area, respectively. The ^{17}O signal increase was 60% and 25% in the left (normal) and right (stroke) compartment, respectively, during a 2 min inhalation period. These values were designed based on our initial experience in $^{17}O_2$ inhalation experiments and those reported in the literature (156,161). Using these values, a set of dynamic images was generated with a matrix size of 256×256 and a temporal resolution of 1.08 s. A total of 1221 images were generated containing 5 min baseline, 2 min inhalation and 15 min washout phase.

The center one eighth of k-space for the simulated dynamic images was used to reconstruct dynamic images with a matrix size of 32×32. In the injection simulation studies, two experimentally relevant noise levels, corresponding to an SNR of 10 and 20 at baseline, were evaluated by adding random noise to each spoke of the entire dataset. Dynamic images were reconstructed using the k-space filter shown in Figure 4.1. The k-space filter was shifted by 21 spokes from one time frame to the next. Peak and steady-state ^{17}O signal maps, as well as the map of washout rate, were generated by pixel-wise fitting of the signal during the washout phase to a mono-exponential function. Normalized root mean square error (NRMSE) of the reconstructed maps was calculated against the corresponding noiseless and fully sampled maps. On the other hand, SNR of ~30 at baseline was evaluated in the inhalation simulation study. The k-space filter used for image reconstruction contains 6 rings with 13, 21, 34, 55, 89, 144 spokes in each ring. It

was shifted by 13 spokes from one time frame to the next to reconstruct dynamic images. The map of signal change rate was generated by pixel-wise fitting of the signal during the inhalation phase to a linear function. According to the simplified model to calculate $CMRO_2$, multiplication of this rate map and a constant gives rise to $CMRO_2$ map (156).

4.2.3. Phantom Experiments

The PSF of the proposed acquisition and reconstruction scheme was measured using a point source phantom. A micro-hematocrit capillary tube with an inner diameter of 1 mm was filled with $H_2{}^{17}O$ (21% enrichment) and placed under an ^{17}O surface coil parallel to the z-direction of the magnet. 3D ^{17}O images perpendicular to the z-direction were acquired. The PSF from three approaches was compared: 1) conventional 3D stack-of-stars radial sampling with 100 evenly distributed spokes to fully sample the k-space; 2) 3D stack-of-stars radial sampling using the golden-ratio-based profile order with 100 spokes; 3) 3D stack-of-stars radial sampling using the golden-ratio-based profile order combined with the KWIC reconstruction. Other acquisition parameters were the same for all three sampling schemes: TR/TE, 9/0.304 ms; FOV, 4.8×4.8×1.25 cm^3; matrix size, 32×32×5; number of averages, 16. These parameters gave rise to a nominal voxel size of ~5.6 μL, which is the target voxel size for in vivo $H_2{}^{17}O$ injection studies in the mouse brain. The full width of half maximum (FWHM) of the PSF was measured to compare the spatial profile of the three approaches.

4.2.4. Image Reconstruction and Analysis

Image reconstruction and analysis used in-house developed software written in MATLAB (Mathworks, Natick, MA, USA). The k-space filter was shifted by 21 and 13 spokes from one time frame to the next in simulations for injection and inhalation studies, respectively. This design will achieve a relatively satisfactory balance between SNR, spatial resolution, and temporal resolution in the mouse brain for future in vivo studies based on our previous experience of in vivo SNR. No zero padding was performed in simulation studies. For phantom experiments, each slice was zero-padded to a matrix size of 128×128 and Fourier transformed to yield 3D images.

Peak $H_2{}^{17}O$ uptake was identified as the maximal signal intensity following $H_2{}^{17}O$ injection. The time course of the ^{17}O signal from peak uptake to the end of the measurement was fit to a mono-exponential function in a pixel-wise fashion to generate the maps of peak and steady-state $H_2{}^{17}O$ uptake, as well as its washout rate. ROIs were drawn manually for the three compartments in the digital phantom. Mean values for each ROI were calculated for each map.

4.3. Results

4.3.1. Simulations for Injection Studies

Figure 4.2 shows the effects of the k-space filter on the estimation of the peak and steady-state ^{17}O signal and the washout rate at two different noise levels.

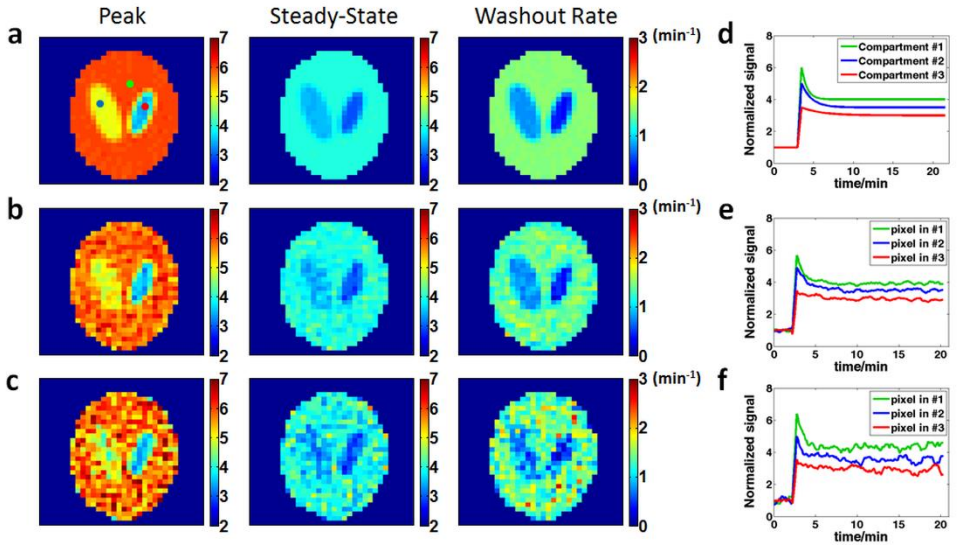

Figure 4.2. Simulation results at two different noise levels. **a**: Maps of peak and steady-state $H_2{}^{17}O$ uptake and washout rate generated from noiseless data. **b:** Data with a baseline SNR of 20. **c:** Data with a baseline SNR of 10. **d**: Simulated, noise-free time courses of the signal changes in the three compartments. **e-f**: Time courses of the representative pixels in each of the three compartments with a baseline SNR of 20 (**e**) and 10 (**f**). The selected pixels are indicated by colored dots in (**a**).

The mean values in the three compartments are summarized in Table 1. With an SNR of 20 at baseline, the NRMSE of the peak uptake and steady-state ^{17}O signal and the washout rate was 1.36%, 1.52%, and 4.01%, respectively. A decrease in SNR led to a corresponding increase in the NRMSE to 1.8%, 2.19%, and 5.34% for the same measurements. Consistent with the increase in NRMSE, the estimated parameters also showed larger variations at lower SNR. However, mean values of the estimated parameters showed unbiased estimation at different noise levels.

These results suggest that the KWIC reconstruction method combined with the golden-ratio-based radial sampling is capable of delineating the dynamics of ^{17}O signal even with relatively low SNR.

Table 4.1. Simulation results. Summary of peak and steady-state $H_2{}^{17}O$ uptake, and washout rate in designed phantom, noiseless and fully sampled maps, and reconstructed maps at different noise levels.

	Compartment	Peak ^{17}O Signal	Steady-State ^{17}O Signal	Washout Rate (min^{-1})
Chosen Values	#1	6	4	1.5
	#2	5	3.5	0.8
	#3	3.5	3	0.4
Noiseless	#1	6 ± 0.02	4 ± 0.01	1.5 ± 0.01
	#2	4.99 ± 0.03	3.5 ± 0.01	0.79 ± 0.02
	#3	3.45 ± 0.04	2.98 ± 0.01	0.38 ± 0.02
SNR = 20	#1	5.86 ± 0.2	3.97 ± 0.16	1.51 ± 0.13
	#2	4.98 ± 0.19	3.47 ± 0.13	0.81 ± 0.06
	#3	3.57 ± 0.11	3 ± 0.04	0.42 ± 0.07
SNR = 10	#1	5.86 ± 0.35	3.98 ± 0.3	1.48 ± 0.33
	#2	4.94 ± 0.45	3.46 ± 0.36	0.83 ± 0.3
	#3	3.59 ± 0.16	2.96 ± 0.18	0.38 ± 0.24

4.3.2. Simulations for Inhalation Studies

Figure 4.3 shows the effects of the k-space filter on the estimation of the ^{17}O signal increase rate during inhalation with an SNR of 30 at baseline. The averaged signal increase rate was 0.30 ± 0.06 min^{-1} and 0.14 ± 0.07 min^{-1} in the left and right compartment, respectively, compared with the ground truth of 0.3 min^{-1} and 0.125 min^{-1}. Simulations at lower SNR levels were attempted. With an SNR of 20 at baseline, the averaged signal increase rate were 0.30 ± 0.10 min^{-1} and 0.14 ± 0.09 min^{-1} in the left and right compartment, respectively. The estimated parameters showed larger variations at lower SNR as expected, and pixel-wise curve fitting in the left compartment with 60% signal increase is still robust. However, unrobust curve fitting results in some pixels in the right compartment which has only 25%

signal increase were observed due to the dominant noise when SNR at baseline dropped below 20.

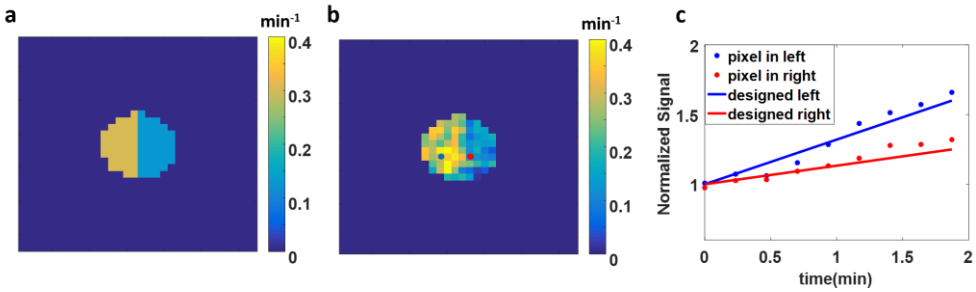

Figure 4.3. Results of simulation for inhalation studies. **a**: Designed rate map of the two compartment phantom. **b:** Reconstructed rate map with a baseline SNR of 30. **c:** Time courses of the representative pixels in the two compartments are shown in blue dots (left compartment) and red dots (right compartment). The selected pixels are indicated by colored dots in (**b**). Time courses of the designed noise-free signals in the two compartments are shown in solid lines.

4.3.3. Phantom Experiments

The measured PSF using a point source phantom is shown in Figure 4.4. Comparing to the conventional radial sampling scheme with full k-space coverage, the area of PSF at FWHM was 10% larger using the golden-ratio-based sampling with and without KWIC reconstruction (4.5 mm^2 vs. 4.1 mm^2), suggesting that the difference in PSF was caused by the golden-ratio-based sampling rather than KWIC reconstruction. Based on the measured PSF, the true voxel size using the golden-ratio-based sampling with KWIC reconstruction was approximately 11.25 μL (4.5 mm^2 in-plane and 2.5 mm in the phase encoding direction). However, it should be noted that this true voxel size of 11.25 μL measured from phantom is an overestimation due to other factors contributing to PSF, such as B_0 field inhomogeneity during the experiment, the size of the phantom, etc.

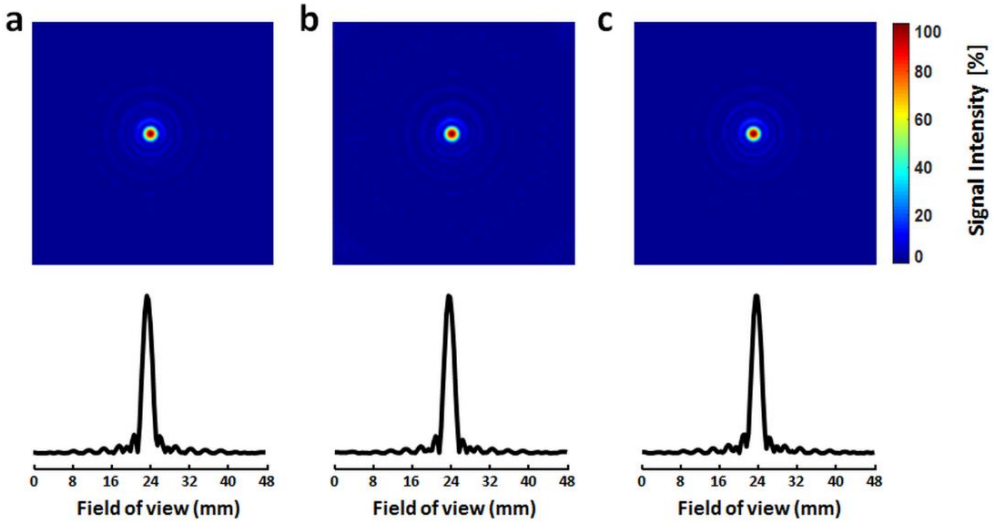

Figure 4.4. Point spread function (PSF) measured from a point source phantom. a: Conventional radial sampling with 100 spokes. b: Golden-ratio-based radial sampling with 100 spokes. c: Golden-ratio-based radial sampling combined with the k-space filtering. Top: 2D maps. Bottom: 1D profiles.

4.4. Discussion and Conclusions

In the current study, a dynamic ^{17}O imaging method with a golden-ratio-based radial sampling profile and KWIC reconstruction was developed and validated in simulation studies. PSF was also evaluated in phantom experiments.

KWIC reconstruction was first proposed by Song et al to manipulate T_2-weighted image contrast from a single image dataset (223). The application of the KWIC reconstruction method in dynamic imaging is facilitated by combining it with a golden-ratio-based radial sampling profile (222,227). An advantage of the golden-angle sampling and KWIC reconstruction is the flexibility to retrospectively choose the temporal rate for the reconstructed images. Golden-ratio-based radial sampling enables quick updates of the center k-space so that no *a priori* knowledge

of the expected kinetics is needed at the stage of data acquisition. A specific k-space filter can be chosen in post-processing for optimal data reconstruction. In principle, any k-space filter that satisfies the Nyquist criterion can be used. With a golden-ratio-based sampling profile, both SNR and k-space coverage are optimal when the number of spokes is a Fibonacci number (222). Hence, a k-space filter designed using Fibonacci numbers allows for satisfaction of the Nyquist criterion with the minimal number of spokes and is optimal for dynamic studies that require high temporal resolution. There is sufficient flexibility in choosing the number of spokes for a specific temporal resolution since the difference between two adjacent Fibonacci numbers increases gradually. In the current study, a k-space filter with 21 spokes and 13 spokes in the central ring was used in simulations for injection and inhalation studies, respectively. An alternative filter with fewer spokes in the central ring can also be used if a higher temporal resolution is more desirable.

The flexibility of choosing a k-space filter to achieve adequate temporal resolution allows application of this method in both $H_2{}^{17}O$ injection and $^{17}O_2$ inhalation studies in vivo. Even though both injection and inhalation studies can use the same ^{17}O MRI approach, there exist significant differences between these two dynamic processes that should be considered for the optimization of acquisition and reconstruction parameters. The increase in $H_2{}^{17}O$ signal is rapid during a bolus injection of $H_2{}^{17}O$, which requires high temporal resolution to capture the kinetics of water uptake. In contrast, the rate of ^{17}O signal increase during an inhalation study is significantly slower but SNR at peak and steady-state is much lower than that in an injection study due to the small amount of $^{17}O_2$ inhaled. Therefore, more

signal averages or larger voxel size are usually needed in an inhalation study compared to an injection study. The sampling temporal resolution and reconstructed apparent temporal resolution in the current simulation studies were designed according to the estimated repetition time and signal averages for future in vivo studies based our previous experience on SNR in the mouse brain in vivo. More detailed comparison between injection and inhalation studies and thereby the choice of acquisition/reconstruction parameters will be discussed in Chapter 5.

One important difference between ^{17}O signal acquisition and ^{1}H signal acquisition should be noted that multiple signal averages are necessary to compensate for low SNR in ^{17}O signal acquisition as compared with a single average used in most ^{1}H MRI studies. In the current simulation studies, each spoke represents the spoke after multiple signal averages in an in vivo experiment. In other words, the current acquisition scheme is that signal average of a single spoke is performed before the next spoke is acquired. Alternatively, spokes following the golden-ratio based profile order can be acquired continuously with one average of each spoke. Additional simulation studies were performed in the two-compartment phantom to compare these two strategies. For the single-average strategy, the k-space filter was segmented into six rings with the same radius as in the multiple-average strategy for the inhalation simulations. A signal average of 8 was assumed, leading to a sampling temporal resolution of 135 ms instead of 1.08 s as in the multiple-average approach. For the multiple-average strategy, 8 acquisitions of the same spoke was added, then the averaged spokes were used to reconstruct dynamic images using KWIC method. For the single-average strategy, 8 times of number of

points were used to reconstruct each time frame as compared to the multiple-average strategy to achieve a fair comparison from the SNR perspective and to maintain the reconstructed temporal resolution the same for both approaches. With an SNR of ~25 at baseline, signal increase rate during inhalation was 0.29 ± 0.07 min^{-1} (left compartment) and 0.14 ± 0.07 min^{-1} (right compartment) using multiple-average approach and 0.28 ± 0.06 min^{-1} (left compartment) and 0.15 ± 0.07 min^{-1} (right compartment) using single-average approach. With an SNR of ~50 at baseline, multiple-average approach yielded signal increase rate of 0.31 ± 0.04 min^{-1} in the left compartment and 0.14 ± 0.04 min^{-1} in the right compartment; single-average approach gave rise to signal increase rate of 0.29 ± 0.04 min^{-1} and 0.14 ± 0.04 min^{-1} in the left and right compartment, respectively. Since no significant difference was observed using these two approaches, the multiple-average approach will be used in in vivo studies for convenience in sequence implementation and data storage.

In conclusion, this study demonstrated a promising dynamic ^{17}O MRI approach for mouse imaging with high spatial and temporal resolution. It provides a robust and flexible imaging approach to study water movement and oxygen metabolism in brain under normal and diseased conditions.

Chapter 5. In vivo Applications of Dynamic ^{17}O MRI: Assessment of Water Movement across BBB in a Mouse Model of GBM and Cerebral Oxygen Metabolism in a Mouse Model of MCAO

This chapter describes the studies that aimed to exploit the feasibility of the 3D golden-angle radial ^{17}O MRI method combined with KWIC reconstruction for in vivo applications. Using this method, the kinetics of $H_2{}^{17}O$ uptake and washout in the brains of mice with GBM was delineated after an intravenous bolus injection of ^{17}O-labeled water. Furthermore, $CMRO_2$ in a mouse model of MCAO was assessed with a brief inhalation of ^{17}O-labeled gas.

For the ^{17}O-labeled water injection study in GBM mice, the proposed ^{17}O imaging method achieved a nominal temporal resolution of 7.56 s with a nominal voxel size of 5.625 μL in the mouse brain at 9.4T. Reduced uptake and prolonged washout of $H_2{}^{17}O$ were observed in tumor tissue, suggesting compromised cerebral perfusion. For the $^{17}O_2$ inhalation study in MCAO mice, this method achieved a nominal temporal resolution of 14.04 s with a nominal voxel size of 10 μL at 9.4T. Deficits in $CMRO_2$ was detected by ^{17}O MRI before edema was observed in T_2-weighted ^{1}H images, suggesting ^{17}O MRI is a powerful tool for diagnosis at the early stage of stroke, and may potentially provide a promising tool to facilitate the assessment of ischemic penumbra in stroke patients.

5.1. Introduction

Regulation of cerebral fluids plays a vital role in brain function (228). Investigation of cerebral fluid dynamics, such as blood flow, diffusion, and water movement across BBB, is of great value in assessing brain physiology and function under normal and diseased conditions. While MRI with arterial spin labeling (ASL) uses magnetically labeled endogenous water as a tracer to measure CBF (229), other imaging methods have used isotope-labeled exogenous water tracers to quantify both CBF and water transport across the BBB (230,231). Using water labeled with oxygen isotopes, ^{17}O MRI is an available method capable of tracing water movement in vivo. Water dynamics and CBF can be assessed with ^{17}O MRI by observing the kinetics of $H_2{}^{17}O$ signal either from a bolus injection of $H_2{}^{17}O$ or from metabolically produced $H_2{}^{17}O$ from inhaled ^{17}O-labeled gas (154,156,164).

On the other hand, oxygen is essential for oxidative phosphorylation in mitochondria to produce energy to maintain physiological activities in the cell. ~20% of oxygen used in the body is consumed by the brain in spite of its relatively small size. Abnormalities in cerebral oxygen metabolism are implicated in many diseases, such as stroke and tumor. Therefore, direct assessment and quantification of cerebral oxygen metabolism plays an important role in disease diagnosis and treatment evaluation. In acute stroke particularly, assessment of metabolic state of the ischemic tissue may help to identify the tissue at the risk of infarction and provide appropriate reperfusion strategies for patients. ^{17}O MRI has been used extensively to evaluate cerebral metabolic activity in rats (161), healthy cats (162), and mice (156,163). Quantification of $CMRO_2$ was accomplished by calculating

the rate of $H_2{}^{17}O$ generation from inhaled $^{17}O_2$. With inhalation of $^{17}O_2$, the labeled oxygen molecules are metabolized in the mitochondria of brain cells to produce $H_2{}^{17}O$, which can be detected by ^{17}O MRI directly. Hence, $CMRO_2$ can be derived from the rate of metabolic $H_2{}^{17}O$ accumulation in the brain.

This study aimed to exploit the feasibility of the 3D golden-ratio-based stack-of-stars acquisition approach combined with KWIC reconstruction method as described in Chapter 4 for in vivo applications. In particular, this method was applied to both $H_2{}^{17}O$ injection and $^{17}O_2$ inhalation studies in mouse models. Using this method, the kinetics of $H_2{}^{17}O$ uptake and washout in the brains of mice with GBM were delineated after an intravenous bolus injection of $H_2{}^{17}O$. Furthermore, $CMRO_2$ in a mouse model of MCAO was assessed with a brief inhalation of $^{17}O_2$.

5.2. Methods

5.2.1. GBM Animal Model

All animal procedures were conducted in accordance with the protocol approved by the Institutional Animal Care and Use Committee of Case Western Reserve University. 6-8 week old athymic NCR nu/nu male mice (Case Western Reserve University Athymic Animal & Xenograft Research Core) were anesthetized via injection of a freshly prepared mixture of ketamine and xylazine and then placed in a stereotaxic frame equipped with a QSI Ultra pump (Stoelting Co., IL, USA). A 33-guage microinjection syringe (Hamilton Co., NV, USA) was preloaded with ~20,000 primary human GBM L2 cancer stem cells in 1 μL and the cells were injected through a 0.7-mm hole in the scalp of the mouse, at a rate of

0.25 μL/min at the following stereotaxic coordinates: anterior to bregma, 0.5 mm; lateral to midline, 1.8 mm; ventral to dura, 2.5 mm with the bregma set at zero. For the control mice, 1 μL of saline was injected into the same location. The microsyringe remained in place for additional 3 min before being slowly removed. The incision was closed with sutures and the sutures were removed 5 days after the injection.

5.2.2. Stroke Animal Model

45-min left MCAO was performed on a male C57BL/6 mouse to induce ischemic stroke. The mouse was placed on a heating pad and MRI studies were conducted 2 hours after MCAO. All animal procedures were conducted in accordance with the protocol approved by the Institutional Animal Care and Use Committee of Case Western Reserve University.

5.2.3. In Vivo MRI Experiments in GBM Mice

MRI studies were performed on a horizontal Biospec 9.4T scanner (Bruker Inc., Billerica, MA, USA). The mouse was initially anesthetized with 3% isoflurane mixed with 100% oxygen while anesthesia was maintained with 0.5 to 1% isoflurane mixed with 100% oxygen. A 29G catheter was inserted into the tail vein for the injection of 200 μL of ^{17}O-water (13% enrichment) in 20 to 25 s. The mouse was then placed in the cradle in a prone position and the respiration rate and body temperature were monitored during the experiments. The body temperature was maintained at 35°C by blowing warm air into the scanner through a feedback control system (SA Instruments, Stony Brook, NY, USA).

^{1}H images were acquired using a 3-cm birdcage coil (Bruker Inc., Billerica, MA, USA) with a 2.5-cm diameter ^{17}O surface coil built in-house placed on top of the mouse head for ^{17}O image acquisition. Multi-slice, T_2-weighted, axial ^{1}H images were acquired using a RARE sequence with the following parameters: TR, 2 s; effective TE, 48 ms; echo spacing, 16 ms; echo train length, 8; FOV, 2.4×2.4 cm^2; slice thickness, 1 mm; matrix size, 256×256; number of averages, 16; number of slices, 5; inter-slice gap, 1.5 mm.

^{17}O images were acquired using a 3D stack-of-stars short echo-time sequence. A total of five radially encoded stacks of data were collected to cover the cylindrical 3D k-space. A 90° RF pulse of 120-μs duration was used for excitation, followed by a 110-μs phase-encoding gradient to achieve short echo time. Radial sampling of the k-space used a constant azimuthal angle spacing of 137.5°, the equivalent of 360° divided by the golden ratio (222,232). Each spoke sampled 16 data points starting from the center of k-space and reached a maximum k value (k_{max}) of 0.33 mm^{-1} with a receiver bandwidth of 8000 Hz. No spoiler gradient was used because of the short T_2 of the ^{17}O signal. Seven fully sampled datasets (100 spokes/slice) were acquired before $H_2{}^{17}O$ injection and data acquisition continued for another ~22 min after the injection. A total of 21600 spokes in 3D k-space were acquired continuously. Other imaging parameters were: TR/TE, 9/0.367 ms; FOV, 4.8×4.8×1.25 cm^3; matrix size, 32×32×5; number of averages, 8. These parameters gave rise to a nominal voxel size of 5.625 μL.

5.2.4. In Vivo MRI Experiments in the Stroke Mouse

MRI studies were performed on a horizontal Biospec 9.4T scanner (Bruker Inc., Billerica, MA, USA). The mouse was initially anesthetized with 2% isoflurane mixed with 100% oxygen. Then the anesthesia was maintained with 0.5 to 1% isoflurane mixed with 20% oxygen and 80% nitrogen. The mouse was placed in the cradle in a prone position and the respiration rate and body temperature were monitored during the experiments. The body temperature was maintained at 36°C by blowing warm air into the scanner through a feedback control system (SA Instruments, Stony Brook, NY, USA). Two sets of ^{1}H images were acquired at 2 hours and 4 hours after MCAO to trace the development of edema. The ^{17}O MRI experiment was performed at 2 hours after MCAO immediately after the first ^{1}H scan. The timeline of the experiment is shown in Figure 5.1.

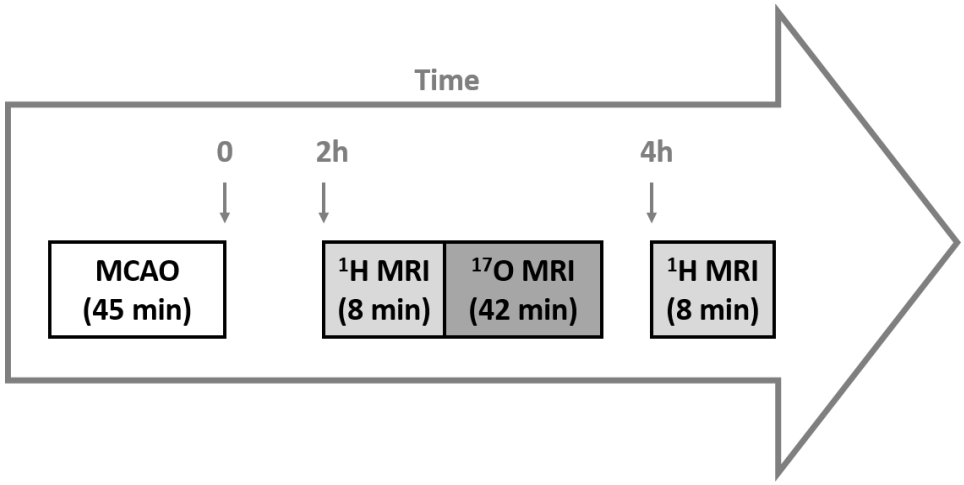

Figure 5.1. Timeline of the MRI experiments. ^{1}H MRI was performed at 2 hours after MCAO. ^{17}O MRI was conducted immediately after the ^{1}H scan. The total 42 min ^{17}O MRI scan consisted of 13 min baseline, 3 min 45 s $^{17}O_2$ inhalation, and 25 min washout phase. ^{1}H MRI was performed again at 4 hours after MCAO to evaluate the development of edema.

A 3-cm birdcage coil (Bruker Inc., Billerica, MA, USA) and a 2-cm diameter in-house built ^{17}O surface coil placed on top of the mouse head were used to acquire ^{1}H and ^{17}O images, respectively. Multi-slice, T_2-weighted, axial ^{1}H images were acquired at 2 hours and 4 hours after MCAO using a RARE sequence. The acquisition time is 8 min and the imaging parameters are: TR, 2 s; effective TE, 48 ms; echo spacing, 16 ms; echo train length, 8; FOV, 3.2×3.2 cm^2; slice thickness, 1 mm; matrix size, 256×256; number of averages, 16; number of slices, 13; inter-slice gap, 0.

^{17}O images were acquired using a 3D stack-of-stars short echo-time sequence. A 90° RF pulse of 50-μs duration was used for excitation, followed by a 110-μs phase-encoding gradient to achieve short echo time. The radial spokes sampled 16 data points from center k-space to maximum k-space with a receiver bandwidth of 8000 Hz. No spoiler gradient was used because of the short T_2 of the ^{17}O signal. A constant azimuthal angle spacing of 137.5°, the equivalent of 360° divided by the golden ratio (222,232), was used to rotate the radial spokes. The continuous acquisition of ^{17}O signals consisted of 13 min baseline, 3 min 45 s $^{17}O_2$ inhalation, and 25 min washout phase. 200 mL $^{17}O_2$ (70% enrichment) was delivered to the mouse through the nose cone by switching the gas delivery channel manually during the ^{17}O MRI scan. Other imaging parameters are: TR/TE, 9/0.304 ms; FOV, 6.4×6.4×1.25 cm^3; matrix size, 32×32×5; number of averages, 24. These parameters gave rise to a nominal voxel size of 10 μL.

5.2.5. Image Reconstruction and Analysis

Image reconstruction and analysis used in-house developed software written in MATLAB (Mathworks, Natick, MA, USA). The k-space filters used in in vivo injection and inhalation studies are the same as in injection and inhalation simulation studies described in Chapter 4, respectively. For the $H_2{}^{17}O$ injection study in GBM mice, the k-space filter was shifted by 21 spokes from one time frame to the next, leading to an effective temporal resolution of 7.56 s with 9 ms TR and 8 signal averages. On the other hand, for the $^{17}O_2$ inhalation study in stroke mice, the k-space filter was shifted by 13 spokes from one time frame to the next, leading to an effective temporal resolution of 14.04 s with 9 ms TR and 24 signal averages. After density compensation and regridding, each slice was zero-padded to a matrix size of 64×64 and Fourier transformed to yield 3D images.

For GBM mice, once image reconstruction was completed, ^{17}O images were co-registered with the T_2-weighted ^{1}H images. Tumor areas showed higher signal intensity in T_2-weighted ^{1}H images due to having a longer T_2 than normal brain tissue. Appropriate ROIs that encompassed the tumor and normal brain tissue were drawn manually from T_2-weighted ^{1}H image. Total tumor and brain volumes were calculated by adding the tumor and brain areas in all five slices. The percentage of tumor volume was calculated as the tumor volume divided by total brain volume. Mice with >30% tumor volume were classified as the GBM-Large (GBM-L) group, and mice with <30% tumor volume were designated as the GBM-Moderate (GBM-M) group. Control mice had a single ROI that covered the entire brain. The ^{17}O signal was normalized by the corresponding natural abundance ^{17}O signal acquired

before $H_2{}^{17}O$ injection. Peak $H_2{}^{17}O$ uptake was identified as the maximal signal intensity following $H_2{}^{17}O$ injection. The normalized time course of the ^{17}O signal from peak uptake to the end of the measurement was fit to a mono-exponential function in a pixel-wise fashion to generate the maps of peak and steady-state $H_2{}^{17}O$ uptake, as well as its washout rate. Mean values for each ROI were calculated for each map. In tissue with no obvious washout phase or even continued accumulation of $H_2{}^{17}O$ after the injection, washout rate was set to zero, while peak and steady-state $H_2{}^{17}O$ uptake was calculated as the normalized ^{17}O signals immediately after $H_2{}^{17}O$ injection and at the end of measurement, respectively.

For stroke mice, the $H_2{}^{17}O$ signal was normalized by the corresponding natural abundance ^{17}O signal acquired before $^{17}O_2$ inhalation. $CMRO_2$ map was generated by pixel-wise fitting of the ^{17}O signal during inhalation to a model of tissue metabolism based on the mass-balance of $H_2{}^{17}O$ generation from mitochondrial respiration and its transport as shown in Eq. 1.5 (156).

5.2.6. Histology

After the MRI experiments, all GBM mice were anesthetized with a mixture of ketamine and xylazine and fixed by transcardial perfusion with 4% paraformaldehyde. The brain was then excised and fixed for another 72 hours. The olfactory bulbs, a small portion of the rostral cortex leading up to the tumor injection site, and the cerebellum were trimmed after the fixation. The brains were cryoprotected in 30% sucrose for 48 to 72 hours, followed by 1:1 30% sucrose:O.C.T. Compound (Fisher Scientific, Pittsburg, PA, USA) for another 48 to 72 hours. The tissue was then embedded in O.C.T. Compound, frozen with liquid

nitrogen, and sectioned into 8 μm thick coronal sections that were then stained with hematoxylin and eosin (H&E) staining.

5.2.7. Statistics

All results are reported as mean ± standard deviation and two-way analysis of variance (ANOVA) was used for data comparison. If statistical differences were detected, multiple pairwise comparisons were performed using a two-tailed student's t-test. An unpaired two-tailed student's t-test was used to compare the peak and steady-state uptake and the $H_2{}^{17}O$ washout rate among the three groups of mice. A paired two-tailed student's t-test was used to compare the parameters between tumor and non-tumor tissue in the same group for GBM-L and GBM-M mice. Significant difference was accepted at $p<0.05$.

5.3. Results

5.3.1. In Vivo Results in GBM Mice

A total of 15 mice were scanned in the current study, with 6 in GBM-L group, 4 in GBM-M group, and 5 in the control group. Representative T_2-weighted images and their corresponding histological staining in GBM-L and GBM-M groups are shown in Figure 5.2. The age of the mice at the time of the MRI scans was 37.3 ± 2.5 weeks, 34.6 ± 2.1 weeks, and 11.5

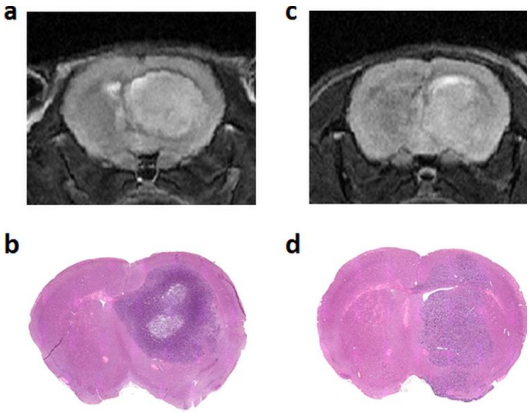

Figure 5.2. Representative T_2-weighted images and their corresponding H&E staining in mice with GBM-L (**a-b**) and GBM-M (**c-d**).

± 0.6 weeks for GBM-L, GBM-M, and the control group, respectively. Average body weight of the mice at the time of MRI experiments was 32.1 ± 5.9 g, 35.6 ± 3.3 g, and 31.4 ± 2.4 g for GBM-L, GBM-M, and the control group, respectively.

^{17}O images from a control mouse, KWIC versus standard reconstruction, are shown in Figure 5.3. At baseline and steady-state, the SNR of KWIC-reconstructed images was similar to that using standard reconstruction (10 for both methods at baseline, 30 versus 32 at steady-state). At peak $H_2{}^{17}O$ uptake, image reconstructed without k-space filtering failed to capture the rapid increase in ^{17}O signal. As a result, the signal intensity in images with the standard reconstruction was only ~75% of that using KWIC reconstruction.

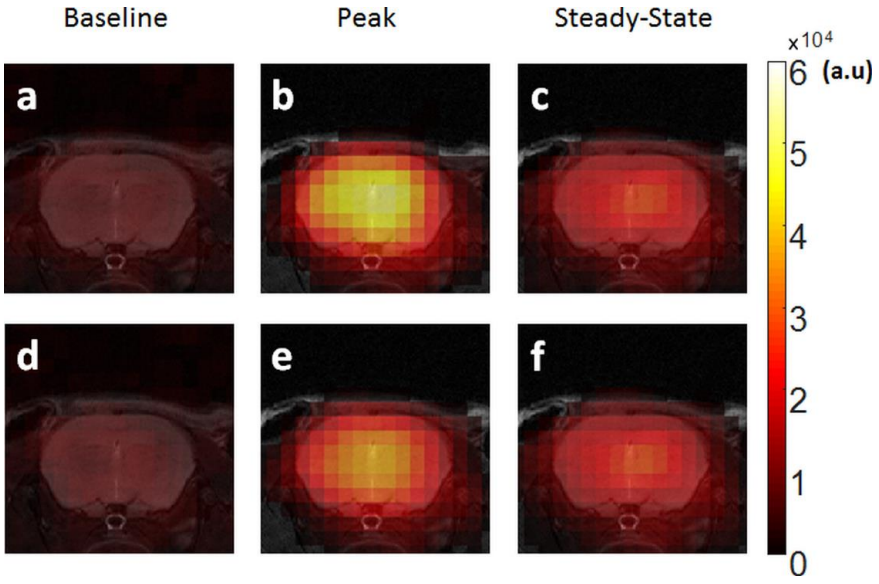

Figure 5.3. Representative ^{17}O images from a control mouse at baseline, peak and steady-state $H_2{}^{17}O$ uptake. **a-c**: KWIC reconstruction. **d-f**: Standard reconstruction using 100 spokes.

Figure 5.4 shows representative maps of peak and steady-state $H_2{}^{17}O$ uptake and washout rate from each group with typical time courses of ^{17}O signal observed in tumor and normal brain tissue. Group-averaged peak and steady-state $H_2{}^{17}O$ uptake and washout rate are shown in Figure 5.5. Baseline-normalized peak and steady-state $H_2{}^{17}O$ uptake in the brain of the control mice were 6.52 ± 0.86 and 3.36 ± 0.2, respectively, and the washout rate was 1.36 ± 0.28 min^{-1}. GBM mice showed more heterogeneous ^{17}O signal kinetics when compared to the control animals. In the GBM-M group, tumor tissue exhibited significantly reduced peak $H_2{}^{17}O$ uptake (5.45 ± 0.87, $p<0.05$) and decreased washout rate (0.88 ± 0.28 min^{-1}, $p<0.05$), suggesting decreased perfusion to the tumor. However, ^{17}O signal kinetics in the brain tissue was the same as the controls. On the contrary, GBM-L mice showed reduced $H_2{}^{17}O$ uptake and washout rate in both the tumor and the brain tissues. In the tumor tissue, no obvious washout phase, or even continued accumulation of $H_2{}^{17}O$, was observed after the injection.

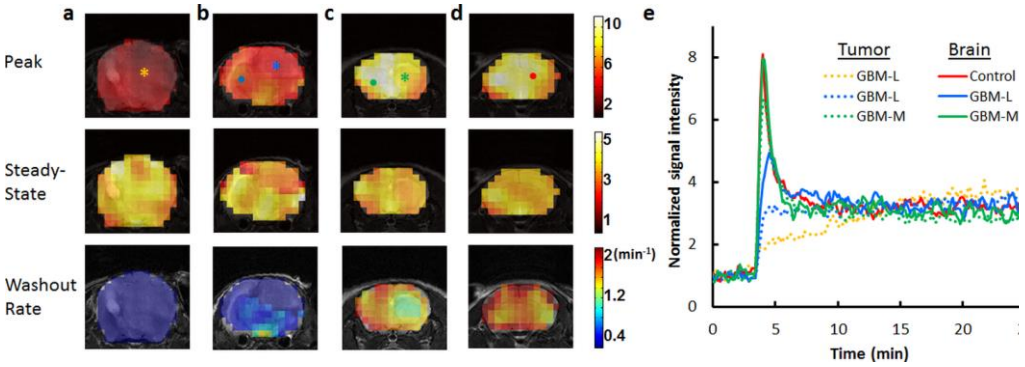

Figure 5.4. Reconstructed parameter maps and representative time courses. a-b: GBM-L mice. c: GBM-M mouse. d: Control mouse. e: Time courses of normalized ^{17}O signal changes in representative pixels indicated in (a-d). Tumor pixels are indicated by stars in (a-c) and their time courses are shown as dotted lines. Brain pixels are indicated by dots in (b-d) and their time courses are shown as solid lines.

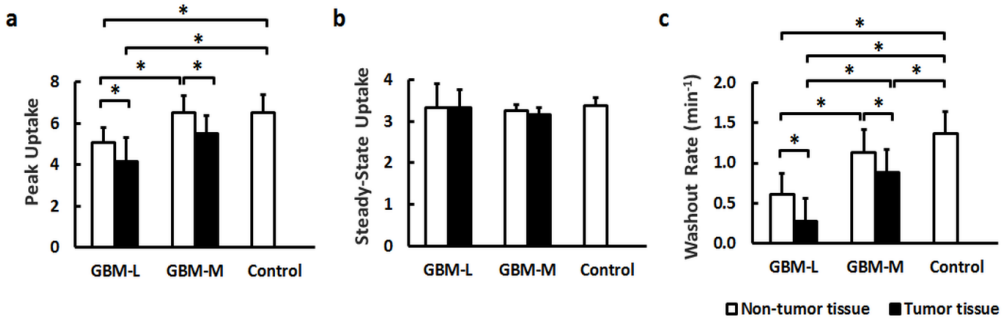

Figure 5.5. Group-averaged peak (**a**) and steady-state (**b**) $H_2{}^{17}O$ uptake and washout rate (**c**). *p<0.05.

5.3.2. In Vivo Results in the Stroke Mouse

In the stroke mouse, reduced $CMRO_2$ was detected by ^{17}O MRI (Figure 5.6b) while no edema was observed in T_2-weighted image (Figure 5.6a) at 2 hours after MCAO. At 4 hours after MCAO, edema was evident as shown in the T_2-weighted image (Figure 5.6c), which corresponded to the stroke area detected by ^{17}O MRI. Brain tissue shows a clear linear increase in $H_2{}^{17}O$ concentration during $^{17}O_2$ inhalation (Figure 5.6d). However, the stroke area shows abnormal oxygen consumption during inhalation as compared to the normal brain tissue (Figure 5.6d).These preliminary results suggest that ^{17}O MRI is a powerful tool for diagnosis at the early stage of stroke.

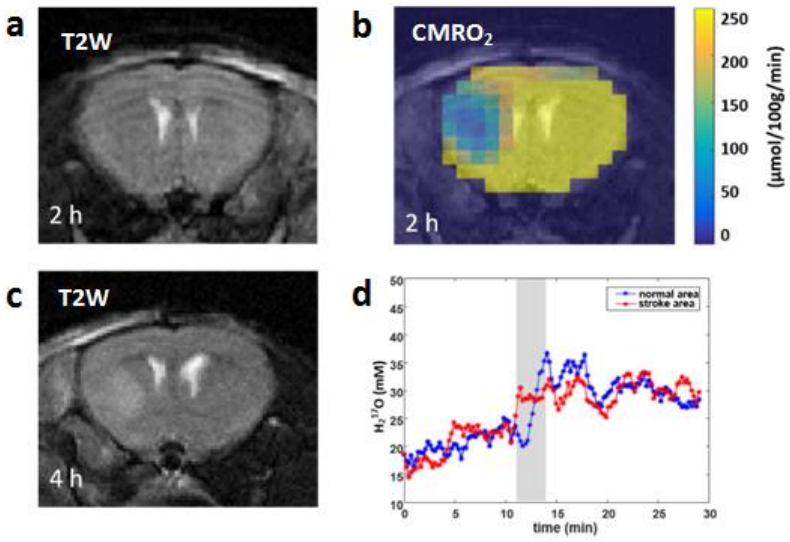

Figure 5.6. a: T_2-weighted ^1H images acquired at 2 hours after MCAO show no edema. **b:** $CMRO_2$ map calculated form ^{17}O MRI data shows deficiency in oxygen consumption in the stroke area. **c:** T_2-weighted ^1H images acquired at 4 hours after MCAO show edema in the stroke area. **d:** time course of $H_2{}^{17}O$ changes during the inhalation experiment in normal brain tissue (blue) and stroke area (red). The gray bar shows the inhalation peroid of 3 min 45 s.

5.4. Discussion and Conclusions

In the current study, the utility of a dynamic ^{17}O imaging method with a golden-ratio-based radial sampling profile and KWIC reconstruction in delineating the uptake and washout of water in the brain was demonstrated in a mouse model of GBM. The kinetics of $H_2{}^{17}O$ uptake and washout after an intravenous bolus injection of $H_2{}^{17}O$ were characterized by monitoring the ^{17}O signal directly with MRI. A temporal resolution of 7.56 s with a voxel size of 5.625 μL was achieved at 9.4T. Tumor tissue displayed a reduced peak $H_2{}^{17}O$ uptake and a diminished washout rate. Furthermore, the feasibility of the proposed ^{17}O MRI method for mapping $CMRO_2$ with high spatial resolution and temporal resolution was

demonstrated in the mouse brain with ischemic stroke. Deficits in $CMRO_2$ was detected by ^{17}O MRI before edema was observed in T_2-weighted ^{1}H images, suggesting ^{17}O MRI is a powerful tool for diagnosis at the early stage of stroke, and may potentially provide a promising tool to facilitate the assessment of ischemic penumbra in stroke patients. The initial experience in the current study shows this method is potentially applicable to numerous animal models to reveal abnormalities in water movement across the BBB and cerebral oxygen metabolism associated with various diseases.

Similar to $H_2{}^{15}O$ (218,219), the kinetics of $H_2{}^{17}O$ after a bolus injection is dominated by cerebral blood flow (154,164). As such, the reduced peak uptake and slower washout rate observed in the tumor tissue is likely due to compromised perfusion resulting from peritumoral edema (233–235). Continued accumulation of $H_2{}^{17}O$ during the washout phase was also observed in GBM-L mice, indicating impaired routes of water efflux in tumor tissues. Interestingly, GBM-L mice also exhibited significantly reduced peak $H_2{}^{17}O$ uptake and prolonged washout in the non-tumor region, suggesting that cerebral perfusion to normal brain tissue was also reduced in GBM-L mice. This reduction is likely caused by compression from the large tumor. Future studies with further evaluation of cerebral perfusion and grading of GBM will allow more precise delineation of the underlying mechanisms.

In stroke treatment, it is very important but challenging to identify and differentiate the irreversibly damaged brain tissue and the ischemic penumbra (potentially salvageable brain tissue) (236). The combination of diffusion-weighted MRI and perfusion-weighted MRI provides an imaging tool to assess the ischemic

penumbra. The ischemic core can be identified by diffusion-weighted MRI while the adjacent hypo-perfused tissue can be identified by perfusion-weighted MRI (236,237). This diffusion-perfusion mismatch approach potentially allows for the identification of the penumbra that is poorly perfused but reversibly damaged. However, it has been reported that it is not very reliable to predict the infarct growth based on diffusion-perfusion mismatch (238–241). In addition, the large variation in perfusion and apparent diffusion coefficient (ADC) threshold values leads to unreliability to identify the diffusion lesion and perfusion lesion (241). A direct approach to measure $CMRO_2$, CBF, and oxygen extraction fraction (OEF) may contribute to solve this problem (156). The current study measured $CMRO_2$ in the mouse brain with a brief inhalation of $^{17}O_2$. In principle, CBF could also be derived from the $H_2{}^{17}O$ concentration changes during the washout phase after inhalation, and OEF could be calculated based on the measured $CMRO_2$ and CBF (156). Simultaneous measurements of $CMRO_2$ and CBF are under investigation and will be implemented in future studies.

Dynamic hetero-nuclei imaging has been hindered by low SNR because of low nuclei abundance and signal sensitivity. Frequently, a large number of signal averages is used to achieve adequate SNR. However, it is at the cost of reduced temporal resolution. Alternatively, SNR can be gained by reducing spatial resolution, which increases the partial volume effect and may not be a feasible approach for small animal imaging. Using MRSI with Cartesian encoding, Zhu et al. reported a temporal resolution of 11 s with a voxel size of 40 μL (15 μL nominal) at 11.7 T in an inhalation study on stroked mice (156). In another study, Cui and

colleagues quantified $CMRO_2$ in mouse brain at 16.4 T with a temporal resolution of 15.4 s and a voxel size of 26 μL (9 μL nominal) (163). We were able to achieve an effective temporal resolution of 7.56 s with a nominal voxel size of 11.25 μL in a $H_2{}^{17}O$ injection study, and an effective temporal resolution of 14.04 s with a nominal voxel size of 10 μL in a $^{17}O_2$ inhalation study at 9.4T.

In order to achieve adequate SNR and temporal resolution to capture the different dynamics of ^{17}O signals after a bolus of $H_2{}^{17}O$ injection and during a brief period of $^{17}O_2$ inhalation, different signal averages, spatial resolution and k-space filters were used for the current injection and inhalation studies. Compared to $H_2{}^{17}O$ injection studies, $^{17}O_2$ inhalation studies yielded much lower SNR because only a small amount of gas is delivered in 2~4 min to reduce the cost for $^{17}O_2$ (156,163). Having a reduced amount of $^{17}O_2$ available in vivo causes reduced signal increases, leading to lower SNR at peak and steady-state. On the other hand, the rate of ^{17}O signal increase during an inhalation study is significantly slower than that in an injection study. Therefore, the decreased SNR can be compensated with increased signal averages, as the kinetics of ^{17}O signal in an inhalation study can be fully captured with a lower temporal resolution. A previous study on mice suggests that a 15-s temporal resolution is adequate for an inhalation study (163). The flexibility of choosing a k-space filter to optimize the trade-off among SNR, spatial, and/or temporal resolution allows application of this method to both $H_2{}^{17}O$ injection and $^{17}O_2$ inhalation studies.

In conclusion, the feasibility of 3D stack-of-stars ^{17}O MRI method combined with KWIC reconstruction was demonstrated in the mouse brain of GBM

and ischemic stroke, respectively. Tumor tissue displayed a reduced peak $H_2{}^{17}O$ uptake and a diminished washout rate, possibly caused by compromised cerebral perfusion. Furthermore, abnormalities in $CMRO_2$ in the stroke mouse was detected by ^{17}O MRI before edema was observed in T_2-weighted ^{1}H images, suggesting ^{17}O MRI is potentially more sensitive to pathological changes in cerebral metabolism associated with stroke. This method also provides a potential tool to facilitate the identification of ischemic penumbra in combination with the measurement of CBF.

Chapter 6. Conclusions and Future Perspectives

Hetero-nuclei MRI provides a unique tool to probe metabolism non-invasively and plays an important role in assessing functional cell processes such as oxidative metabolism in mitochondria. These hetero-nuclei include carbon-13 (^{13}C), sodium-23 (^{23}Na), phosphrous-31 (^{31}P), oxygen-17 (^{17}O), etc. This thesis focused on ^{31}P and ^{17}O for assessment of mitochondrial oxidative capacity in skeletal muscle and cerebral oxygen metabolism, respectively. Novel approaches for imaging ^{31}P and ^{17}O with high spatial resolution and temporal resolution were developed and demonstrated in small animals at high fields.

This chapter outlines future directions for the ^{31}P and ^{17}O MRS/I studies described in the previous chapters. Three aspects will be discussed: 1) further improvements of the proposed ^{31}P and ^{17}O MRS/I methods from the perspective of signal acquisition and reconstruction strategies; 2) general applications of the fast ^{31}P MRS/I methods in preclinical and clinical studies; 3) potential clinical applications of the ^{17}O MRI method in stroke patients.

6.1. Further Improvements of the ^{31}P and ^{17}O MRS/I Methods

SNR is the fundamental factor that limits the utility of hetero-nuclei MRI due to the intrinsic low MR sensitivity and low in vivo concentrations. In order to maximize SNR without sacrificing spatial or temporal resolutions, it is crucial to optimize signal acquisition approaches, from coil design to pulse sequence design. The following paragraphs will discuss optimized coil design, pulse sequence design,

and the potential to borrow dynamic MRI techniques that have been extensively used in proton MRI to accelerate hetero-nuclei MRI.

6.1.1. Coil Design

Quadrature coils are known to yield as much as 40% SNR increase compared to single coils by detecting signals from two orthogonal channels (242). This increase in SNR without sacrificing spatial resolution and temporal resolution is beneficial to all imaging and spectroscopy studies in general, but is particularly important to hetero-nuclei imaging given the low in vivo concentrations and low MR sensitivity of almost all hetero-nuclei. A quadrature surface coil has been used to measure ^{17}O relaxation times in vivo in rat brain at ultra-high field with excellent SNR (215). Quadrature coils have also been reported to measure ^{17}O and ^{23}Na signals in human brain (165,243). For ^{17}O inhalation studies in the mouse brain and ^{31}P MRSI studies in rat hindlimb, the size of the coils has to be relatively small to achieve optimized sensitivity. Despite the challenge to build very small coils and distribute tunable capacitors on it, quadrature coils are undoubtedly promising to enhance SNR for preclinical hetero-nuclei imaging studies with no penalty in spatial and temporal resolutions.

Another issue that should be considered is the potential coupling between the hetero-nuclei coil and the proton coil since the smaller hetero-nuclei coil is placed within the relatively big proton coil in order to acquire both proton reference images and hetero-nuclei images without moving the animal. In the current studies, the two coils are placed in the orientation that the directions of two B_1 fields are perpendicular to each other to minimize the coupling. Active decoupling between

the coils or dual-tune $^{1}H/^{31}P$ (or $^{1}H/^{17}O$) coils might solve this issue better for future studies.

6.1.2. Sequence Design for ^{31}P Studies

In the current ^{31}P MRSI study, a uniform density single-shot spiral trajectory was designed and implemented for spatial encoding. A total of 20 spirals were acquired continuously in one TR for spectral encoding without extra echo shift combining SPICE reconstruction. Alternatively, variable density multi-shots spirals can be employed and it may allow for more flexible spatial-spectral encoding schemes under SPICE framework.

Another direction for investigating mitochondrial function using ^{31}P MRI is to employ chemical selective MRI instead of MRSI as introduced in Chapter 1.3.4. The current ^{31}P MRSI study using SPICE described in Chapter 3 achieved unprecedented spatial resolution and temporal resolution, which is unrealistic using any conventional MRSI methods. Nevertheless, the SNR in rat skeletal muscle is still very low with such a high spatial resolution (nominal voxel size 0.78×0.78×1.6 mm^3) within 30s acquisition time. In order to measure mitochondrial oxidative capacity, only the quantification of PCr is required. It would be beneficial to quantify Pi and the chemical shift between Pi and PCr as well to calculate pH. Therefore, chemical selective imaging focusing on PCr and Pi can potentially yield better SNR due to the reduction of chemical shift dimension and still provides sufficient information for assessment of mitochondrial function. Particularly, a balanced steady-state free procession (bSSFP) framework has the potential to accelerate PCr imaging due to the short repetition time. In addition, T_2/T_1 contrast

provided by bSSFP is beneficial given the relatively long T_2 value of PCr (22,244). bSSFP-based sequence has been shown to achieve higher SNR per unit time especially for long T_2 values compared with FLASH-based sequence using optimized flip angle (136).

6.1.3. Sequence Design for ^{17}O Studies

In the ^{17}O-water injection and ^{17}O-gas inhalation studies as described in Chapter 4 and 5, 3D spatial encoding was achieved by a stack-of-stars ultrashort echo time sequence. This encoding approach yields fine in-plane resolution while relatively large voxel size in the third dimension. Moreover, the view sharing reconstruction was performed in k_x-k_y plane only, which did not take full advantage of 3D k-space sampling. In order to explore view sharing in all three dimensions, a 3D center-out radial trajectory based on golden-ratio profile order is worth investigation. A 3D radial trajectory (sampling from $-k_{max}$ to k_{max}) using multidimensional golden means has been reported to achieve improved temporal stability and robustness against artifacts in dynamic imaging for breast tumor diagnosis (245). This approach can be easily adapted for the design of golden-angle 3D center-out radial trajectories (sampling from k-space center to k_{max}). In brief, the location of the tip of a 3D spoke is determined by 2D golden means, φ_1 and φ_2, which are derived by solving the eigenvalue and eigenvector of the 3×3 modified Fibonacci matrix (245). Figure 6.1 shows the first five spokes designed by this approach. Combined with KWIC reconstruction, this acquisition scheme is promising to achieve more undersampling, which can be translated into higher

temporal resolution and/or spatial resolution, compared with the stack-of-stars sampling combined with in-plane KWIC reconstruction.

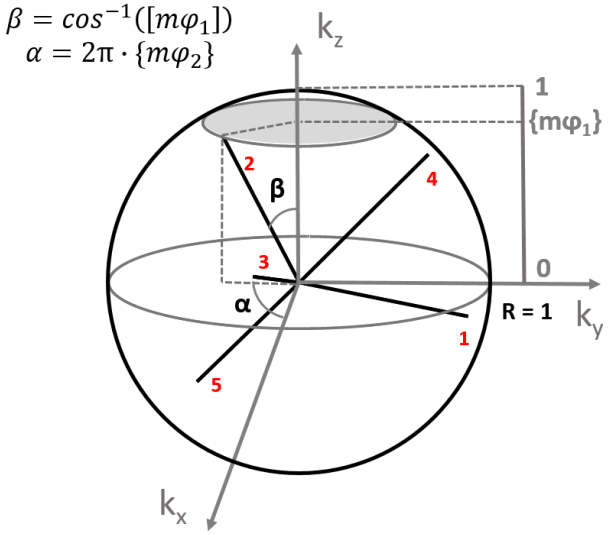

Figure 6.1. 3D center-out radial trajectory using multidimensional golden means. The first five spokes are shown and labeled with red numbers. The k_z location (angle β) of each spoke is determined based on φ_1. Once the kz location is fixed, the polar angle α in k_x-k_y plane is determined by φ_2. $[m\varphi_1]$ is the fractional part of $m\varphi_1$ redistributed in the range of [-1,1]; $\{m\varphi_2\}$ is the fractional part of $m\varphi_2$. $\varphi_1 \approx 0.4656$ and $\varphi_2 \approx 0.6823$ are derived from the 3×3 modified Fibonacci matrix. m = 1,2,3,…

6.1.4. Dynamic MRI Techniques

A variety of fast imaging techniques exploiting temporal and spatial redundancy of the images have emerged in recent years. These approaches boost the performance of dynamic imaging significantly by reducing scan duration, improving temporal resolution, and increase spatial resolution. Among these techniques, view sharing approaches such as MR fluoroscopy (246), keyhole (247,248), BRISK (249), CURE (250), TRICKS (251), TWIST (252), etc. exploit

temporal redundancy of the images; k-t approaches such as UNFOLD (253), k-t BLAST (254), k-t SENSE (254), etc. utilize spatiotemporal redundancy jointly. More details of the development of these techniques and the connections between them have been described in a comprehensive and insightful review by Tsao and Kozerke (255). Though these methods have been mainly used for proton imaging such as fMRI and MR angiography, they have great potential for dynamic hetero-nuclei imaging because the properties of the image function are essentially the same in spite of relatively low SNR.

In the ^{31}P MRSI study described in Chapter 3, a successful attempt has been made to apply ^{1}H SPICE approach to ^{31}P by exploiting the multi-dimensional correlations of the image function. On the other hand, the ^{17}O MRI studies described in Chapter 4 and 5 borrowed the concept of view sharing that is widely used in proton imaging and demonstrated the utility of this approach to measure water movement across blood-brain barrier and $CMRO_2$ successfully. Alternatively, k-t approaches (e.g., k-t BLAST) and compressed sensing techniques (143) are also potentially applicable to dynamic hetero-nuclei imaging. It is known that PCr follows an exponential function during recovery; and the concentration of metabolically produced $H_2{}^{17}O$ during inhalation can be modeled as a linear function. SPICE or k-t approaches may take advantage of these unique temporal properties of the image function for further accelerations.

6.2. Preclinical and Clinical Applications of ^{31}P MRS/I in General

In this thesis, the ^{31}P MRS method was applied to an animal model of type 2 diabetes to investigate the link between mitochondrial function in skeletal muscle

and insulin resistance. Diabetes is one of the most important applications of dynamic ^{31}P MRS/I. Nevertheless, the applications of ^{31}P MRS/I are not limited to diabetes. Indeed, pathophysiological changes in high-energy metabolism associated with or without diseases can all be investigated using ^{31}P MRS/I. In preclinical studies, ^{31}P MRS/I has been used to investigate altered energetics in animal models with disease in heart (36,256,257), liver (258), and brain (37,39,259). In clinical studies, it has also been applied to characterize muscle energetics (48,260,261), and alterations in energy metabolism in patients with fatty liver disease (41,168), lymphoma (52), schizophrenia (99), etc. Therefore, translation of the proposed fast ^{31}P MRS/I method to clinical scanners is worth exploring for metabolic investigations in a variety of organs in clinical research. Compared with preclinical studies in small animals at high fields, the lower field strength commonly used in clinical studies (e.g. 3T) can be compensated by much larger voxel size in humans to avoid SNR loss.

In addition, ^{31}P MT techniques allow in vivo quantification of metabolic fluxes via CK and ATP synthase at equilibrium conditions. This technique has been widely applied to quantify the CK reaction rate in heart, brain, and skeletal muscle (14,23,262–267). P_i to ATP flux has also been investigated in liver, heart, brain, and skeletal muscle (267–271). Combination of ^{31}P MT and dynamic ^{31}P MRS/I allows for non-invasive measurements both at equilibrium and during metabolic perturbations, and thereby provides comprehensive information on energy metabolism. Therefore, implementing both techniques in one study is worth exploring in future.

6.3. Potential Clinical Applications of ^{17}O MRI in Stroke Patients

The proposed ^{17}O MRI method was demonstrated in mouse models in this thesis, however, it can be easily translated to clinical research. In ^{17}O inhalation studies in human brain, a voxel size of 8~8.5 mm^3 was typically achieved using 3D radial acquisition with a frame rate of 40~50 s at high fields (≥7T) (165,272). As shown in Figure 5.3, an acceleration factor of ~5 was achieved without SNR loss using the golden-angle radial acquisition approach combined with view sharing reconstruction. Given the relationship between acquisition time and SNR, performing this method in human brain would allow for ~2.2 folds SNR gain with the same voxel size and temporal resolution (assuming other factors such as coil sensitivity and shimming conditions are the same). The SNR increase can be exchanged for either higher temporal resolution (from 50 s to 10 s) or smaller voxel size (from ~8 mm^3 to ~4 mm^3). In addition, as discussed in Chapter 6.1.3, 3D radial acquisition combined with 3D view sharing provides more potential for data undersampling and thereby more acceleration compared to the current stack-of-star approach. Hence, an acceleration factor of 5 is a conservative estimation and more acceleration is very promising for $CMRO_2$ imaging in clinical studies.

The identification of ischemic penumbra is a widely recognized problem in the treatment of stroke due to the absence of robust measurement techniques. $CMRO_2$ imaging by ^{17}O MRI in addition to perfusion and diffusion measurements provides comprehensive information about metabolic changes that is potentially helpful to identify penumbra. Therefore, the potential clinical application of the

proposed ^{17}O MRI method is promising to provide a sensitive and robust tool for penumbra identification and treatment evaluation in stroke patients.

In conclusion, the challenges of dynamic hetero-nuclei MRI in preclinical studies may be addressed by optimized coil design, sequence design suitable for the unique MR properties of the target nuclei, and dynamic imaging techniques that can be borrowed from proton imaging. Improvements of the aspects above will undoubtedly give rise to better SNR efficiency, higher spatial resolution or temporal resolution. The development and optimization of dynamic hetero-nuclei MRI techniques will open the door of non-invasive metabolic imaging and provide numerous opportunities to reveal alterations in metabolism and the underlying mechanisms associated with various diseases. These methods are also promising to be translated to clinical research for disease diagnosis and treatment evaluation.

Bibliography

1. Meyer RA, Sweeney HL, Kushmerick MJ. A simple analysis of the "phosphocreatine shuttle". Am. J. Physiol. 1984;246:C365-77.

2. Mlynárik V, Kasparová S, Liptaj T, Dobrota D, Horecký J, Belan V. Creatine kinase reaction rates in rat brain during chronic ischemia. MAGMA 1998;7:162–5.

3. Boeck CR, Carbonera LS, Milioli ME, Constantino LC, Garcez ML, Rezin GT, Scaini G, Streck EL. Mitochondrial respiratory chain and creatine kinase activities following trauma brain injury in brain of mice preconditioned with N-methyl-D-aspartate. Mol. Cell. Biochem. 2013;384:129–37. doi: 10.1007/s11010-013-1790-8.

4. Amaral AU, Cecatto C, Seminotti B, et al. Marked reduction of Na(+), K(+)-ATPase and creatine kinase activities induced by acute lysine administration in glutaryl-CoA dehydrogenase deficient mice. Mol. Genet. Metab. 2012;107:81–6. doi: 10.1016/j.ymgme.2012.04.015.

5. Toledo FGS. Mitochondrial involvement in skeletal muscle insulin resistance. Diabetes 2014;63:59–61. doi: 10.2337/db13-1427.

6. Sleigh A, Raymond-barker P, Thackray K, et al. Brief report Mitochondrial dysfunction in patients with primary congenital insulin resistance. 2011;121:2457–2461. doi: 10.1172/JCI46405.or.

7. Befroy DE, Petersen KF, Dufour S, Mason GF, Graaf RA De, Rothman DL, Shulman GI. Impaired Mitochondrial Substrate Oxidation in Muscle of Insulin-

Resistant Offspring of Type 2 Diabetic Patients. 2007;56. doi: 10.2337/db06-0783.COX.

8. Meyer RA. A linear model of muscle respiration explains monoexponential phosphocreatine changes. Am. J. Physiol. 1988;254:C548–C553.

9. Challiss RA, Vranic M, Radda GK. Bioenergetic changes during contraction and recovery in diabetic rat skeletal muscle. Am J Physiol. 1989 Jan;256:E129-37.

10. Soussi B, Idström JP, Bylund-Fellenius AC, Scherstén T. Dynamics of skeletal muscle energetics during ischemia and reperfusion assessed by in vivo 31P NMR. NMR Biomed. 1990;3:71–7.

11. Morikawa S, Kido C, Inubushi T. Observation of rat hind limb skeletal muscle during arterial occlusion and reperfusion by 31P MRS and 1H MRI. Magn. Reson. Imaging 1991;9:269–274. doi: 10.1016/0730-725X(91)90411-E.

12. Paganini AT, Foley JM, Meyer RA. Linear dependence of muscle phosphocreatine kinetics on oxidative capacity. Am. J. Physiol. 1997;272:C501–C510.

13. Lauterbur PC. Image Formation by Induced Local Interactions: Examples Employing Nuclear Magnetic Resonance. Nature 1973;242:190–191. doi: 10.1038/242190a0.

14. Ingwall JS. Phosphorus nuclear magnetic resonance spectroscopy of cardiac and skeletal muscles. Am. J. Physiol. 1982;242:H729-44.

15. Suzuki E, Maeda M, Kuki S, Steward MC, Takami H, Seo Y, Murakami M,

Watari H. Adenosine triphosphate compartmentation in the rat heart: a 31P spin-lattice relaxation study. J. Biochem. 1990;107:559–62.

16. Kingsley-Hickman PB, Sako EY, Uğurbil K, From a H, Foker JE. 31P NMR measurement of mitochondrial uncoupling in isolated rat hearts. J. Biol. Chem. 1990;265:1545–50.

17. Newman RJ. Clinical applications of nuclear magnetic resonance spectroscopy: a review. J R Soc Med. 1984 Sep; 77(9): 774–779.e 77.

18. Gadian DG, Radda GK. NMR studies of tissue metabolism. Annu. Rev. Biochem. 1981;50:69–83. doi: 10.1146/annurev.bi.50.070181.000441.

19. Cady E, Costello A, Dawson M, Delpy D, Hope P, Reynolds E, Tofts P, Wilkie D. Non-invasive investigation of cerebral metabolism in newborn infants by phosphorus nuclear magnetic resonance spectroscopy. Lancet. 1983 May 14;1(8333):1059-62.

20. Hope P, Costello A, Cady E, Delpy D, Tofts P, Chu A, Hamilton P, Reynolds E, Wilkie D. Cerebral Energy Metabolism Studied With Phosphorus NMR Spectroscopy in Normal and Birth-asphyxiated Infants. Lancet. 1984 Aug 18;2(8399):366-70.

21. Graham J. Kemp, Martin Meyerspeer EM. Absolute quantification of phosphorus metabolite concentrations in human muscle in vivo by 31P MRS: a quantitative review. NMR Biomed. 2007;20:555–565. doi: 10.1002/nbm.

22. Meyerspeer M, Krššák M, Moser E. Relaxation times of 31P-metabolites in human calf muscle at 3 T. Magn. Reson. Med. 2003;49:620–625. doi:

10.1002/mrm.10426.

23. Lei H, Zhu X-H, Zhang X-L, Ugurbil K, Chen W. In vivo 31P magnetic resonance spectroscopy of human brain at 7 T: an initial experience. Magn. Reson. Med. 2003;49:199–205. doi: 10.1002/mrm.10379.

24. Qiao H, Zhang X, Zhu XH, Du F, Chen W. In vivo 31P MRS of human brain at high/ultrahigh fields: a quantitative comparison of NMR detection sensitivity and spectral resolution between 4 T and 7 T. Magn. Reson. Imaging 2006;24:1281–1286. doi: 10.1016/j.mri.2006.08.002.

25. Bogner W, Chmelik M, Schmid AI, Moser E, Trattnig S, Gruber S. Assessment of 31P relaxation times in the human calf muscle: A comparison between 3 T and 7 T in vivo. Magn. Reson. Med. 2009;62:574–582. doi: 10.1002/mrm.22057.

26. Ernst RR. Numerical Hilbert transform and automatic phase correction in magnetic resonance spectroscopy. J. Magn. Reson. 1969;1:7–26. doi: 10.1016/0022-2364(69)90003-1.

27. Wang T, Shao K, Chu Q, Ren Y, Mu Y, Qu L, He J, Jin C, Xia B. Automics: an integrated platform for NMR-based metabonomics spectral processing and data analysis. BMC Bioinformatics 2009;10:83. doi: 10.1186/1471-2105-10-83.

28. Chen L, Weng Z, Goh L, Garland M. An efficient algorithm for automatic phase correction of NMR spectra based on entropy minimization. J. Magn. Reson. 2002;158:164–168. doi: 10.1016/S1090-7807(02)00069-1.

29. Sibisi S, Skilling J, Brereton RG, Laue ED, Staunton J. Maximum entropy

signal processing in practical NMR spectroscopy. Nature 1984;311:446–447. doi: 10.1038/311446a0.

30. Brown DE. Fully automated baseline correction of 1D and 2D NMR spectra using bernstein polynomials. J. Magn. Reson. 1995;114:268–270. doi: 10.1006/jmra.1995.1138.

31. Schulze G, Jirasek A, Yu MML, Lim A, Turner RFB, Blades MW. Investigation of selected baseline removal techniques as candidates for automated implementation. Appl. Spectrosc. 2005;59:545–574. doi: 10.1366/0003702053945985.

32. Golotvin S, Williams A. Improved baseline recognition and modeling of FT NMR spectra. J. Magn. Reson. 2000;146:122–5. doi: 10.1006/jmre.2000.2121.

33. Dietrich W, Rüdel CH, Neumann M. Fast and precise automatic baseline correction of one- and two-dimensional nmr spectra. J. Magn. Reson. 1991;91:1–11. doi: 10.1016/0022-2364(91)90402-F.

34. Roth K, Hubesch B, Meyerhoff DJ, Naruse S, Gober JR, Lawry TJ, Boska MD, Matson GB, Weiner MW. Noninvasive quantitation of phosphorus metabolites in human tissue by NMR spectroscopy. J. Magn. Reson. 1989;81:299–311. doi: 10.1016/0022-2364(89)90062-0.

35. Parasoglou P, Xia D, Regatte RR. Spectrally selective 3D TSE imaging of phosphocreatine in the human calf muscle at 3 T. Magn. Reson. Med. 2013;69:812–7. doi: 10.1002/mrm.24288.

36. Weiss RG, Chatham JC, Georgakopolous D, et al. An increase in the

myocardial PCr/ATP ratio in GLUT4 null mice. FASEB J. 2002;16:613–5.

37. Braun KP, Dijkhuizen RM, de Graaf RA, Nicolay K, Vandertop WP, Gooskens RH, Tulleken KA. Cerebral ischemia and white matter edema in experimental hydrocephalus: a combined in vivo MRI and MRS study. Brain Res. 1997;757:295–8.

38. Shivu GN, Abozguia K, Phan TT, Ahmed I, Henning A, Frenneaux M. 31P magnetic resonance spectroscopy to measure in vivo cardiac energetics in normal myocardium and hypertrophic cardiomyopathy: Experiences at 3 T. Eur. J. Radiol. 2010;73:255–259. doi: 10.1016/j.ejrad.2008.10.018.

39. Saggu R. Characterisation of Endothelin-1-Induced Intrastriatal Lesions Within the Juvenile and Adult Rat Brain Using MRI and 31P MRS. Transl. Stroke Res. 2013;4:351–367. doi: 10.1007/s12975-013-0258-1.

40. Chanseaume E, Bielicki G, Tardy A-L, Renou J-P, Freyssenet D, Boirie Y, Morio B. Impaired resting muscle energetics studied by (31)P-NMR in diet-induced obese rats. Obesity (Silver Spring). 2008;16:572–7. doi: 10.1038/oby.2007.91.

41. Sharma R, Sinha S, Danishad KA, Vikram NK, Gupta A, Ahuja V, Jagannathan NR, Pandey RM, Misra A. Investigation of hepatic gluconeogenesis pathway in non-diabetic Asian Indians with non-alcoholic fatty liver disease using in vivo (31P) phosphorus magnetic resonance spectroscopy. Atherosclerosis 2009;203:291–297. doi: 10.1016/j.atherosclerosis.2008.06.016.

42. Bottomley PA, Drayer BP, Smith LS. Chronic adult cerebral infarction

studied by phosphorus NMR spectroscopy. Radiology 1986;160:763–766. doi: 10.1148/radiology.160.3.3737915.

43. Hove M, Neubauer S. Evaluating metabolic changes in heart disease by magnetic resonance spectroscopy. Hear. Metab 2006;32:18–21.

44. Giannesini B, Vilmen C, Le Fur Y, Dalmasso C, Cozzone PJ, Bendahan D. A strictly noninvasive MR setup dedicated to longitudinal studies of mechanical performance, bioenergetics, anatomy, and muscle recruitment in contracting mouse skeletal muscle. Magn. Reson. Med. 2010;64:262–70. doi: 10.1002/mrm.22386.

45. Wiseman RW, Kushmerick MJ. Creatine kinase equilibration follows solution thermodynamics in skeletal muscle: 31P NMR studies using creatine analogs. J. Biol. Chem. 1995;270:12428–12438. doi: 10.1074/jbc.270.21.12428.

46. Kemp GJ, Taylor DJ, Thompson CH, Hands LJ, Rajagopalan B, Styles P, Radda GK. Quantitative analysis by 31P magnetic resonance spectroscopy of abnormal mitochondrial oxidation in skeletal muscle during recovery from exercise. NMR Biomed. 1993;6:302–310. doi: 10.1002/nbm.1940060504.

47. Harkema SJ, Meyer RA. Effect of acidosis on control of respiration in skeletal muscle. Am. J. Physiol. 1997;272:C491-500.

48. Kemp GJ, Roussel M, Bendahan D, Le Fur Y, Cozzone PJ. Interrelations of ATP synthesis and proton handling in ischaemically exercising human forearm muscle studied by 31P magnetic resonance spectroscopy. J. Physiol. 2001;535:901–928. doi: 10.1111/j.1469-7793.2001.00901.x.

49. Soussi B, Idström JP, Bylund-Fellenius a C, Scherstén T. Dynamics of skeletal muscle energetics during ischemia and reperfusion assessed by in vivo 31P NMR. NMR Biomed. 1990;3:71–7.

50. Petroff O a, Prichard JW, Behar KL, Alger JR, den Hollander J a, Shulman RG. Cerebral intracellular pH by 31P nuclear magnetic resonance spectroscopy. Neurology 1985;35:781–8.

51. Barker PB, Butterworth EJ, Boska MD, Nelson J, Welch KM. Magnesium and pH imaging of the human brain at 3.0 Tesla. Magn. Reson. Med. 1999;41:400–6. doi: 10.1002/(SICI)1522-2594(199902)41:2<400::AID-MRM26>3.0.CO;2-E.

52. Rata M, Giles SL, deSouza NM, Leach MO, Payne GS. Comparison of three reference methods for the measurement of intracellular pH using 31P MRS in healthy volunteers and patients with lymphoma. NMR Biomed. 2014;27:158–162. doi: 10.1002/nbm.3047.

53. Befroy DE, Shulman GI. Magnetic resonance spectroscopy studies of human metabolism. Diabetes 2011;60:1361–1369. doi: 10.2337/db09-0916.

54. Morikawa S, Kido C, Inubushi T. Observation of rat hind limb skeletal muscle during arterial occlusion and reperfusion by 31P MRS and 1H MRI. Magn. Reson. Imaging 1991;9:269–274. doi: 10.1016/0730-725X(91)90411-E.

55. Marro KI, Olive JL, Hyyti OM, Kushmerick MJ. Time-courses of perfusion and phosphocreatine in rat leg during low-level exercise and recovery. J. Magn. Reson. Imaging 2007;25:1021–7. doi: 10.1002/jmri.20903.

56. Lanza IR, Bhagra S, Nair KS, Port JD. Measurement of human skeletal

muscle oxidative capacity by 31P-MR spectroscopy: A cross-validation with in vitro measurements. J. Magn. Reson. Imaging 2011;34:1143–1150. doi: 10.1002/jmri.22733.

57. Miller RG, Boska MD, Moussavi RS, Carson PJ, Weiner MW. ^{31}P nuclear magnetic resonance studies of high energy phosphates and pH in human muscle fatigue. Comparison of aerobic and anaerobic exercise. J. Clin. Invest. 1988;81.

58. Forbes SC, Paganini AT, Slade JM, Towse TF, Meyer R a. Phosphocreatine recovery kinetics following low- and high-intensity exercise in human triceps surae and rat posterior hindlimb muscles. Am. J. Physiol. Regul. Integr. Comp. Physiol. 2009;296:R161–R170. doi: 10.1152/ajpregu.90704.2008.

59. Perry CGR, Kane DA, Lanza IR, Neufer PD. Methods for assessing mitochondrial function in diabetes. Diabetes 2013;62:1041–53. doi: 10.2337/db12-1219.

60. Macia M, Pecchi E, Vilmen C, Desrois M, Lan C, Portha B, Bernard M, Bendahan D, Giannesini B. Insulin Resistance Is Not Associated with an Impaired Mitochondrial Function in Contracting Gastrocnemius Muscle of Goto-Kakizaki Diabetic Rats In Vivo. PLoS One 2015;10:e0129579. doi: 10.1371/journal.pone.0129579.

61. Liu Y, Mei X, Li J, Lai N, Yu X. Mitochondrial function assessed by ^{31} P MRS and BOLD MRI in non-obese type 2 diabetic rats. Physiol. Rep. 2016;4:e12890. doi: 10.14814/phy2.12890.

62. Parasoglou P, Xia D, Chang G, Regatte RR. Dynamic three-dimensional

imaging of phosphocreatine recovery kinetics in the human lower leg muscles at 3T and 7T: A preliminary study. NMR Biomed. 2013;26:348–356. doi: 10.1002/nbm.2866.

63. Shah PK, Ye F, Liu M, Jayaraman A, Baligand C, Walter G, Vandenborne K. In vivo (31)P NMR spectroscopy assessment of skeletal muscle bioenergetics after spinal cord contusion in rats. Eur. J. Appl. Physiol. 2014;114:847–58. doi: 10.1007/s00421-013-2810-9.

64. Scheuermann-Freestone M, Madsen PL, Manners D, Blamire AM, Buckingham RE, Styles P, Radda GK, Neubauer S, Clarke K. Abnormal Cardiac and Skeletal Muscle Energy Metabolism in Patients With Type 2 Diabetes. Circulation 2003;107.

65. Broek NMA Van Den, Ciapaite J, Nicolay K, Prompers JJ. Comparison of in vivo postexercise phosphocreatine recovery and resting ATP synthesis flux for the assessment of skeletal muscle mitochondrial function. 2010:1136–1143. doi: 10.1152/ajpcell.00200.2010.

66. Ernst RR. Application of Fourier Transform Spectroscopy to Magnetic Resonance. Rev. Sci. Instrum. 1966;37:93. doi: 10.1063/1.1719961.

67. Bottomley P. Selective volume method for performing localized NMR spectroscopy. Magn. Reson. Imaging 1985;3:iv–v. doi: 10.1016/0730-725X(85)90032-3.

68. Bottomley PA. Spatial localization in NMR spectroscopy in vivo. Ann N Y Acad Sci 1987;508:333–348.

69. Frahm J, Merboldt K-D, Hänicke W. Localized proton spectroscopy using stimulated echoes. J. Magn. Reson. 1987;72:502–508. doi: 10.1016/0022-2364(87)90154-5.

70. Dreher W, Schuster C, Leibfritz D. Short TE PRESS Proton NMR Spectroscopy without Water Suppression. Application to the Human Brain at 3 Tesla. Proc. 14th Sci. Meet. Int. Soc. Magn. Reson. Med. 2006;2:3066.

71. Dreher W, Leibfritz D. Detection of homonuclear decoupled in vivo proton NMR spectra using constant time chemical shift encoding: CT-PRESS. Magn. Reson. Imaging 1999;17:141–150. doi: 10.1016/S0730-725X(98)00156-8.

72. Terpstra M, Ugurbil K, Tkac I. Noninvasive quantification of human brain ascorbate concentration using 1H NMR spectroscopy at 7 T. NMR Biomed. 2010;23:227–32. doi: 10.1002/nbm.1423.

73. Dreher W, Ebel D, Leibfritz D. Optimized CT-PRESS for Localized Proton NMR Spectroscopy of the Human Brain at 3 Tesla. Proc. Intl. Soc. Mag. Reson. Med. 16 (2008) 1611.

74. Moonen CT, von Kienlin M, van Zijl PC, Cohen J, Gillen J, Daly P, Wolf G. Comparison of Single-shot Localization Methods (STEAM and PRESS) for In Vivo Proton NMR Spectroscopy. NMR Biomed. 1989;2(5-6):201-8.

75. Ordidge R, Connelly A, Lohman J. Image-selected in vovo spectroscopy (ISIS) a new technique for spatially selective NMR spectroscopy. J Magn Reson 1986;66:283–294.

76. Lamb HJ, Doornbos J, den Hollander J a, Luyten PR, Beyerbacht HP, van der

Wall EE, de Roos a. Reproducibility of human cardiac 31P-NMR spectroscopy. NMR Biomed. 1996;9:217–27. doi: 10.1002/(SICI)1099-1492(199608)9:5<217::AID-NBM419>3.0.CO;2-G.

77. Luyten PR, Groen JP, Vermeulen JWAH, Den Hollander JA. Experimental approaches to image localized human 31P NMR spectroscopy. Magn. Reson. Med. 1989;11:1–21. doi: 10.1002/mrm.1910110102.

78. Sprott H, Rzanny R, Reichenbach JR, Kaiser W a, Hein G, Stein G. 31P magnetic resonance spectroscopy in fibromyalgic muscle. Rheumatology (Oxford). 2000;39:1121–1125.

79. Bakermans AJ, Abdurrachim D, van Nierop BJ, et al. In vivo mouse myocardial 31P MRS using three-dimensional image-selected in vivo spectroscopy (3D ISIS): Technical considerations and biochemical validations. NMR Biomed. 2015;28:1218–1227. doi: 10.1002/nbm.3371.

80. Chmelik M, Považan M, Kršňák M, Gruber S, Tkačov M, Trattnig S, Bogner W. In vivo 31P magnetic resonance spectroscopy of the human liver at 7T: An initial experience. NMR Biomed. 2014;27:478–485. doi: 10.1002/nbm.3084.

81. Kitagawa A, Saeki M, Imamura K, Ohashi K, Ishikawa T, Nakajima H, Takagi M. 31P-MR spectroscopy of bone and soft tissue lesions. Nihon Igaku Hoshasen Gakkai Zasshi. 1995;55:1017–1024.

82. Keevil SF. Spatial localization in nuclear magnetic resonance spectroscopy. Phys. Med. Biol. 2006;51:R579–R636. doi: 10.1088/0031-9155/51/16/R01.

83. Greenman RL, Elliott MA, Vandenborne K, Schnall MD, Lenkinski RE. Fast

Imaging of Phosphocreatine Using a RARE Pulse Sequence. Magn. Reson. Med. 1998;39:851–854.

84. Greenman RL, Axel L, Ferrari VA, Lenkinski RE. Fast Imaging of Phosphocreatine in the Normal Human Myocardium Using a Three-Dimensional RARE Pulse Sequence at 4 Tesla. J Magn Reson Imaging. 2002;15(4):467–472. doi: 10.1002/jmri.10081.

85. Greenman RL. Quantification of the 31P metabolite concentration in human skeletal muscle from RARE image intensity. Magn. Reson. Med. 2004;52:1036–42. doi: 10.1002/mrm.20258.

86. Greenman RL, Smithline HA. The Feasibility of Measuring Phosphocreatine Recovery Kinetics in Muscle Using Single-Shot 31 P RARE MRI Sequence. Acad Radiol 2011;18:917–923. doi: 10.1016/j.micinf.2011.07.011.Innate.

87. Greenman RL, Wang X, Smithline HA. Simultaneous acquisition of phosphocreatine and inorganic phosphate images for Pi:PCr ratio mapping using a RARE sequence with chemically selective interleaving. Magn. Reson. Imaging 2011;29:1138–44. doi: 10.1016/j.mri.2011.05.001.

88. Parasoglou P, Feng L, Xia D, Otazo R, Regatte RR. Rapid 3D-imaging of phosphocreatine recovery kinetics in the human lower leg muscles with compressed sensing. Magn. Reson. Med. 2012;68:1738–46. doi: 10.1002/mrm.24484.

89. Parasoglou P, Xia D, Chang G, Convit A, Regatte RR. Three dimensional mapping of the creatine kinase enzyme reaction rate in muscles of the lower leg.

NMR Biomed. 2013;26:1142–1151. doi: 10.1016/j.immuni.2010.12.017.Two-stage.

90. Parasoglou P, Xia D, Chang G, Regatte RR. Three-dimensional saturation transfer ^{31}P-MRI in muscles of the lower leg at 3.0 T. Sci. Rep. 2014;4:5219. doi: 10.1038/srep05219.

91. Lee RF, Giaquinto R, Constantinides C, Souza S, Weiss RG, Bottomley PA. A broadband phased-array system for direct phosphorus and sodium metabolic MRI on a clinical scanner. Magn. Reson. Med. 2000;43:269–277. doi: 10.1002/(SICI)1522-2594(200002)43:2<269::AID-MRM14>3.0.CO;2-J.

92. Lu A, Atkinson IC, Zhou XJ, Thulborn KR. PCr/ATP ratio mapping of the human head by simultaneously imaging of multiple spectral peaks with interleaved excitations and flexible twisted projection imaging readout trajectories at 9.4 T. Magn. Reson. Med. 2013;69:538–544. doi: 10.1002/mrm.24281.

93. Schmid AI. Dynamic PCr and pH Imaging of Human Calf Muscles During Exercise and Recovery Using 31P Gradient-Echo MRI at 7 Tesla. Magn. Reson. Med. 2014;0:1–8. doi: 10.1002/mrm.25822.

94. Pohmann R, von Kienlin M, Haase A. Theoretical evaluation and comparison of fast chemical shift imaging methods. J. Magn. Reson. 1997;129:145–160. doi: 10.1006/jmre.1997.1245.

95. Skoch A, Jiru F, Bunke J. Spectroscopic imaging: Basic principles. Eur. J. Radiol. 2008;67:230–239. doi: 10.1016/j.ejrad.2008.03.003.

96. Posse S, Otazo R, Dager SR, Alger J. MR spectroscopic imaging: Principles

and recent advances. J. Magn. Reson. Imaging 2013;37:1301–1325. doi: 10.1002/jmri.23945.

97. de Graaf RA. In Vivo NMR Spectroscopy: Principles and Techniques: 2nd Edition. 2007. doi: 10.1002/9780470512968.

98. Eric Jensen J, Drost DJ, Menon RS, Williamson PC. In vivo brain 31P-MRS: Measuring the phospholipid resonances at 4 Tesla from small voxels. NMR Biomed. 2002;15:338–347. doi: 10.1002/nbm.776.

99. Jensen JE, Miller J, Williamson PC, Neufeld RWJ, Menon RS, Malla A, Manchanda R, Schaefer B, Densmore M, Drost DJ. Grey and white matter differences in brain energy metabolism in first episode schizophrenia: 31P-MRS chemical shift imaging at 4 Tesla. Psychiatry Res. - Neuroimaging 2006;146:127–135. doi: 10.1016/j.pscychresns.2005.11.004.

100. Ha DH, Choi S, Oh JY, Yoon SK, Kang MJ, Kim KU. Application of 31P MR spectroscopy to the brain tumors. Korean J. Radiol. 2013;14:477–486. doi: 10.3348/kjr.2013.14.3.477.

101. Murphy-Boesch J, Stoyanova R, Srinivasan R, Willard T, Vigneron D, Nelson S, Taylor JS, Brown TR. Proton-decoupled 31P chemical shift imaging of the human brain in normal volunteers. NMR Biomed. 1993;6:173–180. doi: 10.1002/nbm.1940060302.

102. Nahrendorf M, Hiller K-H, Greiser A, et al. Chronic coronary artery stenosis induces impaired function of remote myocardium: MRI and spectroscopy study in rat. Am. J. Physiol. Heart Circ. Physiol. 2003;285:H2712-21. doi:

10.1152/ajpheart.00233.2003.

103. Flögel U, Jacoby C, Gödecke A, Schrader J. In vivo 2D mapping of impaired murine cardiac energetics in NO-induced heart failure. Magn. Reson. Med. 2007;57:50–8. doi: 10.1002/mrm.21101.

104. Chmelík M, Schmid a. I, Gruber S, Szendroedi J, Krššák M, Trattnig S, Moser E, Roden M. Three-dimensional high-resolution magnetic resonance spectroscopic imaging for absolute quantification of 31P metabolites in human liver. Magn. Reson. Med. 2008;60:796–802. doi: 10.1002/mrm.21762.

105. Dezortova M, Taimr P, Skoch A, Spicak J, Hajek M. Etiology and functional status of liver cirrhosis by 31P MR spectroscopy. World J. Gastroenterol. 2005;11:6926–6931.

106. Schlemmer HPW, Sawatzki T, Sammet S, Dornacher I, Bachert P, Van Kaick G, Waldherr R, Seitz HK. Hepatic phospholipids in alcoholic liver disease assessed by proton-decoupled 31P magnetic resonance spectroscopy. J. Hepatol. 2005;42:752–759. doi: 10.1016/j.jhep.2004.12.032.

107. Vyhnanovská P, Dezortová M, Herynek V, Táborský P, Viklický O, Hájek M. In vivo 31P MR spectroscopy of human kidney grafts using the 2D-chemical shift imaging method. Transplant. Proc. 2011;43:1570–5. doi: 10.1016/j.transproceed.2010.11.027.

108. Jeneson JA, Nelson SJ, Vigneron DB, Taylor JS, Murphy-Boesch J, Brown TR. Two-dimensional 31P-chemical shift imaging of intramuscular heterogeneity in exercising human forearm muscle. Am. J. Physiol. 1992;263:C357-64.

109. Forbes SC, Slade JM, Francis RM, Meyer RA. Comparison of oxidative capacity among leg muscles in humans using gated 31P 2-D chemical shift imaging. NMR Biomed. 2009;22:1063–71. doi: 10.1002/nbm.1413.

110. Cannon DT, Howe FA, Whipp BJ, Ward S a, McIntyre DJ, Ladroue C, Griffiths JR, Kemp GJ, Rossiter HB. Muscle metabolism and activation heterogeneity by combined 31P chemical shift and T2 imaging, and pulmonary O2 uptake during incremental knee-extensor exercise. J. Appl. Physiol. 2013;115:839–49. doi: 10.1152/japplphysiol.00510.2013.

111. Kanayama T, Minowa K, Inoue N, Yamaguchi T, Yoshida S, Kawasaki T. Regional differences of metabolism in human masseter muscle by two-dimensional 31P-chemical shift imaging. J. Dent. Res. 2000;79:85–9.

112. Maudsley AA, Matson GB, Hugg JW, Weiner MW. Reduced phase encoding in spectroscopic imaging. Magn. Reson. Med. 1994;31:645–651. doi: 10.1002/mrm.1910310610.

113. Guimaraes AR, Baker JR, Jenkins BG, Lee PL, Weisskoff RM, Rosen BR, Gonza RG. Echoplanar Chemical Shift Imaging. 1999;882:877–882.

114. Ebel A, Zhu X, Weiner M, Ji J, Schuff N. Sensitivity Encoded Three Dimensional Echo Planar Spectroscopic Imaging (3D-EPSI) of Human Brain at 4T. Proc. Intl. Soc. Mag. Reson. Med. 14 (2006) 3075.

115. Ebel A, Schuff N. Repeated Measures Performance of Whole-Brain Echo-Planar Spectroscopic Imaging at 4 Tesla. Proc. Intl. Soc. Mag. Reson. Med. 17 (2009) 4318.

116. Posse S, Tedeschi G, Risinger R, Ogg R, Bihan DL. High Speed 1H Spectroscopic Imaging in Human Brain by Echo Planar Spatial-Spectral Encoding. Magn. Reson. Med. 1995;33:34–40. doi: 10.1002/mrm.1910330106.

117. Posse S, DeCarli C, Le Bihan D. Three-dimensional echo-planar MR spectroscopic imaging at short echo times in the human brain. Radiology 1994;192:733–738. doi: 10.1148/radiology.192.3.8058941.

118. Ozturk E, Chen A, Pels P, Nelson S, Zierhut M, Cunningham C, Vigneron D. Spectroscopic Imaging of 1H at 3T: Comparing SNR between Traditional Phase Encoding and Echo-Planar Techniques in the Human Brain. In: Proc. Intl. Soc. Mag. Reson. Med. 14 (2006) 65.

119. Korzowski A, Bachert P. High-resolution ^{31} P echo-planar spectroscopic imaging in vivo at 7T. Magn. Reson. Med. 2017;0:1–9. doi: 10.1002/mrm.26785.

120. Adalsteinsson E, Irarrazabal P, Topp S, Meyer C, Macovski A, Spielman DM. Volumetric spectroscopic imaging with spiral-based k-space trajectories. Magn. Reson. Med. 1998;39:889–98.

121. Ramirez MS, Lee J, Walker CM, Sandulache VC, Hennel F, Lai SY, Bankson J a. Radial spectroscopic MRI of hyperpolarized [1-(13) C] pyruvate at 7 tesla. Magn. Reson. Med. 2014;72:986–95. doi: 10.1002/mrm.25004.

122. Schirda C V, Tanase C, Boada FE. Rosette spectroscopic imaging: optimal parameters for alias-free, high sensitivity spectroscopic imaging. J. Magn. Reson. Imaging 2009;29:1375–85. doi: 10.1002/jmri.21760.

123. Fessler JA, Sutton BP. Nonuniform fast fourier transforms using min-max

interpolation. IEEE Trans. Signal Process. 2003;51:560–574. doi: 10.1109/TSP.2002.807005.

124. Chatnuntawech I, Gagoski B, Bilgic B, Cauley SF, Setsompop K, Adalsteinsson E. Accelerated 1 H MRSI using randomly undersampled spiral-based k-space trajectories. Magn. Reson. Med. 2015;74:13-24. doi: 10.1002/mrm.25394.

125. Maudsley AA, Domenig C, Govind V, Darkazanli A, Studholme C, Arheart K, Bloomer C. Mapping of brain metabolite distributions by volumetric proton MR spectroscopic imaging (MRSI). Magn. Reson. Med. 2009;61:548–559. doi: 10.1002/mrm.21875.

126. Gagoski BA, Ratai E, Eichler FS, Wiggins G, Roell S, Krueger G, Lee J, Adalsteinsson E. 3D volumetric in vivo spiral CSI at 7T. Proc. Intl. Soc. Mag. Reson. Med. 15 (2007) 635.

127. Wiesinger F, Weidl E, Menzel MI, Janich M a, Khegai O, Glaser SJ, Haase A, Schwaiger M, Schulte RF. IDEAL spiral CSI for dynamic metabolic MR imaging of hyperpolarized [1-13C]pyruvate. Magn. Reson. Med. 2012;68:8–16. doi: 10.1002/mrm.23212.

128. Mayer D, Yen Y-F, Takahashi A, Josan S, Tropp J, Rutt BK, Hurd RE, Spielman DM, Pfefferbaum A. Dynamic and high-resolution metabolic imaging of hyperpolarized [1-13C]-pyruvate in the rat brain using a high-performance gradient insert. Magn. Reson. Med. 2011;65:1228–33. doi: 10.1002/mrm.22707.

129. Levin YS, Mayer D, Yen Y-F, Hurd RE, Spielman DM. Optimization of fast

spiral chemical shift imaging using least squares reconstruction: application for hyperpolarized (13)C metabolic imaging. Magn. Reson. Med. 2007;58:245–52. doi: 10.1002/mrm.21327.

130. Mayer D, Levin YS, Hurd RE, Glover GH, Spielman DM. Fast metabolic imaging of systems with sparse spectra: Application for hyperpolarized 13C imaging. Magn. Reson. Med. 2006;56:932–7. doi: 10.1002/mrm.21025.

131. Mayer D, Yen Y, Levin YS, Tropp J, Pfefferbaum A, Ralph E, Spielman DM, Drive W. In Vivo Application of Sub-Second Spiral Chemical Shift Imaging (CSI) to Hyperpolarized 13 C Metabolic Imaging: Comparison with Phase-Encoded CSI. J Magn Reson. 2011;204:340–345. doi: 10.1016/j.jmr.2010.03.005.In.

132. Liu Y, Jiang Y, Wang C, Griswold M, Yu X. Fast 31P Chemical Shift Imaging Using Multi-Spiral Acquisition at 9.4T. Proc. Intl. Soc. Mag. Reson. Med. 23 2015.

133. Valkovič L, Chmelík M, Meyerspeer M, et al. Dynamic 31P–MRSI using spiral spectroscopic imaging can map mitochondrial capacity in muscles of the human calf during plantar flexion exercise at 7 T. NMR Biomed. 2016;29:1825–1834. doi: 10.1002/nbm.3662.

134. Schirda CV, Noll DC, Boada FE. Fast 2D Spectroscopic Imaging Using Rosette Trajectories. Proc. Intl. Soc. Mag. Reson. Med. 11 2003.

135. Valkovic L, Chmelik M, Meyerspeer M, Gagoski B, Rodgers CT, Krssak M, Andronesi OC, Trattnig S, Bogner W. Dynamic 31P-MRSI using spiral

spectroscopic imaging can map mitochondrial capacity in muscles of the human calf during plantar flexion exercise at 7 T. NMR Biomed. 2016;29:1825–1834. doi: 10.1002/nbm.3662.

136. Speck O, Scheffler K, Hennig J. Fast 31P chemical shift imaging using SSFP methods. Magn. Reson. Med. 2002;48:633–9. doi: 10.1002/mrm.10279.

137. Carr H, Resonance NM. Steady-State Free Precession in Nuclear Magnetic Resonance. Phys. Rev. 1958;112:1693–1701. doi: 10.1103/PhysRev.112.1693.

138. Leupold J, Wieben O, Månsson S, Speck O, Scheffler K, Petersson JS, Hennig J. Fast chemical shift mapping with multiecho balanced SSFP. MAGMA 2006;19:267–73. doi: 10.1007/s10334-006-0056-9.

139. Lam F, Liang ZP. A subspace approach to high-resolution spectroscopic imaging. Magn. Reson. Med. 2014;71:1349–1357. doi: 10.1002/mrm.25168.

140. Griswold MA, Jakob PM, Heidemann RM, Nittka M, Jellus V, Wang J, Kiefer B, Haase A. Generalized Autocalibrating Partially Parallel Acquisitions (GRAPPA). Magn. Reson. Med. 2002;47:1202–1210. doi: 10.1002/mrm.10171.

141. Pruessmann KP, Weiger M, Scheidegger MB, Boesiger P. SENSE: Sensitivity encoding for fast MRI. Magn. Reson. Med. 1999;42:952–962. doi: 10.1002/(SICI)1522-2594(199911)42:5<952::AID-MRM16>3.0.CO;2-S.

142. Sodickson DK, Manning WJ. Simultaneous acquisition of spatial harmonics (SMASH): Fast imaging with radiofrequency coil arrays. Magn. Reson. Med. 1997;38:591–603. doi: 10.1002/mrm.1910380414.

143. Lustig M, Donoho D, Pauly JM. Sparse MRI: The application of compressed

sensing for rapid MR imaging. Magn. Reson. Med. 2007;58:1182–95. doi: 10.1002/mrm.21391.

144. Maguire ML, Geethanath S, Lygate C a., Kodibagkar VD, Schneider JJE. Compressed sensing to accelerate magnetic resonance spectroscopic imaging: evaluation and application to 23Na-imaging of mouse hearts. J. Cardiovasc. Magn. Reson. 2015;17:45. doi: 10.1186/s12968-015-0149-6.

145. Arai T, Nakao S, Morikawa S, Inubushi T, Yokoi T, Shimizu K, Mori K. Measurement of local cerebral blood flow by magnetic resonance imaging: in vivo autoradiographic strategy using 17O-labeled water. Brain Res. Bull. 1998;45:451–6.

146. Arai T, Mori K, Nakao S, Watanabe K, Kito K, Aoki M, Mori H, Morikawa S, Inubushi T. In vivo oxygen-17 nuclear magnetic resonance for the estimation of cerebral blood flow and oxygen consumption. Biochem. Biophys. Res. Commun. 1991;179:954–61.

147. Pekar J, Ligeti L, Ruttner Z, Lyon RC, Sinnwell TM, van Gelderen P, Fiat D, Moonen CT, McLaughlin AC. In vivo measurement of cerebral oxygen consumption and blood flow using 17O magnetic resonance imaging. Magn. Reson. Med. 1991;21:313–9.

148. Alder F, Yu FC. On the spin and magnetic moment of O17. Phys. Rev. 1951;81:1067–1068. doi: 10.1103/PhysRev.81.1067.

149. Zhu XH, Merkle H, Kwag JH, Ugurbil K, Chen W. 17O relaxation time and NMR sensitivity of cerebral water and their field dependence. Magn. Reson. Med.

2001;45:543–549. doi: 10.1002/mrm.1073.

150. Zhu XH, Chen W. In vivo oxygen-17 NMR for imaging brain oxygen metabolism at high field. Prog. Nucl. Magn. Reson. Spectrosc. 2011;59:319–335. doi: 10.1016/j.pnmrs.2011.04.002.

151. Lu M, Zhang Y, Ugurbil K, Chen W, Zhu X-H. In vitro and in vivo studies of 17 O NMR sensitivity at 9.4 and 16.4 T. Magn. Reson. Med. 2013;69:1523–1527. doi: 10.1002/mrm.24386.

152. Mintun MA, Raichle ME, Martin WRW, Herscovitch P. Brain oxygen utilization measured with 0-15 radiotracers and positron emission tomography. J. Nucl. Med. 1984;25:177–187.

153. Pozzilli C, Itoh M, Matsuzawa T, Fukuda H, Abe Y, Sato T, Takeda S, Ido T. Positron emission tomography in minor ischemic stroke using oxygen-15 steady-state technique. J Cereb Blood Flow Metab 1987;7:137–142. doi: 10.1038/jcbfm.1987.36.

154. Zhu X-H, Zhang Y, Tian R-X, Lei H, Zhang N, Zhang X, Merkle H, Ugurbil K, Chen W. Development of (17)O NMR approach for fast imaging of cerebral metabolic rate of oxygen in rat brain at high field. Proc. Natl. Acad. Sci. U. S. A. 2002;99:13194–9. doi: 10.1073/pnas.202471399.

155. Zhang N, Zhu X-H, Lei H, Ugurbil K, Chen W. Simplified methods for calculating cerebral metabolic rate of oxygen based on 17O magnetic resonance spectroscopic imaging measurement during a short 17O2 inhalation. J. Cereb. Blood Flow Metab. 2004;24:840–8. doi: 10.1097/01.WCB.0000125885.54676.82.

156. Zhu X-H, Chen JM, Tu T-W, Chen W, Song S-K. Simultaneous and noninvasive imaging of cerebral oxygen metabolic rate, blood flow and oxygen extraction fraction in stroke mice. Neuroimage 2013;64:437–447. doi: 10.1016/j.neuroimage.2012.09.028.

157. Atkinson IC, Thulborn KR. Feasibility of mapping the tissue mass corrected bioscale of cerebral metabolic rate of oxygen consumption using 17-oxygen and 23-sodium MR imaging in a human brain at 9.4T. Neuroimage 2010;51:723–733. doi: 10.1016/j.neuroimage.2010.02.056.

158. Brown TR, Kincaid BM, Ugurbil K. NMR chemical shift imaging in three dimensions. Proc. Natl. Acad. Sci. U. S. A. 1982;79:3523–6. doi: 10.1073/pnas.79.11.3523.

159. Nagel AM, Laun FB, Weber MA, Matthies C, Semmler W, Schad LR. Sodium MRI using a density-adapted 3D radial acquisition technique. Magn. Reson. Med. 2009;62:1565–1573. doi: 10.1002/mrm.22157.

160. Lu A, Atkinson IC, Claiborne TC, Damen FC, Thulborn KR. Quantitative sodium imaging with a flexible twisted projection pulse sequence. Magn. Reson. Med. 2010;63:1583–1593. doi: 10.1002/mrm.22381.

161. Zhu X-H, Zhang Y, Zhang N, Ugurbil K, Chen W. Noninvasive and three-dimensional imaging of CMRO2 in rats at 9.4 T: reproducibility test and normothermia/hypothermia comparison study. J. Cereb. Blood Flow Metab. 2006;27:1225–1234. doi: 10.1038/sj.jcbfm.9600421.

162. Zhu X-H, Zhang N, Zhang Y, Uğurbil K, Chen W. New insights into central

roles of cerebral oxygen metabolism in the resting and stimulus-evoked brain. J. Cereb. blood flow Metab. 2009;29:10–8. doi: 10.1038/jcbfm.2008.97.

163. Cui W, Zhu X-H, Vollmers ML, Colonna ET, Adriany G, Tramm B, Dubinsky JM, Öz G, Oez G. Non-invasive measurement of cerebral oxygen metabolism in the mouse brain by ultra-high field (17)O MR spectroscopy. J. Cereb. Blood Flow Metab. 2013;33:1846–9. doi: 10.1038/jcbfm.2013.172.

164. Zhu XH, Zhang Y, Wiesner HM, Ugurbil K, Chen W. In vivo measurement of CBF using 17O NMR signal of metabolically produced H217O as a perfusion tracer. Magn. Reson. Med. 2013;70:309–314. doi: 10.1002/mrm.24469.

165. Hoffmann SH, Radbruch A, Bock M, Semmler W, Nagel AM. Direct 17O MRI with partial volume correction: first experiences in a glioblastoma patient. Magn. Reson. Mater. Physics, Biol. Med. 2014;c:579–587. doi: 10.1007/s10334-014-0441-8.

166. Kurzhunov D, Borowiak R, Hass H, Wagner P, Krafft AJ, Timmer J, Bock M. Quantification of oxygen metabolic rates in Human brain with dynamic ^{17} O MRI: Profile likelihood analysis. Magn. Reson. Med. 2016;0:1–11. doi: 10.1002/mrm.26476.

167. Andrade CS, Otaduy MCG, Park EJ, Leite CC. Phosphorus-31 MR spectroscopy of the human brain: technical aspects and biomedical applications. Int. J. Curr. Res. Rev. 2014;6:41–57.

168. Jeon MJ, Lee Y, Ahn S, Lee C, Kim O-H, Oh B-C, Yu U, Kim H. High resolution in vivo 31P-MRS of the liver: potential advantages in the assessment of

non-alcoholic fatty liver disease. Acta radiol. 2015;56:1051–1060. doi: 10.1177/0284185114550850.

169. Hoda SA, Hoda RS. Robbins and Cotran Pathologic Basis of Disease. Adv. Anat. Pathol. 2005;12:103. doi: 10.1097/01.pap.0000155072.86944.7d.

170. DeFronzo RA, Tripathy D. Skeletal muscle insulin resistance is the primary defect in type 2 diabetes. Diabetes Care 2009;32 Suppl 2:S157-63. doi: 10.2337/dc09-S302.

171. Petersen KF, Dufour S, Befroy D, Garcia R, Shulman GI, Möhlig M, Isken F, Ristow M. Impaired mitochondrial activity and insulin-resistant offspring of patients with type 2 diabetes. N. Engl. J. Med. 2004;350:2419-21-21. doi: 10.1056/NEJMoa031314.

172. Lowell BB, Shulman GI. Mitochondrial dysfunction and type 2 diabetes. Science 2005;307:384–387. doi: 10.1126/science.1104343.

173. Ritov VB, Menshikova E V, He J, Ferrell RE, Goodpaster BH, Kelley DE. Deficiency of subsarcolemmal mitochondria in obesity and type 2 diabetes. Diabetes 2005;54:8–14.

174. Kelley DE, He J, Menshikova E V, Ritov VB. Dysfunction of mitochondria in human skeletal muscle in type 2 diabetes. Diabetes 2002;51:2944–50.

175. Boushel R, Gnaiger E, Schjerling P, Skovbro M, Kraunsøe R, Dela F. Patients with type 2 diabetes have normal mitochondrial function in skeletal muscle. Diabetologia 2007;50:790–796. doi: 10.1007/s00125-007-0594-3.

176. De Feyter HM, van den Broek NM a, Praet SFE, Nicolay K, van Loon LJC,

Prompers JJ. Early or advanced stage type 2 diabetes is not accompanied by in vivo skeletal muscle mitochondrial dysfunction. Eur. J. Endocrinol. 2008;158:643–53. doi: 10.1530/EJE-07-0756.

177. Ogawa S, Lee TM, Kay a R, Tank DW. Brain magnetic resonance imaging with contrast dependent on blood oxygenation. Proc. Natl. Acad. Sci. U. S. A. 1990;87:9868–72.

178. Ledermann H-P, Schulte A-C, Heidecker H-G, Aschwanden M, Jäger K a, Scheffler K, Steinbrich W, Bilecen D. Blood oxygenation level-dependent magnetic resonance imaging of the skeletal muscle in patients with peripheral arterial occlusive disease. Circulation 2006;113:2929–35. doi: 10.1161/CIRCULATIONAHA.105.605717.

179. King AJF. The use of animal models in diabetes research. Br. J. Pharmacol. 2012;166:877–894. doi: 10.1111/j.1476-5381.2012.01911.x.

180. Goto Y, Kakizaki M, Masaki N. Production of spontaneous diabetic rats by repetition of selective breeding. Tohoku J. Exp. Med. 1976;119:85–90. doi: 10.1620/tjem.119.85.

181. Padilla DJ, McDonough P, Behnke BJ, Kano Y, Hageman KS, Musch TI, Poole DC. Effects of Type II diabetes on muscle microvascular oxygen pressures. Respir. Physiol. Neurobiol. 2007;156:187–95. doi: 10.1016/j.resp.2006.08.008.

182. Akash MS, Rehman K, Chen S. Goto-Kakizaki rats: its suitability as non-obese diabetic animal model for spontaneous type 2 diabetes mellitus. Curr Diabetes Rev 2013;9:387–396. doi: 10.2174/15733998113099990069.

183. Layec G, Malucelli E, Le Fur Y, Manners D, Yashiro K, Testa C, Cozzone PJ, Iotti S, Bendahan D. Effects of exercise-induced intracellular acidosis on the phosphocreatine recovery kinetics: a (31) P MRS study in three muscle groups in humans. NMR Biomed. 2013;26:1403–11. doi: 10.1002/nbm.2966.

184. Graaf L De, Nicolay K, Prompers JJ. Intersubject differences in the effect of acidosis on phosphocreatine recovery kinetics in Muscle After Exercise Are Due To Differences in Proton Efflux Rates. Am J Physiol Cell Physiol 2007;293:228–237. doi: 10.1152/ajpcell.00023.2007.

185. Roussel M, Bendahan D, Mattei JP, Le Fur Y, Cozzone PJ. 31P Magnetic resonance spectroscopy study of phosphocreatine recovery kinetics in skeletal muscle: The issue of intersubject variability. Biochim. Biophys. Acta - Bioenerg. 2000;1457:18–26. doi: 10.1016/S0005-2728(99)00111-5.

186. Arnold DL, Matthews PM, Radda GK. Metabolic recovery after exercise and the assessment of mitochondrial function in vivo in human skeletal muscle by means of 31P NMR. Magn Reson Med 1984;1:307–315.

187. Iotti S, Frassineti C, Sabatini A, Vacca A, Barbiroli B. Quantitative mathematical expressions for accurate in vivo assessment of cytosolic [ADP] and DeltaG of ATP hydrolysis in the human brain and skeletal muscle. Biochim. Biophys. Acta - Bioenerg. 2005;1708:164–177. doi: 10.1016/j.bbabio.2005.01.008.

188. Walter G, Vandenborne K, Elliott M, Leigh JS. In vivo ATP synthesis rates in single human muscles during high intensity exercise. J. Physiol. 1999;519 Pt

3:901–910. doi: 10.1111/j.1469-7793.1999.0901n.x.

189. Morino K, Petersen KF, Dufour S, et al. Reduced mitochondrial density and increased IRS-1 serine phosphorylation in muscle of insulin-resistant offspring of type 2 diabetic parents. J. Clin. Invest. 2005;115:3587–3593. doi: 10.1172/JCI25151.

190. Morino K, Petersen KF, Shulman GI. Molecular mechanisms of insulin resistance in humans and their potential links with mitochondrial dysfunction. Diabetes 2006;55. doi: 10.2337/db06-S002.

191. De Feyter HM, Lenaers E, Houten SM, Schrauwen P, Hesselink MK, Wanders RJ a, Nicolay K, Prompers JJ. Increased intramyocellular lipid content but normal skeletal muscle mitochondrial oxidative capacity throughout the pathogenesis of type 2 diabetes. FASEB J. 2008;22:3947–55. doi: 10.1096/fj.08-112318.

192. Morikawa S, Inubushi T, Kito K. Heterogeneous metabolic changes in the calf muscle of the rat during ischaemia-reperfusion: in vivo analysis by 31P nuclear magnetic resonance chemical shift imaging and 1H magnetic resonance imaging. Cardiovasc. Surg. 1993;1:337–42.

193. Padilla DJ, Mcdonough P, Behnke BJ, Kano Y, Hageman KS, Musch TI, Poole DC, Danielle J. Effects of Type II diabetes on capillary hemodynamics in skeletal muscle. Am J Physiol Hear. Circ Physiol 2006;5802:2439–2444. doi: 10.1152/ajpheart.00290.2006.

194. Felber JP, Ferrannini E, Golay A, Meyer HU, Theibaud D, Curchod B,

Maeder E, Jequier E, DeFronzo RA. Role of lipid oxidation in pathogenesis of insulin resistance of obesity and type II diabetes. Diabetes 1987;36:1341–1350. doi: 10.2337/diabetes.36.11.1341.

195. Staron RS, Kraemer WJ, Hikida RS, Fry AC, Murray JD, Campos GER. Fiber type composition of four hindlimb muscles of adult Fisher 344 rats. Histochem. Cell Biol. 1999;111:117–123. doi: 10.1007/s004180050341.

196. Ariano MA, Armstrong RB, Edgerton VR. Hindlimb muscle fiber populations of five mammals. J. Histochem. Cytochem. 1973;21:51–55. doi: 10.1177/21.1.51.

197. Armstrong RB, Phelps RO. Muscle fiber type composition of the rat hindlimb. Am. J. Anat. 1984;171:259–272. doi: 10.1002/aja.1001710303.

198. James DE, Jenkins a B, Kraegen EW. Heterogeneity of insulin action in individual muscles in vivo: euglycemic clamp studies in rats. Am. J. Physiol. 1985;248:E567–E574.

199. Albers PH, Pedersen AJT, Birk JB, Kristensen DE, Vind BF, Baba O, Nøhr J, Højlund K, Wojtaszewski JFP. Human Muscle Fiber Type–Specific Insulin Signaling: Impact of Obesity and Type 2 Diabetes. Diabetes 2015;64:485–497. doi: 10.2337/db14-0590.

200. Lillioja S, Young AA, Culter CL, Ivy JL, Abbott WG, Zawadzki JK, Yki-Järvinen H, Christin L, Secomb TW, Bogardus C. Skeletal muscle capillary density and fiber type are possible determinants of in vivo insulin resistance in man. J. Clin. Invest. 1987;80:415–24. doi: 10.1172/JCI113088.

201. Chance B, Eleff S, Leigh JS. Noninvasive, nondestructive approaches to cell bioenergetics. Proc. Natl. Acad. Sci. U. S. A. 1980;77:7430–7434. doi: 10.1073/pnas.77.12.7430.

202. Liang Z-P. Spatiotemporal Imaging with Partially Separable Functions. IEEE Int. Symp. Biomed. Imaging 2007;2:988–991. doi: 10.1109/ISBI.2007.357020.

203. Nguyen HM, Peng X, Do MN, Liang ZP. Denoising MR spectroscopic imaging data with low-rank approximations. IEEE Trans. Biomed. Eng. 2013;60:78–89. doi: 10.1109/TBME.2012.2223466.

204. Haldar JP, Liang ZP. Spatiotemporal imaging with partially separable functions: A matrix recovery approach. In: 2010 7th IEEE International Symposium on Biomedical Imaging: From Nano to Macro, ISBI 2010 - Proceedings. 2010:716–719. doi: 10.1109/ISBI.2010.5490076.

205. Kasten J, Lazeyras F, Van De Ville D. Data-driven MRSI spectral localization via low-rank component analysis. IEEE Trans. Med. Imaging 2013;32:1853–1863. doi: 10.1109/TMI.2013.2266259.

206. Lam F, Ma C, Clifford B, Johnson CL, Liang ZP. High-resolution 1H-MRSI of the brain using SPICE: Data acquisition and image reconstruction. Magn. Reson. Med. 2016;76:1059–1070. doi: 10.1002/mrm.26019.

207. Ma C, Lam F, Ning Q, Johnson CL, Liang ZP. High-resolution 1H-MRSI of the brain using short-TE SPICE. Magn. Reson. Med. 2017;77:467–479. doi: 10.1002/mrm.26130.

208. Lam F, Lu H, Yang Y, Robinson GE, Liang Z. Ultrahigh-Resolution

Metabolic Imaging at 9.4 Tesla. Proc. Intl. Soc. Mag. Reson. Med. 24 (2016) 385.

209. Ma C, Lam F, Ning Q, Clifford B, Liu Q, Johnson CL, Liang Z. High-Resolution Dynamic 31P-MRSI Using High-Order Partially Separable Functions. Proc. Intl. Soc. Mag. Reson. Med. 24 2016:4–6.

210. Lam F, Ning Q, Larsen R, Liang Z. A Subspace-Based Approach to High-Resolution 31P-MRSI. Proc. Intl. Soc. Mag. Reson. Med. 24 2016:6–8.

211. Tucker LR. Some mathematical notes on three-mode factor analysis. Psychometrika 1966;31:279–311. doi: 10.1007/BF02289464.

212. Mateescu GD. Functional oxygen-17 magnetic resonance imaging and localized spectroscopy. Adv. Exp. Med. Biol. 2003;510:213–8.

213. Zhu X-H, Zhang N, Zhang Y, Zhang X, Ugurbil K, Chen W. In vivo 17O NMR approaches for brain study at high field. NMR Biomed. 2005;18:83–103. doi: 10.1002/nbm.930.

214. Gordji-Nejad A, Möllenhoff K, Oros-Peusquens AM, Pillai DR, Shah NJ. Characterizing cerebral oxygen metabolism employing oxygen-17 MRI/MRS at high fields. Magn. Reson. Mater. Physics, Biol. Med. 2014;27:81–93. doi: 10.1007/s10334-013-0413-4.

215. Wiesner HM, Balla DZ, Shajan G, Scheffler K, Uğurbil K, Chen W, Uludağ K, Pohmann R. 17O relaxation times in the rat brain at 16.4 tesla. Magn. Reson. Med. 2016;75:1886–1893. doi: 10.1002/mrm.25814.

216. de Crespigny AJ, D'Arceuil HE, Engelhorn T, Moseley ME. MRI of focal cerebral ischemia using (17)O-labeled water. Magn. Reson. Med. 2000;43:876–

83. doi: 10.1002/1522-2594(200006)43:6<876::AID-MRM14>3.0.CO;2-Y [pii].

217. Hopkins AL, Barr RG. Oxygen-17 compounds as potential NMR T2 contrast agents: Enrichment effects of H217O on protein solutions and living tissues. Magn. Reson. Med. 1987;4:399–403. doi: 10.1002/mrm.1910040413.

218. Herscovitch P, Markham J, Raichle ME. Brain blood flow measured with intravenous H2(15)O. I. Theory and error analysis. J. Nucl. Med. 1983;24:782–9.

219. Raichle ME, Martin WR, Herscovitch P, Mintun MA, Markham J. Brain blood flow measured with intravenous H2(15)O. II. Implementation and validation. J. Nucl. Med. 1983;24:790–8.

220. Mintun MA, Raichle ME, Martin WR, Herscovitch P. Brain oxygen utilization measured with O-15 radiotracers and positron emission tomography. J. Nucl. Med. 1984;25:177–87.

221. Fox PT, Raichle ME, Mintun MA, Dence C. Nonoxidative glucose consumption during focal physiologic neural activity. Science 1988;241:462–4.

222. Winkelmann S, Schaeffter T, Koehler T, Eggers H, Doessel O. An optimal radial profile order based on the golden ratio for time-resolved MRI. IEEE Trans. Med. Imaging 2007;26:68–76. doi: 10.1109/TMI.2006.885337.

223. Song HK, Dougherty L. k-Space weighted image contrast (KWIC) for contrast manipulation in projection reconstruction MRI. Magn. Reson. Med. 2000;44:825–832. doi: 10.1002/1522-2594(200012)44:6<825::AID-MRM2>3.0.CO;2-D.

224. Feng L, Grimm R, Block KT obias, Chandarana H, Kim S, Xu J, Axel L,

Sodickson DK, Otazo R. Golden-angle radial sparse parallel MRI: combination of compressed sensing, parallel imaging, and golden-angle radial sampling for fast and flexible dynamic volumetric MRI. Magn. Reson. Med. 2014;72:707–717. doi: 10.1002/mrm.24980.

225. Song HK, Yan L, Smith RX, Xue Y, Rapacchi S, Srinivasan S, Ennis DB, Hu P, Pouratian N, Wang DJJ. Noncontrast enhanced four-dimensional dynamic MRA with golden angle radial acquisition and K-space weighted image contrast (KWIC) reconstruction. Magn. Reson. Med. 2014;72:1541–1551. doi: 10.1002/mrm.25057.

226. Pipe JG, Menon P. Sampling density compensation in MRI: Rationale and an iterative numerical solution. Magn. Reson. Med. 1999;41:179–186. doi: 10.1002/(SICI)1522-2594(199901)41:1<179::AID-MRM25>3.0.CO;2-V.

227. Lin W, Guo J, Rosen MA, Hee KS. Respiratory motion-compensated radial dynamic contrast-enhanced (DCE)-MRI of chest and abdominal lesions. Magn. Reson. Med. 2008;60:1135–1146. doi: 10.1002/mrm.21740.

228. Hladky SB, Barrand MA. Mechanisms of fluid movement into, through and out of the brain: evaluation of the evidence. Fluids Barriers CNS 2014;11:26. doi: 10.1186/2045-8118-11-26.

229. Williams DS, Detre JA, Leigh JS, Koretsky AP. Magnetic resonance imaging of perfusion using spin inversion of arterial water. Proc. Natl. Acad. Sci. U. S. A. 1992;89:212–6. doi: 10.1073/pnas.89.9.4220e.

230. Zhang K, Herzog H, Mauler J, et al. Comparison of cerebral blood flow

acquired by simultaneous [(15)O]water positron emission tomography and arterial spin labeling magnetic resonance imaging. J. Cereb. Blood Flow Metab. 2014:1–8. doi: 10.1038/jcbfm.2014.92.

231. Igarashi H, Suzuki Y, Kwee IL, Nakada T. Water influx into cerebrospinal fluid is significantly reduced in senile plaque bearing transgenic mice, supporting beta-amyloid clearance hypothesis of Alzheimer's disease. Neurol. Res. 2014;36:1094–1098. doi: 10.1179/1743132814Y.0000000434.

232. Yu J, Xue Y, Song HK. Comparison of lung T2* during free-breathing at 1.5 T and 3.0 T with ultrashort echo time imaging. Magn. Reson. Med. 2011;66:248–254. doi: 10.1002/mrm.22829.

233. Kalpathy-Cramer J, Gerstner ER, Emblem KE, Andronesi OC, Rosen B. Advanced magnetic resonance imaging of the physical processes in human Glioblastoma. Cancer Res. 2014;74:4622–4637. doi: 10.1158/0008-5472.CAN-14-0383.

234. Hossman KA, Bloink M. Blood Flow and Regulation of Blood Flow in Experimental Peritumoral Edema. Stroke 1981;12:211–217.

235. Steen RG. Edema and Tumor Perfusion : Characterization by Quantitative 1H MR Imaging. AJR 1992;158:259–264.

236. Heiss WD. The ischemic penumbra: Correlates in imaging and implications for treatment of ischemic Stroke: The Johann Jacob Wepfer Award 2011. Cerebrovasc. Dis. 2011;32:307–320. doi: 10.1159/000330462.

237. Barber PA, Darby DG, Desmond PM, Yang Q, Gerraty RP, Jolley D,

Donnan GA, Tress BM, Davis SM. Prediction of stroke outcome with echoplanar perfusion- and diffusion-weighted MRI. Neurology 1998;51:418–426. doi: 10.1212/WNL.51.2.418.

238. Mishra NK, Albers G, Davis GA et al. A systematic overview of thrombolysis 3-9H from stroke onset in patients selected according to mismatch criteria. Cerebrovasc Dis 2009; 27(Sup- pl. 6): 31

239. Kane I, Sandercock P, Wardlaw J. Magnetic resonance perfusion diffusion mismatch and thrombolysis in acute ischaemic stroke: a systematic review of the evidence to date. J Neurol Neurosurg Psychiatry 2007;78:485–491. doi: 10.1136/jnnp.2006.100347.

240. Rivers CS, Wardlaw JM, Armitage PA, Bastin ME, Carpenter TK, Cvoro V, Hand PJ, Dennis MS. Do acute diffusion- and perfusion-weighted MRI lesions identify final infarct volume in ischemic stroke? Stroke 2006;37:98–104. doi: 10.1161/01.STR.0000195197.66606.bb.

241. Wardlaw JM. Neuroimaging in acute ischaemic stroke: Insights into unanswered questions of pathophysiology. J. Intern. Med. 2010;267:172–190. doi: 10.1111/j.1365-2796.2009.02200.x.

242. Glover GH, Hayes CE, Pelc NJ, Edelstein WA, Mueller M, Hart HR, Hardy CJ, O ’donnell M, Barber-~ WD. Comparison of Linear and Circular Polarization for Magnetic Resonance Imaging. J. Magn. Reson. 1985;64:255–270. doi: 10.1016/0022-2364(85)90349-X.

243. Mirkes CC, Hoffmann J, Shajan G, Pohmann R, Scheffler K. High-

resolution quantitative sodium imaging at 9.4 tesla. Magn. Reson. Med. 2014;25096:25393. doi: 10.1002/mrm.25096.

244. Sui Y, Xing H, Claiborne T, Thulborn KR, and Zhou XJ. Relaxation Time Measurements of 31 P Metabolites in Human Muscle at 9.4 Tesla. Proc. Intl. Soc. Mag. Reson. Med. 19 (2011) 3507.

245. Chan RW, Ramsay EA, Cunningham CH, Plewes DB. Temporal stability of adaptive 3D radial MRI using multidimensional golden means. Magn. Reson. Med. 2009;61:354–363. doi: 10.1002/mrm.21837.

246. Riederer SJ, Tasciyan T, Farzaneh F, Lee JN, Wright RC, Herfkens RJ. MR fluoroscopy: Technical feasibility. Magn. Reson. Med. 1988;8:1–15. doi: 10.1002/mrm.1910080102.

247. Van Vaals JJ, Brummer ME, Thomas Dixon W, Tuithof HH, Engels H, Nelson RC, Gerety BM, Chezmar JL, Den Boer JA. “Keyhole” method for accelerating imaging of contrast agent uptake. J. Magn. Reson. Imaging 1993;3:671–675. doi: 10.1002/jmri.1880030419.

248. Jones RA, Haraldseth O, Müller TB, Rinck PA, Oksendal AN. K-space substitution: a novel dynamic imaging technique. Magn Reson Med 1993;29:830–834. doi: 10.1002/mrm.1910290618.

249. Doyle M, Walsh EG, Blackwell GG, Pohost GM. Block Regional Interpolation Scheme for k-Space (BRISK): A Rapid Cardiac Imaging Technique. Magn. Reson. Med. 1995;33:163–170. doi: 10.1002/mrm.1910330204.

250. Parrish T, Hu X. Continuous Update with Random Encoding (CURE): A

New Strategy for Dynamic Imaging. Magn. Reson. Med. 1995;33:326–336. doi: 10.1002/mrm.1910330307.

251. Korosec FR, Frayne R, Grist TM, Mistretta CA. Time-resolved contrast-enhanced 3D MR angiography. Magn. Reson. Med. 1996;36:345–351. doi: 10.1002/mrm.1910360304.

252. Lim RP, Shapiro M, Wang EY, et al. 3D Time-Resolved MR Angiography (MRA) of the Carotid Arteries with Time-Resolved Imaging with Stochastic Trajectories: Comparison with 3D Contrast-Enhanced Bolus-Chase MRA and 3D Time-Of-Flight MRA. Am. J. Neuroradiol. 2008;29:1847–1854. doi: 10.3174/ajnr.A1252.

253. Madore B, Glover GH, Pelc NJ. Unaliasing by Fourier-encoding the overlaps using the temporal dimension (UNFOLD), applied to cardiac imaging and fMRI. Magn. Reson. Med. 1999;42:813–828. doi: 10.1002/(SICI)1522-2594(199911)42:5<813::AID-MRM1>3.0.CO;2-S.

254. Tsao J, Boesiger P, Pruessmann KP. k-t BLAST and k-t SENSE: dynamic MRI with high frame rate exploiting spatiotemporal correlations. Magn. Reson. Med. 2003;50:1031–42. doi: 10.1002/mrm.10611.

255. Tsao J, Kozerke S. MRI temporal acceleration techniques. J. Magn. Reson. Imaging 2012;36:543–60. doi: 10.1002/jmri.23640.

256. Luptak I, Balschi JA, Xing Y, Leone TC, Kelly DP, Tian R. Decreased contractile and metabolic reserve in peroxisome proliferator-activated receptor-alpha-null hearts can be rescued by increasing glucose transport and utilization.

Circulation 2005;112:2339–2346. doi:
10.1161/CIRCULATIONAHA.105.534594.

257. Spindler M, Saupe KW, Christe ME, Sweeney HL, Seidman CE, Seidman JG, Ingwall JS. Diastolic dysfunction and altered energetics in the alphaMHC403/+ mouse model of familial hypertrophic cardiomyopathy. J. Clin. Invest. 1998;101:1775–83. doi: 10.1172/JCI1940.

258. Bowers JL, Lanir A, Metz KR, Kruskal JB, Lee RG, Balschi J, Federman M, Khettry U, Clouse ME. 23Na- and 31P-NMR studies of perfused mouse liver during nitrogen hypoxia. Am. J. Physiol. 1992;262:G636-44.

259. Braun KPJ, van Eijsden P, Vandertop WP, de Graaf RA, Gooskens RHJM, Tulleken KAF, Nicolay K. Cerebral metabolism in experimental hydrocephalus: an in vivo ^{1} H and ^{31} P magnetic resonance spectroscopy study. J. Neurosurg. 1999;91:660–668. doi: 10.3171/jns.1999.91.4.0660.

260. Chung Y, Mole PA, Sailasuta N, Tran TK, Hurd R, Jue T. Control of respiration and bioenergetics during muscle contraction. 2005;8635:730–738. doi: 10.1152/ajpcell.00138.2004.

261. Kemp GJ, Thompson CH, Barnes PR, Radda GK. Comparisons of ATP turnover in human muscle during ischemic and aerobic exercise using 31P magnetic resonance spectroscopy. Magn. Reson. Med. 1994;31:248–258. doi: 10.1002/mrm.1910310303.

262. Kingsley-Hickman PB, Sako EY, Mohanakrishnan P, Robitaille PM, From AH, Foker JE, Uğurbil K. 31P NMR studies of ATP synthesis and hydrolysis

kinetics in the intact myocardium. Biochemistry 1987;26:7501–10.

263. Robitaille PM, Merkle H, Sako E, Lang G, Clack RM, Bianco R, From AH, Foker J, Uğurbil K. Measurement of ATP synthesis rates by 31P-NMR spectroscopy in the intact myocardium in vivo. Magn. Reson. Med. 1990;15:8–24.

264. Kingsley-Hickman PB, Fokers JE, Sakoz Y, Fromll HL, Sako EY, Uğurbil K, From a H, Foker JE. 31P NMR measurement of mitochondrial uncoupling in isolated rat hearts. J. Biol. Chem. 1990;265:1545–50.

265. Leibfritz D, Dreher W. Magnetization transfer MRS. NMR Biomed. 2001;14:65–76. doi: 10.1002/nbm.681.

266. Balaban RS, Kantor HL, Ferretti JA. In vivo flux between phosphocreatine and adenosine triphosphate determined by two-dimensional phosphorous NMR. J. Biol. Chem. 1983;258:12787–9.

267. Befroy DE, Rothman DL, Petersen KF, Shulman GI. ^{31}P-magnetization transfer magnetic resonance spectroscopy measurements of in vivo metabolism. Diabetes 2012;61:2669–78. doi: 10.2337/db12-0558.

268. Thoma WJ, Uğurbil K. Saturation-transfer studies of ATP-Pi exchange in isolated perfused rat liver. BBA - Bioenerg. 1987;893:225–231. doi: 10.1016/0005-2728(87)90043-0.

269. Matthews PM, Bland JL, Gadian DG, Radda GK. The steady-state rate of ATP synthesis in the perfused rat heart measured by 31P NMR saturation transfer. Biochem. Biophys. Res. Commun. 1981;103:1052–1059. doi: 10.1016/0006-

291X(81)90915-3.

270. Kemp GJ. The interpretation of abnormal 31P magnetic resonance saturation transfer measurements of Pi/ATP exchange in insulin-resistant skeletal muscle. Am. J. Physiol. Endocrinol. Metab. 2008;294:E640-2-4. doi: 10.1152/ajpendo.00797.2007.

271. Du F, Zhu X-HH, Qiao H, Zhang X, Chen W. Efficient in vivo 31P magnetization transfer approach for noninvasively determining multiple kinetic parameters and metabolic fluxes of ATP metabolism in the human brain. Magn. Reson. Med. 2007;57:103–14. doi: 10.1002/mrm.21107.

272. Atkinson IC, Thulborn KR. Feasibility of mapping the tissue mass corrected bioscale of cerebral metabolic rate of oxygen consumption using 17-oxygen and 23-sodium MR imaging in a human brain at 9.4 T. Neuroimage 2010;51:723–33. doi: 10.1016/j.neuroimage.2010.02.056.